AN ABSTRACT OF THE DISSERTATION OF

Jonathan Day for the degree of Doctor of Philosophy in Physics

presented on June 20, 2008.

Title: On the Photoresponse of Several Novel Functionalized Oligoacene and Anthradithiophene Derivatives

Abstract approved:

Oksana Ostroverkhova

The results of an investigation into carrier dynamics in several novel functionalized and solution-processable pentacene and anthradithiophene derivatives are reported. Measurements were made of real-time photoresponse of polycrystalline thin films of these materials to ultrafast laser pulses, on picosecond to microsecond time-scales, as well as measurements of dark current and current under steady illumination. This data was taken over varied field-strength, light intensity and temperature. The results support a model for carrier generation and transport with the following features. Carrier photo-generation is assisted weakly, if it is assisted at all, thermally or by applied fields. Carriers are initially (picosecond to nanosecond time-scales) in extended states and transport is "bandlike." Carriers then relax into more localized states, transported via

thermally assisted hopping (nanosecond to second time-scales). This model was supported by further experiments with the electric behavior of films prepared from a pure anthradithophene derivative, doped with either the buckminsterfullerene C_{60} or with other molecular dopants. These results also show that samples with traps of known density and depth can be prepared, as a means of manipulating transport dynamics. The electronic and photo-electronic behaviors of films with self-anodized aluminum and of films with gold electrodes were compared, and a model of the particular energy profile and dynamics which exist at the different interfaces between the films and the different contacts was developed. This model views the metal-organic-metal system as an anode-to-anode Schottky strucure, whose I-V relation is shaped both by the nature of the interface dynamics for different metal contacts, and by the different distributions of space-charge in the thin film between different electrodes.

© Copyright Jonathan Day

June 20, 2008

All Rights Reserved

On the Photoresponse of Several Novel Functionalized Oligoacene and Anthradithiophene Derivatives

by

Jonathan Day

A DISSERTATION

submitted to

Oregon State University

in partial fulfillment of
the requirements for the
degree of
Doctor of Philosophy

Presented June 20, 2008
Commencement June 2009

Doctor of Philosophy dissertation of Jonathan Day

presented on June 20, 2008

APPROVED:

Major Professor, representing Physics

Chair of the Department of Physics

Dean of the Graduate School

I understand that my dissertation will become part of the permanent collection of Oregon State University libraries. My signature below authorizes release of my dissertation to any reader upon request.

Jonathan Day, Author

DEDICATION

This thesis is dedicated to my wife, fellow artist, and comrade, Fay Jones Day.

ACKNOWLEDGMENTS

I owe fervent thanks to my major professor, Dr. Oksana Ostroverkhova, for unfailing support and for setting unremittingly high standards. Thanks also go to Dr. Yun-Shik Lee, Dr. William Hetherington, Dr, Janet Tate, Jeremy Danielsen, Andrew Jameson, Rick Presley, Robert Kykyneshi and Joe Tomaino for sometimes critical technical support. My colleagues past and present in Dr. Ostroverkhova's research group, Whitney Buchanan, Mark Kendrick, Andy Platt, Joe Peterson, Sam Peterson, Vince Rossi, Zack Peterson, and Mark Mazurier have been first rate, offering ideas, making suggestions, and asking often pointed and fruitful questions. The faculty of the Physics Department of Oregon State have been excellent, setting a bar which sometimes seemed terrifyingly high, but which was really just high enough.

I owe deepest thanks to my mother, Emylou Lloyd, for all her support and encouragement over many, many years.

Finally, I can never repay my debt to my wife, Fay Jones Day. She knows what I'm talking about.

TABLE OF CONTENTS

Page

Chapter

1. Introduction 1

1.1 Organic and inorganic semiconductors 1

1.1.1 Materials: Conjugated Polymers 5

1.1.2 Materials: Polyacenes 6

1.2 Electric Current in Organic Materials 9

1.3 Interfaces 12

1.4 Methods 12

1.4.1 Materials preparation 12

1.4.2 Non-contact Methods: Optical Pump, THz Probe 13

1.4.3 Non-contact Methods: All-optical Pump-Probe 16

1.4.4 Contact Methods: DSO 16

1.4.5 Temperature and other environmental parameters 17

1.5 Overview of this Thesis 18

2. Background 19

2.1 Carrier Photogeneration 19

2.2 Carrier Transport 22

2.3 Problems with the Onsager model 25

2.3.1 1987: Polydiacetylene 25

TABLE OF CONTENTS (Continued)

Chapter Page

2.3.2 1993 – 1994: PPV 27
2.3.3 1995: Electron transfer polymer-to-fullerene 31
2.3.4 1996: Transient PC and PL in PPV at high fields 31
2.3.5 2000: IRAV 33
2.3.6 2006: Tetracene 35
2.4 Nearly-small molecular polarons 36
2.5 Modified Onsager model 38
2.5.1 1991: DC and Transient photoconductivity 38
2.5.2 1994: Quenching & Excitons 38
2.5.3 1997: PPV: Geminate Pair Dissociation 39
2.5.4 1999–2000: Dissociation of hot excitons 42
2.6 Results of other recent work 45
2.6.1 Graupner Group 45
2.6.2 Hegmann, Ostroverkhova Groups 47
2.7 Summary 49
3. Transient and CW Photoresponse: 285–350 K 53
3.1 Introduction 53
3.1.1 Traps 56
3.1.2 Materials Preparation 57

TABLE OF CONTENTS (Continued)

Chapter Page

3.1.3 Instrumentation 62

3.1.4 Evolution of the Sample Fixture 65

3.2 Results 68

3.2.1 Transient Photoresponse 68

3.2.2 CW photoconductivity 74

3.3 Discussion 78

3.3.1 Photogeneration efficiency 81

3.3.2 Transient decay 82

3.3.3 Electric field dependence 84

3.3.4 Distribution of trapping states 85

3.3.5 Intensity dependence 86

3.3.6 Localization processes on longer time-scales 87

3.4 Conclusions 87

4. Doping: Probing and Manipulating Transport Dynamics 89

4.1 Introduction 89

4.2 Materials 90

4.3 Experiment 92

4.4 Results 93

4.4.1 Transient photoresponses 93

TABLE OF CONTENTS (Continued)

Chapter Page

4.4.2 Dark current and photoresponse 94
4.5 Discussion 96
4.5.1 Doping with C60 96
4.5.2 Molecular Dopants 101
4.6 Conclusions 105
5. Contact Effects 107
5.1 Introduction 107
5.2 Materials 108
5.3 Experiments and Results 108
5.3.1 Transient and CW photoresponse measurements 110
5.3.2 Transient photoresponse 110
5.3.3 Geometry differences. Back illumination versus front 111
5.3.4 Dark current and cw photocurrent 112
5.3.5 Gap Scan: Photoresponse 115
5.3.6 Gap scan: transients 118
5.4 Discussion 119
5.4.1 Space charge in electrode gap 119
5.4.2 Aluminum Contacts 121
5.4.3 Gold contacts 131

TABLE OF CONTENTS (Continued)

Chapter Page

5.4.4 Peak transient photoresponse versus CW 133

5.4.5 Transient response to localized excitation 136

5.4.6 Back illumination versus front 137

5.5 Conclusions 137

6. Summary and Concusions 139

REFERENCES 141

APPENDIX A: CALCULATION OF THE $\mu\eta$ PRODUCT FROM TRANSIENT PHOTOCURRENT DATA 149

APPENDIX B: DISPLACEMENT CURRENTS AND FRANKEVICH'S ANALYSIS 152

VITA 159

LIST OF FIGURES

Figure		Page
1.1	A clear, flexible, image scanner developed by S. Takao and his group, at the University of Tokyo.	2
1.2	A commercially available OLED display unit, from Densitron Technologies	4
1.3	Example of conjugated polymer: polypyrrole. (From http://www.wam.umd.edu/ smela/conj_pols.htm)	5
1.4	Structures of some conjugated polymers. (From F. Hegmann[63]) . . .	6
1.5	Structures of some polyacene molecules. The wavelength of the lowest energy absorption peak is also indicated.[21] (From F. Hegmann[63]) .	7
1.6	Schematic view of the lowest bonding orbital π-electron cloud above and below the plane of the anthracene molecule. The lower image is electron density sections through the central molecular planes in the anthracene crystal. (From M. Pope, C. E. Swengerg[21])	8
1.7	Functionalized pentacene-pendant structure: Pc-TIPS. From J. S. Brooks *et al*[23]	9
1.8	Molecular structure of materials used in this study: Clockwise from top left: ADT-TIPS-F, Pc-TIPS and DCDHF. For ADT-TIPS-F, R = Si (i-PR)$_3$. For ADT-TES-F, R = Si (Et)$_3$.	10
1.9	ADT-TIPS-F π-stacking (top) contrasted with that of ADT-TES-F (bottom). (From S. Subramanian.[120])	10
1.10	(a) Typical optical-pump THz-probe apparatus. BS: beam splitter; P: polyethylene visible beam block; F: blue filter; S: sample; A: 1 mm aperture $\lambda/4$: quarter-wave plate; WP: Wollaston prism; and BD: balanced detector. (b) Single-scan THz trace (FWHM 250 fs) and (c) spectrum obtained under dry N_2. From K. P. H. Lui [30]	14

LIST OF FIGURES (Continued)

Figure		Page
1.11	Transmitted pulse probe intensity as a function of probe delay time. From F. Hegmann[63]	15
1.12	Transient photoinduced absorption as a function of probe delay time. From F. Hegmann[63]	15
1.13	A typical excite-and-probe experimental setup. The ultrashort laser pulse is separated into a pump and a probe beam with a variable optical delay between them (Δt). The pump beam is normally used to excite the semiconductor, whereas the probe beam, typically much weaker than the pump beam, is used to measure the changes induced by the first pulse as a function of the optical delay between them. From A. Athonos [31]	16
1.14	Schematic of fixture for measurement of transient photoresponse with an applied potential	17
2.1	Energy band diagrams of photoexcitations in organic semiconductors according to (a) the semiconductor band model and (b) the molecular exciton model. (From F. Hegmann.[5])	20
2.2	Example spectrum of pure pentacene films showing absorption edge at 750 nm.	22
2.3	Temperature dependence of the peak transient photocurrent from 360 to 81 K (open circles); the magnitudes of the fast (solid circles) and slower (solid triangles) components at 297 and 81 K are indicated. (From Lee *at al*, PRB **49** 2396 (1993)).	29
2.4	The time dependence of the PIA of MEH-PPV/[6,6]PCBCa (2%) at 1.45 eV (open circles) and at 1.2 eV (open triangles), and of MEH–PPV/[6,6]PCBCa (50%) at 1.45 ev (closed circles) and at 1.2 eV (closed triangles). (From Kraabel *et al* J. Chem. Phys. **104** 4267 (1996))	32

Figure Page

2.5 The dependence of the peak transient photocurrent (I_P) and dark current (I_D) on external field at various temperatures in tensile drawn, oriented PPV, $l/l_0 = 10$. The top curve (open circles) shows that I_P is temperature independent. The lower curves represent I_D: 300 K (solid circles), 250 K (solid squares), 200 K (solid diamonds), 150 K (solid triangles), 100 K (open squares). From Moses *et al* (1996[50] 33

2.6 Comparison of the PIA wave form in MEH-PPV (solid circles) and MEH-PPV/C_{60} (50 % C_{60} by weight) (solid triangles), when pumped at the same light intensity at 800 nm and probed at 7 μm. From D. Moses *et al*, [42] 35

2.7 Data points represent the quantum yield ϕ of the dc photocurrent as a function of electric field ($\lambda_{exc} = 400$ nm, $T = 295$K). Solid curves are Onsager dissociation yields calculated for an initial pair separation of 25Å, assuming 3D (upper) and 1D (lower) topology, respectively. (From Gailberger and Bässler, PRB **44** 8643, (1991)) 39

2.8 Transient luminescence quenching at 70 K as detected with luminescence upconversion (squares). The data are extracted from the time-resolved luminescence signals taken without bias and with an applied voltage of 17 V. The cross indicates the value obtained in CW measurements. (From Kersting *et al*, PRL **73** 1440 (1994)). . 40

2.9 Scheme of the relaxation and dissociation processes involved without bias (a) and with applied field (b). ρ_1 denotes the density of states of the excitons. ρ_2 is the density of states if one of the carriers is transferred to a neighboring site. The arrows indicate the relaxation paths. ΔE_0 (with field) and ΔE_1 (without field) indicate the energy differences between an exciton and a geminate e–h pair with a charge separation r_L. (From Kersting *et al*, PRL **73** 1440 (1994)). 41

2.10 Field dependence of the intrinsic photocurrent in a 95 nm thick PPV–ether film. The photocurrent was measured upon irradiating through the ITO/SiO electrode at positive bias. (From Barth *et al*, Chemical Physics Letters **274** 165 (1997).) 42

2.11 Onsager dissociation efficiency vs. square root of the applied electric field for several separations. (From Pai and Enck (PRB **11** (1975) 5163) 43

Figure Page

2.12 Comparison between the experimental field dependence of the intrinsic photocarrier yield in undiluted PPV-ether, and theoretical 3D Onsager fits for $\epsilon = 4$ and variable thermalization distance r_0. (From Barth *et al* PRB **56** (1997) 3844) 44

2.13 Schematic view of geminate pair dissociation in an energetically random hopping system. At high temperatures a carrier generated optically (process 1) at a certain thermalization distance r_0 can either dissociate via thermally activated jumps involving states close to the center of the manifold of hopping states (route 2) or recombine (route 3). At low temperatures escape proceeds via the tail states of the DOS (route 4). This route requires less thermal energy. (From Barth, Bässler, *et al*, CPL **274** (1997) 165-170) 45

2.14 Field–induced differential transmission $(-\Delta T/T)_{MF}$ at 1.91 (solid line) and 2.53 eV (dots) as a function of pump-probe delay. Upper panel (dashed line) pump pulse autocorrelation). From W. Graupner, *et al* [34] 46

2.15 (a) Percent differential transmission of the peak of the THz probe pulse as a function of delay time and temperature. (b) Log-log plot of data shown in (a). Lines labeled m = -1 and m = -0.5 are guides to the eye for power law decay rates of t^{-1} and $t^{-0.5}$, respectively. From F. Hegmann.[54] 48

2.16 Differential transmission of the peak of the THz probe pulse as a function of delay time and temperature. (a) FPc crystal under optical excitation at 400 nm with $F \sim 0.4$ cm^2 at temperatures of 298, 40, and 10 K. The inset shows a power-law fit $\Delta t^{-\beta}$ ($\beta = 0.55$) to the data obtained at 80 K for Δt ¿ 2 ps. (b) Pc thin film under optical excitation at 580 nm with $F \sim 1$ mJ/cm^2 at temperatures of 298, 120, 80, and 20 K. Single-exponential fits to the data are also shown. From O. Ostroverkhova.[29] 49

3.1 Molecular structures. R = Si(i-Pr)$_3$. 58

3.2 Optical absorption spectra of ADT–TIPS–F, Pc–TIPS and DCDHF films. 59

Figure Page

3.3 Typical interdigitated electrode pair: metal areas black, active area 1 mm, finger width 25μm, interfinger spacing 25μm. Film shown: ADT-TIPS-F 60

3.4 Instrumentation and fixture setup for measurements of transient photoresponse. 63

3.5 Instrumentation and fixture setup for measurements of continuous-wave (CW) photoresponse 63

3.6 Early version of fixture. Shunt capacitor/series inductor network serves as low pass filter, to ensure that potential across sample/load resistor network remains constant. 64

3.7 Schematic of fixture used in transient photocurrent experiments . . . 64

3.8 Transient photo-response of Pc-TIPS film with varied beam intensity, measured with early version of sample fixture, exhibiting severe "ringing." 65

3.9 Later version of fixture. Electrode pair is shown end view. 67

3.10 Transient photocurrent obtained in ADT–TIPS–F, Pc–TIPS and DCDHF films at 1.2×10^4 V/cm and 30 μJ/cm^2 at 400 nm. Inset: Normalized transient photocurrents (I_{ph}) in ADT–TIPS–F and Pc–TIPS films. Power-law fits ($I_{ph} \propto t^{-\beta}$) are also shown. Offset along y-axis is for clarity. 69

3.11 (a) Normalized transient photocurrents obtained in an ADT–TIPS–F film at various electric fields. (b) Bottom: The total charge (Q), obtained by integrating transient photocurrent with respect to time, collected over 150 ps, 4 ns and 1 μs after photoexcitation of an ADT–TIPS–F film as a function of electric field. The power-law fits ($Q \propto E^{\alpha}$) are also shown. Top: Photocurrents (I_{CW}) obtained in the same sample under CW photoexcitation as a function of electric field. CW photocurrents measured at 532-nm excitation under dc conditions and at 365-nm excitation at a chopper frequency (f) of 390 Hz are shown. The power-law fits ($I_{CW} \propto E^{\alpha_{CW}}$) are also included. 70

Figure Page

3.12 Product of mobility and photogeneration efficiency, ($\mu\eta$), obtained from the peak transient photocurrent in ADT–TIPS–F, Pc–TIPS, DCDHF films (solid squares, open circles, and solid triangles, respectively) at 1.2×10^4 V/cm at 400 nm and in GaAs at 150 V/cm at 800 nm (solid diamonds) and 400 nm (open diamonds) as a function of temperature. A power-law fit ($\mu\eta \propto T^{-n}$)to the ADT–TIPS–F data, with n=2.3±0.2, is also included. 71

3.13 Product of mobility and photogeneration efficiency, ($\mu\eta$), obtained from the peak transient photocurrent in ADT-TIPS-F, Pc-TIPS, DCDHF films and GaAs at 400 nm as a function of applied electric field. Data from GaAs transients at 800 nm are also included. Power-law ($\mu\eta \propto E^{\alpha}$)fits are shown. 73

3.14 (a) CW photocurrent as a function of chopper frequency (f) obtained in the ADT–TIPS–F film at 1 mW/cm^2 (open squares) and 10 mW/cm^2 (solid squares) at 1.2×10^4 V/cm, as well as in GaAs at 1 mW/cm^2 at 150 V/cm, all at 532 nm. Power-law fits ($I_{CW} \propto f^{-\gamma}$), with exponents γ, are also shown. (b) Exponents γ as a function of light intensity obtained in ADT–TIPS–F, Pc–TIPS, and DCDHF films and GaAs. The lines are guides for the eye. 76

3.15 (a) CW photocurrent as a function of light intensity (I) obtained in an ADT–TIPS–F film at 20 Hz, 390 Hz and 1 kHz (solid, open, and crossed squares, respectively) at 1.2×10^4 V/cm, as well as in GaAs at 390 Hz and 1 kHz (solid and open diamonds, respectively) at 150 V/cm, all at 532 nm. Power-law fits ($I_{CW} \propto I^b$), with exponents b, are also shown. (b) Exponents b as a function of chopper frequency obtained in ADT–TIPS–F, Pc–TIPS, and DCDHF films and in GaAs. The lines are guides for the eye. 77

Figure Page

3.16 CW photocurrent as a function of temperature (T) obtained in ADT–TIPS–F, Pc–TIPS, and DCDHF films (solid squares, open circles, and solid triangles, respectively) at 0.8×10^4 V/cm and in GaAs (solid diamonds) at 100 V/cm at light intensity of 0.5 mW/cm^2 at 532 nm: (a) at a chopper frequency f of 1 kHz, and (b) under dc conditions. Double and triple symbols of different sizes correspond to different samples. (c) CW photocurrent in one of the DCDHF (triangles) and ADT–TIPS–F (squares) samples replotted as a function of 1/T: at f=1 kHz (solid symbols, left axis) and under dc conditions (open symbols, right axis). Arrhenius fits ($I_{CW} \propto \exp[-\Delta/(k_B T)]$), with corresponding activation energies Δ, are also shown. 79

3.17 Product of mobility, initial photogeneration efficiency, and carrier lifetime, $\mu\eta_0\tau$, obtained from CW photocurrents at 532 and 365 nm as a function of electric field. Power-law fits ($\mu\eta_0\tau \propto \mathrm{E}^{\alpha_{CW}}$) are also shown. 80

3.18 Product of mobility, initial photogeneration efficiency, and carrier lifetime $\mu\eta_0\tau$ as a function of temperature at 1.2×10^4 V/cm (organic films) and 1.5×10^2 V/cm (GaAs). 81

4.1 Molecular structures, clockwise from top: C_{60}, ADT-TIPS-CN (R = Si(i-Pr)$_3$), ADT-TIPS-F or ADT-TES-F (R = Si(i-Pr)$_3$ (ADT-TIPS-F), R = Si(Et)$_3$ (ADT-TES-F)), DCDHF, and Pc-TIPS (R = Si(i-Pr)$_3$). 90

4.2 (a) Optical absorption spectra of ADT–TES–F films, pristine and with dopants. (b) Transient photocurrents obtained in ADT–TES–F films, pristine and doped with 2% and 5% concentrations by weight of C_{60} at 1.2×10^4 V/cm and 30 μJ/cm^2 at 400 nm. (c) Transient photocurrents in ADT–TES–F films, pristine and doped with 10% DCDHF, Pc-TIPS, and ADT-TIPS-CN 91

4.3 (a) Transient photoresponse of ADT–TES–F films, pristine and doped with 2%, 5% C_{60}. Inset: Logarithmic plot of transient photoresponse (b) (a) Transient photoresponse of ADT–TES–F films, pristine and doped with 10% DCDHF, Pc-TIPS, and ADT-TIPS-CN. Inset: Logarithmic plot of transient photoresponse 95

LIST OF FIGURES (Continued)

Figure Page

4.4 (a): Amplitude of peak photoresponse as a function of dopant concentration (percentage by weight of C_{60}). (b): Log-log plot of normalized decay profiles, ADT-TES-F, 5% C_{60} doping vs. pristine ADT-TES-F. 96

4.5 (a): Amplitude of peak photoresponse for ADT-TES-F doped with: 10% DCDHF, Pc-TIPS, and ADT-TIPS-CN. (b): Log-log plot of normalized decay profiles, ADT-TES-F with 10% ADT-TIPS-CN doping vs. pristine ADT-TES-F. 97

4.6 (a) Dark current and CW photoresponse for ADT-TES-F, pristine and doped with 2 %, 5 % C_{60} (b) Dark current and CW photoresponse for ADT-TES-F, pristine and doped with ADT-TIPS-CN, Pc-TIPS, and DCDHF. Open symbols: CW, closed symbols: dark current . 97

4.7 (a): Amplitude of dark current and CW photoresponse as a function of dopant concentration, ADT-TES-F doped with C_{60}. (b): Amplitude of dark current and CW photoresponse as a function of dopant concentration, ADT-TES-F doped with Pc-TIPS, ADT-TIPS-CN, DCDHF. For each pair of bars: darker bar represents dark current; lighter bar CW photocurrent. 98

4.8 (a)ADT-TES-Films doped with Pc-TIPS, ADT-TIPS-CN, and DCDHF, concentrations 10% by weight: CW photocurrent, dark current subtracted. (b)ADT-TES-Films, pristine and doped with C_{60}, 2% and 5% by weight: CW photocurrent, dark current subtracted. 99

4.9 (a) DC transients, PVK, doped with C_{60}, 0.5%, 1%, and 2% by weight. (b) DC transients, ADT-TES-F, doped with C_{60}, pristine, 2%, 5% by weight. 101

4.10 Ionization energies for the materials studied in this Chapter. E_F, Fermi energy. 103

Figure Page

5.1 (a) Molecular structure (R = Si(i-Pr)$_3$ (ADT-TIPS-F), R = Si(Et)$_3$ (ADT-TES-F)), and optical absorption spectra of ADT–TIPS–F films. (b) Transient photocurrent obtained in ADT–TIPS–F films, on Au and Al electrodes, at 1.2×10^4 V/cm and 30 μJ/cm^2 at 400 nm. Inset: Transient photocurrents (I_{ph}) in ADT–TIPS–F films on loglog scales. (c) Transient photoresponse peak amplitudes vs. voltage, for Au and Al electrodes, thin fingers, back illumination. 109

5.2 Interdigitated electrode pair geometry, showing geometry using "thin" fingers and geometry using "wide" fingers. 112

5.3 ADT-TIPS-F thin films, amplitude of peak transient photoresponse as a function of applied voltage. (a) Au contacts, both thin and wide fingers. (b) Al contacts, both thin and wide fingers. 113

5.4 (a) ADT-TIPS-F films with aluminum contacts. Dark current and CW photocurrent. CW photocurrent minus dark current not shown; coincides on this scale with CW photocurrent. Voltage 0 – 100V. (b)ADT-TIPS-F films with gold contacts. Dark current, CW photocurrent and CW photcurrent minus dark current, voltage 0 – 100V. 114

5.5 (a) ADT-TES-F films with aluminum contacts. Dark current, CW photocurrent and CW photcurrent minus dark current, voltage 10 – 300V. (b)ADT-TESS-F films with gold contacts. Dark current, CW photocurrent and CW photcurrent minus dark current, voltage 10 – 300V. 115

5.6 Microsope view of coplanar electrode pair used for measurement of phoresponse as function of beam spot position in gap. 116

5.7 Top: Schematic of scan of coplanar gap. Bottom: photoresponse as function of position of beam spot in gap, for gold and for aluminum contacts. 117

5.8 (a) Gap: photoresponse to localized beam spot, as a function of spot position in gap, for 30, 50, and 100 V. Vertical dashed lines show positions of electrode edges, positive at 70 μm. (b) Power-law relation $I \propto V^{\alpha}$, showing linear relation with beam spot at mid-gap. (c) Quadratic relation for beam-spot near positive electrode edge. . 118

Figure Page

5.9 (a) Schottky anode-to-anode structure. (b) Detail at reverse-biased junction, showing reduction of barrier size from Φ_e to $\Phi_B = \Phi_e - \Delta\Phi$ due to Schottky effect. The effective barrier potential, due to the superposition of the image potential on the HOMO level, is shown as a red dashed line. (c) Detail, showing further reduction in magnitude of the injection barrier Φ_B due to interface dipole and resulting vacuum level shift Δ. 122

5.10 Fit of dark current data to Richardson equation, for ADT-TIPS-F thin films. (a) aluminum contacts, (b) gold contacts. 125

5.11 Top: ADT-TES-F, dark current, applied voltage 0 to 200V, fit to Richardson equation for thermionic emission. Bottom: Fowler-Nordheim plot of dark current for two different samples, for applied voltage 10 to 300 V. Data for voltages 150 to 300 fitted to Fowler-Nordheim tunneling theory. Fit yields value for κ (Equation 5.2). Assumption: 2μm effective gap size. 127

5.12 Dark current and CW - dark current, ADT-TES-F film on aluminum electrodes 130

5.13 CW photocurrent, in ADT-TIPS-F with gold electrodes, plotted to fit (a) the 2-D Mott-Gurney relation and (b) the 1-D (Geurst) version of the Mott-Gurney relation. 132

5.14 (a) ADT-TES-F Film on Al electrodes, thin fingers and wide, dark current data fitted to Richardson equation. (b) ADT-TES-F Film on Au electrodes, thin fingers and wide, dark current fitted to Richardson equation. 134

1 Plots of simulated currents due to free carriers (red) and polarization (blue). Left: linear. Right: logarithmic with respect to current (vertical axis). Top: Low μ (1 x 10^{-5}) for typical disordered organic material (e.g., DCDHF). Bottom: Higher μ (1 x 10^{-2}) for more ordered material (e.g., pentacene) 155

On the Photoresponse of Several Novel Functionalized Oligoacene
and Anthradithiophene Derivatives

CHAPTER 1
INTRODUCTION

1.1 Organic and inorganic semiconductors

The physical theories which account for the observed characteristics and behaviors of inorganic semiconductors have achieved immense sophistication and predictive power. The incalculable extent to which technologies based upon these materials have penetrated our lives is testimony to the depth and extent of our knowledge and understanding of them.

Although it was first observed, early in the last century, that there exist organic materials which share, to a certain degree, some of the characteristics of inorganics semiconductors, it was not until fairly recently that our working understanding of such materials reached a point where the possibility of commercially viable applications could be seriously considered (figures 1.1 and 1.2). Organic materials operate at a certain disadvantage; in comparison with organics, inorganics are in some ways far easier to work with and to understand, and they withstand environmental adversity (temperature changes, oxidation, moisture) much more robustly. On the other hand, the very depth and breadth of our mastery of inorganics makes it increasingly difficult to push the envelope, and the possibilities suggested by materials with many more degrees of freedom, which are in general much less well understood, and which have certain of their own advantages, become more enticing. Organics share certain of the useful features of plastics and of inks: they can be mechanically flexible, solution-processable, printable, even paintable. They are possibly much cheaper to produce and to process. Techniques of synthesing these materials have developed to the point where specific materials, with characteristics which meet specific requirements, can be synthesized.[1–3]

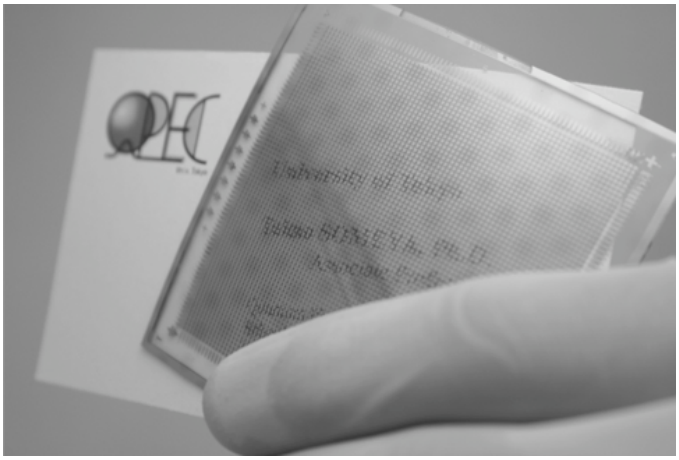

Figure 1.1. A clear, flexible, image scanner developed by S. Takao and his group, at the University of Tokyo.

In consequence, certain long-unanswered questions have become of much greater immediate concern.[4,6–10,63,92]

How much kinship is there between inorganic semiconducting crystals and those organic materials which have been found to be crystalline, conducting or semiconducting, and photoresponsive? One naturally hopes that the kinship may be found to be close, in view of the tremendous sophistication and power of the methods used with inorganics. Much could be accomplished, if these methods could be adapted in any way for use in work with organics. However, at the very beginning, one finds a crucial difference between the two classes of materials. The materials used in inorganic semiconductor applications – silicon, germanium, gallium arsenide and other compounds – form crystals through covalent bonding. One finds, in such materials (if pure), that charge, whether injected at electrodes or excited by incident light, can move very freely under the influence of an applied field, with long mean free paths, a high degree of delocalization, and a correspondingly great degree of shielding of the carrier from the Coulombic attraction of the nuclei of nearby atoms in the crystal. In contrast, organic crystals such as the polyacenes – anthracene, tetracene, pentacene – are complex molecules (polycylic aromatic hydrocarbons), and such materials are bound into crystals by Van der Waals forces. The bonding forces are much weaker, and overlap between the outer orbitals

of adjacent molecules, and screening, by electrons in inner orbitals, of the Coulombic interaction between carrier and nuclei, are much less. One might suspect from this that such materials would be perfect or almost perfect insulators. But, surprisingly, some of the polyacenes, pentacene in particular, can exhibit relatively high carrier mobilities, of the order of 1 $cm^2/(Vs)$ and higher, in ultrapure crystals. That's not metallic conductivity, of course, but neither can the material be called an insulator. Further, such materials have proven to be very optically active, with the possibility of fluorescence, photoconduction, perhaps even lasing. Particularly at low temperatures, mobilities may reach the same order of magnitude as inorganic semiconductors.

At the outset, then, it appears that the cornerstone of the theory of inorganic semiconductors, the band model, is of uncertain utility in the field of organic semiconductors. But neither can we summarily dispense with it. We will see in Chapter 2 that an important group of researchers, numbering among their members the Nobel laureate Alan Heeger, have for many years maintained the validity of the band model for organic semiconductors.

Silinsh and Capek, in discussions of the energy structure of polaron states in organic crystals, hold that the standard one-electron band model, with clearly defined valence and conduction bands, of some reasonable width in energy, separated by a significant energy gap, should be discarded.[11] They propose something like bands, but with a continuum of energy states rather than a gap between them. Another important feature of the band model, the Bloch function with **k**-vector a good quantum number, i. e., with mean free path much greater than the lattice constant, was challenged early on by Glaeser and Berry, at least for temperatures near room temperature.[14] On the other hand, there exists laboratory evidence which suggests some form of delocalization, even at room temperatures, for some of these materials.[8,42,45] Hence, for reasons of both practical utility and of theoretical convenience, some version of the band model remains current in research into organic crystals. For example, one often finds the HOMO and LUMO levels[1] doing service as "valence" and "conduction" bands, in discussions of

[1]Highest Occupied Molecular Orbital, Lowest Unoccupied Molecular Orbital

Figure 1.2. A commercially available OLED display unit, from Densitron Technologies

organic materials. Since it is believed that electron transport in organic crystals is movement – in some form – of excited electrons within the LUMO level of individual molecules and between LUMO levels of neighboring molecules, it may be valid to consider the LUMO level to be in some sense analogous to a "conduction band" and the HOMO level to a "valence band." However, both with respect to bandwidth and with respect to bandgap, there are fundamental differences with the band model as applied to inorganics.

1.1.1 Materials: Conjugated Polymers

Although conjugated polymers are not the focus of this paper, a great deal of work, some with direct implications for the work described here, has been done with polymers in the last few decades. In this research, particular attention has been paid to carrier dynamics in polymers, especially exciton dynamics. The nature of the primary photoexcitation remains a matter of dispute, and many of the questions regarding what happens on various time scales, from femtosecond to millisecond, after the initial photoexcitation, are much the same for organic crystals as they are for polymers.

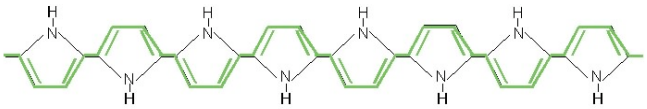

Figure 1.3. Example of conjugated polymer: polypyrrole. (From http://www.wam.umd.edu/ smela/conj_pols.htm)

Figure 1.4 shows schematically the basic structures of some of the main polymers of interest. Conjugated polymers are characterized by alternating single and double bonds between carbon atoms on the polymer backbone (Figure 1.3). When deposited by, e.g., spin-coating, as a film on a suitable substrate, they will not form crystals, but rather a sort of molecular spaghetti. The chains hinge, as it were, at the carbon bonds between successive benzene rings in the chain. The length of the chain is to some degree indeterminate. For these reasons, polymeric solids are amorphous, lacking the repeating unit cells characteristic of crystals. Undoped polymers typically have low conductivities, $< 10^{-2}$ cm^2/(Vs) at room temperature,[15] compared with mobilities for holes injected into pure polyacene single crystals (naphthalene, pentacene) of $\sim$1 cm^2/(Vs) at room temperature.[16]

In 1977 Heeger, MacDiarmid and Shirakawa discovered highly-conductive polymers,[17] for which they won the Nobel prize in Chemistry in 2000. If properly doped, such polymers have been found to have conductivities at room temperature close to that of copper.[18] However, unlike copper, their conductivity, doped or undoped, has been

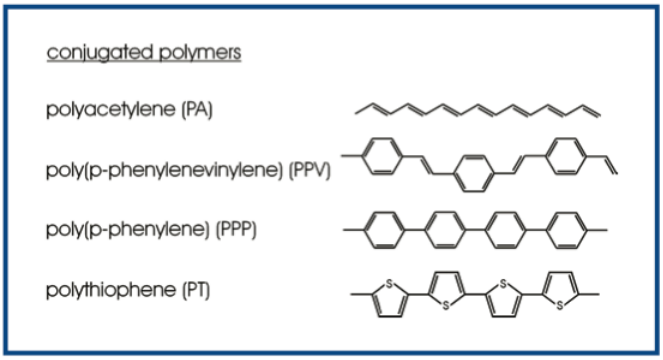

Figure 1.4. Structures of some conjugated polymers. (From F. Hegmann[63])

found to increase with temperature.[19] These materials are of a disordered nature, and such materials typically exhibit dispersive transport, as modelled by Scher and Montroll.[20,21] Such behavior is viewed as a random walk in a random array of hopping sites, within a regular lattice of cells made up of those sites. Such transport is also known as the *continuous time random walk* model (CTRW).

Research into these materials will be described in some detail in Chapter 2.

1.1.2 Materials: Polyacenes

Polyacenes are a sub-group of the conjugated aromatic hydrocarbons.[21] Some typical polyacene structures, may be seen in Figure 1.5. Unlike polymers, polyacenes have a rigid "backbone," of a fixed length, created by the succession of joined benzene rings.

The outer orbital configuration of a single molecule of a typical polyacene may be seen in figure 1.6. π-orbital electron clouds are formed above and below the plane of the molecule, through the overlap of the sp^2 orbitals of the carbon molecules of the benzene rings which form the anthracene "backbone".

The crystalline structure of a typical pure polyacene, the anthracene crystal, may be seen schematically represented at the bottom of Figure 1.5. Such materials crystallize in a "herringbone" structure. The overlap, in such materials, between π-orbitals in adjacent molecules of such a crystal, is not wide. This is referred to as "minimal

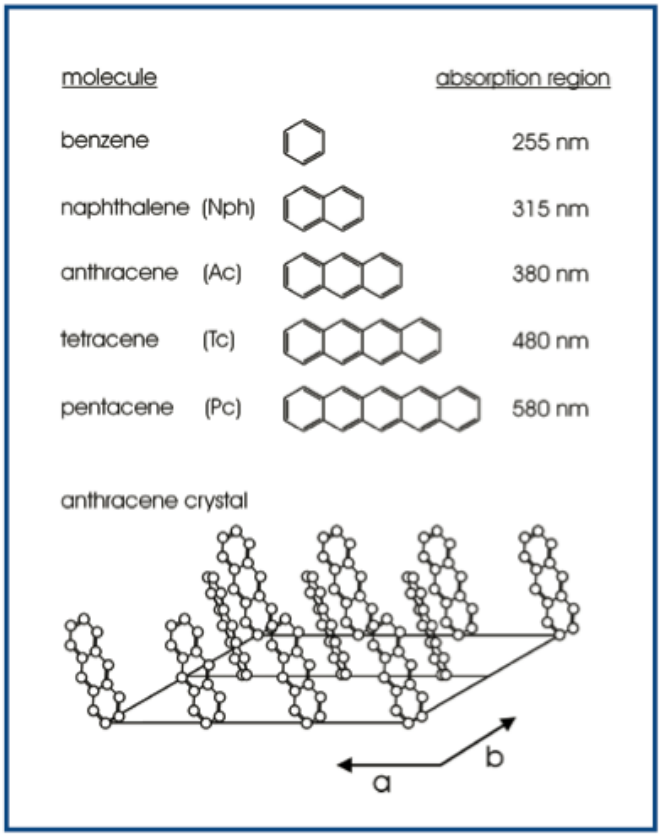

Figure 1.5. Structures of some polyacene molecules. The wavelength of the lowest energy absorption peak is also indicated.[21] (From F. Hegmann[63])

π-stacking." One of the important developments of the last decade has been the synthesis of "functionalized" polyacenes. John Anthony and his group at the University of Kentucky investigated the consequences of attaching additional groups to the pure polyacene molecule, typically to the midsection. They found that in this case, edge-to-face bonding, as is characteristic of the pure crystal, is prohibited, and a "pancake" or "brick wall" structure is formed,[22] rather than the herringbone structure. An example is shown in Figure 1.7.

The materials with which this thesis is principally concerned are the following: a novel fluorinated anthradithiophene (ADT) derivative functionalized with triisoproplysilylethynil (TIPS) side-groups (ADT-TIPS-F), a similar material, fluorinated

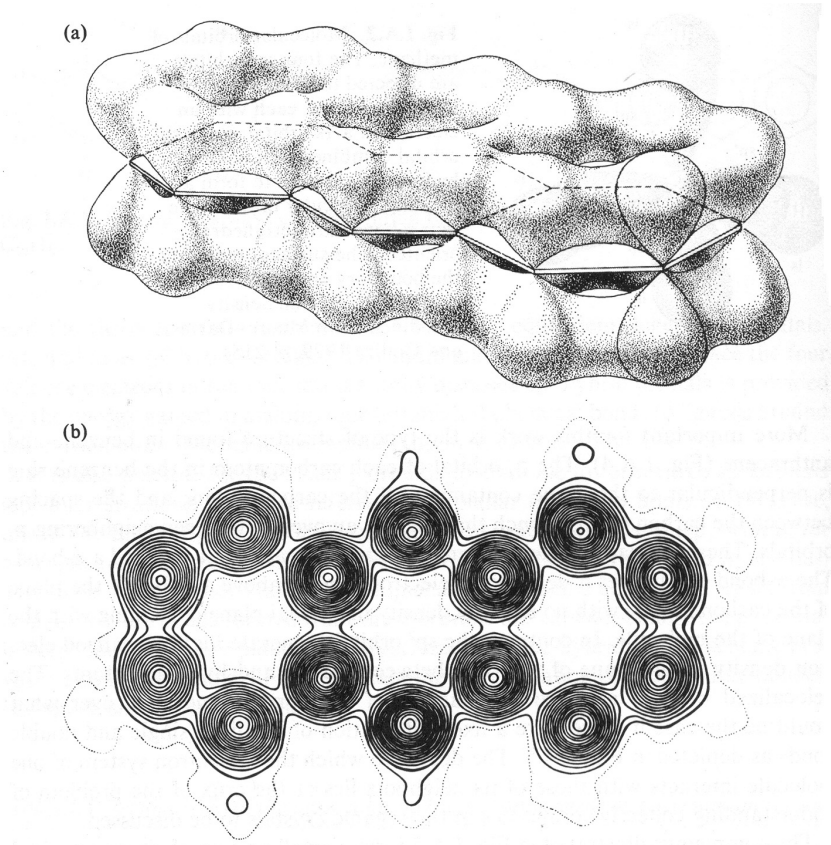

Figure 1.6. Schematic view of the lowest bonding orbital π-electron cloud above and below the plane of the anthracene molecule. The lower image is electron density sections through the central molecular planes in the anthracene crystal. (From M. Pope, C. E. Swengerg[21])

anthradithiophine functionalized with triethylsilylethynil side-groups, ADT-TES-F,[2] a pentacene derivative functionalized with TIPS groups (Pc-TIPS),[2,8,9,24] and a dicyanomethylenedihydrofuran (DCDHF) derivative.[3,25,26] DCDHF derivatives are glass-forming molecules originally developed for photorefractive (PR) applications; DCDHF-based monolithic amorphous glasses are among the best-performing organic photorefractives.[3,25,26] ADT-TIPS-F, ADT-TES-F and Pc-TIPS form very similar single molecules (Figure 1.8), but pack somewhat differently into crystals. Both pack in variants of the "brick-wall" packing structure, but the skew, so to speak, of the packing differs. Anthony has shown that the size and shape of the added side-groups or substituents has

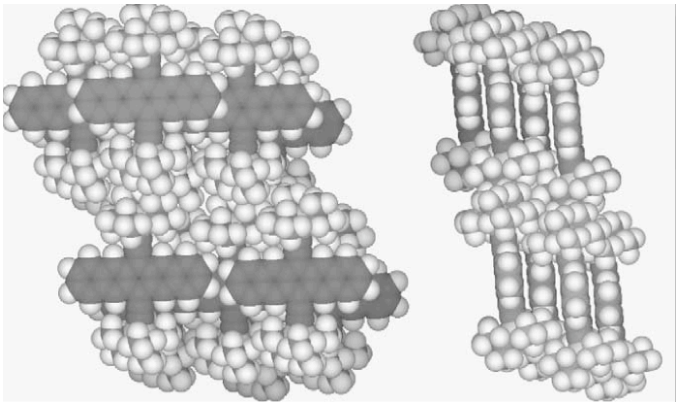

Figure 1.7. Functionalized pentacene-pendant structure: Pc-TIPS. From J. S. Brooks *et al*[23]

a marked effect on the crystal packing motifs characteristic of the bulk material (Figure 1.9).[2] ADT-TES-F, ADT-TIPS-F and Pc-TIPS all form 2-D π-stacks; the stacking for ADT-TES-F and ADT-TIPS-F is shown in Figure 1.9. Pc-TIPS and ADT-TIPS-F are triclinic, belonging to the space group P-1, with best-fit unit cell parameters: a = 0.755nm, b = 0.773 nm, c = 1.676 nm, $\alpha = 89.5$, $\beta = 78.7$, $\gamma = 84.0°$, and a = 0.758 nm , b = 0.8180 nm, c = 1.615 nm, $\alpha = 100.8$, $\beta = 92.6$, $\gamma = 98.8°$, respectively.[27] ADT-TES-F is also triclinic, with a = 0.721, b = 0.732, and c = 1.635 nm. Both ADT-TIPS-F and ADT-TES-F form larger lattices than pure pentacene (unit-cell parameters: a = 0.515, b = 0.60, c = 0.79 nm).

1.2 Electric Current in Organic Materials

A continuous flow of current through an organic material requires that carriers be injected into the material under an applied field (typically at a metallic electrode), that they be capable of transport through the material, and that they may be extracted at the other electrode.

Questions regarding the nature of these currents fall naturally, therefore, into several distinct but related categories. First, there are questions regarding the nature

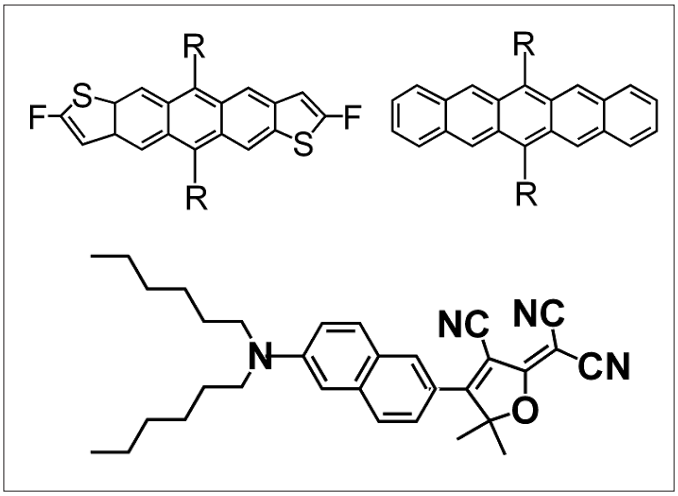

Figure 1.8. Molecular structure of materials used in this study: Clockwise from top left: ADT-TIPS-F, Pc-TIPS and DCDHF. For ADT-TIPS-F, R = Si $(i\text{-PR})_3$. For ADT-TES-F, R = Si $(Et)_3$.

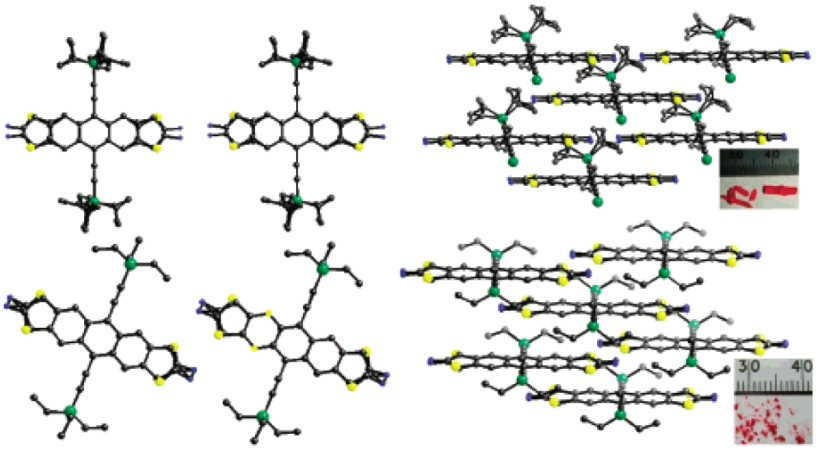

Figure 1.9. ADT-TIPS-F π-stacking (top) contrasted with that of ADT-TES-F (bottom). (From S. Subramanian.[120])

of the metal/organic interface at both electrodes, and the dynamics of carrier injection/extraction there. Then there are questions regarding what are called "intrinsic" characteristics of carrier transport (and possibly carrier generation), such as those which might be found in the interior of a very pure single crystal of the material. Next, there

are questions concerning transport through a more or less imperfect form of the material, one with crystalline domains and domain walls, defects, traps, and all the rest of the menagerie of imperfections found in real, less than ideal materials, as well as questions concerning surface effects and carrier behavior at surfaces and interfaces. Characteristics of transport arising from such factors are referred to as "extrinsic." Finally, there are questions regarding carrier transport as it may be enabled, assisted, or hindered by environmental factors external to the material, such as incident light or applied heat.

Moreover, continuous steady-state current is not the only form which current may take. There are also "transient" currents, such as arise from excitation by fast laser pulses, which generate short-lived populations of carriers, similar to those generated and dispersed in time-of-flight experiments. It is quite possible that carriers generated in this way may be of a very different species, with very different dynamics, from those which constitute the majority carrier in steady-state currents.[11] Carriers arising through photo-excitation may be generated on sub-picosecond time scales, but it may require nanoseconds, or longer, for carrier and lattice to relax into the configuration typical of steady-state current. Much can happen during the period of relaxation – trapping, phonon interactions, etc. There is at present a wide and growing body of data, some presented in this thesis, on the transient transport of these (possibly) short lived carrier species under the influence of an applied field. Although many potential applications of organic semiconductors may not make use of such transient photocurrents, their investigation is likely to bring to light much information which will help to improve our general understanding of the fundamental structure-property relations of these materials.

The data for currents in this thesis are therefore of three kinds: dark, steady-state, and transient. A current measured, in the absence of external influences (e. g., incident light), is referred to as "dark current."

1.3 Interfaces

The nature of the processes operating at the electrode/organic interface is still under investigation by many workers in the field.[12,13,116,117] This interface has often been pictured as a Schottky junction, but the applicability of that model to the organic/metal interface has been called into question in fundamental respects. For example, given the relatively low mobility of carriers in organic semiconductors, it is not clear that thermodynamic equilibrium and alignment of the Fermi levels of the two materials does indeed take place. Further, organic materials tend to form an interface dipole layer at the junction with the metal, which can result in a shift of the vacuum levels of the two materials relative to one another. This in turn has a direct effect on the height of the carrier injection barrier. These questions will be discussed in detail in Chapter 4.

1.4 Methods

There exists a wide variety of methods in this field. Here we will briefly discuss some characteristic considerations in the area of sample preparation, and at a few of the principal methods currently employed for the excitation of charge carriers, and for the subsequent measurements of their behavior.

1.4.1 Materials preparation

Polymer Preparation. These materials, since they do not form crystals, are often simply spin-coated onto the substrate of choice.

In a more fundamental, and more interesting, sense of the word "preparation," such materials may nowadays be doped, for example with one of the buckminsterfullerenes, such as C_{60}.[28] In the case of doping of polymers with C_{60}, since C_{60} is insoluble and otherwise difficult to work with, it is necessary to attach other organic groups to the C_{60} in order to attach it to a polymer. These dopants provide sites in the material which possess specific characteristics, i. e., hole traps (or electron acceptors) of known depth. Further, these characteristics may be known to operate on specific

time-scales. In this way, if one can compare behavior of the doped material, with high enough time-resolution, with behavior of the undoped material, one can then glean information about the behavior of the matrix in which the dopant resides, and about the associated time-scales.

Polyacene Preparation. The pure forms of the polyacenes tend to be insoluble in ordinary solvents such as toluene. Thin films are formed by vacuum deposition, crystals by such methods as vapor transport growth in argon flow. Thin films tend to be amorphous or polycrystalline, with small domains, typically less than 1 μm in length. Determination of intrinsic properties is very difficult in such films. Relatively large crystals can be grown, which aids in the determination of these properties, but their preparation tends to be time- and hardware-intensive.

Functionalized polyacenes, on the other hand, permit the deposition of thin films not from vacuum but from solution. Such films tend, again, to be polycrystalline, but this disadvantage is offset, to some extent, by the ease of preparation.

As in the case of polymers, one way of preparing these materials for investigations into energy structure and carrier dynamics is to dope them. They may be doped with C_{60} or they may be doped with organic molecules more similar to the host material. Chapter 4 will discuss results obtained from doping functionalized anthradithiophenes with C_{60}, with a dicyanomethylenedihydrofuran (DCDHF) derivative, and with two closely related oligoacenes.

1.4.2 Non-contact Methods: Optical Pump, THz Probe

The work of F. A. Hegmann and associates, may be taken to represent the general approach to the use of optical-pump THz-probe methods. In one of their setups, shown in Figure 1.10, the optical energy source is the output of an ultrafast, mode-locked Ti:Sapphire pulse laser, usually close to 800nm. The output pulses are used both to pump the sample material, and to generate the THz probe pulse, through optical rectification with an $ZnTe$ crystal,[29] or some other method. The probe is generally of far less intensity than the pump. The intensity of the THz probe signal, after transmission

through the sample, is detected and measured by a second ZnTe crystal. The time difference between the passage of the pump pulse through the sample, and the passage of the THz pulse, is varied by a delay stage. The time-resolution of the setup is typically not as good as the ultrafast pulse-width (∼400 fs, say, for a ∼100 fs pulse-width).

The THz pulse is of such a wavelength that it will not resonate with molecular energy levels. If there are no free carriers, the material is transparent to the THz pulse. Only if there are free carriers which can couple to the EM field of the THz pulse will there be any absorption.

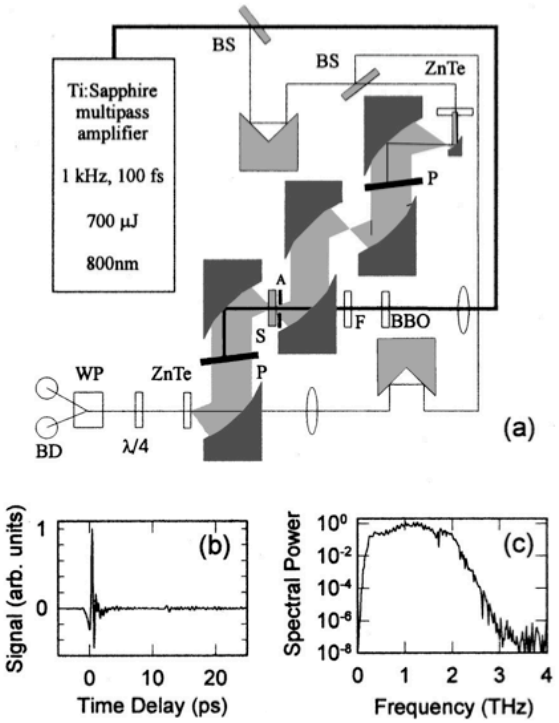

Figure 1.10. (a) Typical optical-pump THz-probe apparatus. BS: beam splitter; P: polyethylene visible beam block; F: blue filter; S: sample; A: 1 mm aperture $\lambda/4$: quarter-wave plate; WP: Wollaston prism; and BD: balanced detector. (b) Single-scan THz trace (FWHM 250 fs) and (c) spectrum obtained under dry N_2. From K. P. H. Lui [30]

The key to the method is the adjustable delay between the optical pump and the THz probe. If the pump has generated free carriers, this excitation will relax on

some time-scale. The free carriers will absorb THz optical energy, but as the excitation relaxes, its attendant absorption will decrease. The THz probe can be made by the delay stage to succeed the pump pulse at variable time intervals, and thus to measure the absorption as a function of delay time interval. Carrier dynamics can in this way be investigated on very short time scales, down to fractions of a pico-second. Figure 1.11 shows the transmitted THz probe pulse intensity $\triangle T$, as a function of probe delay time.

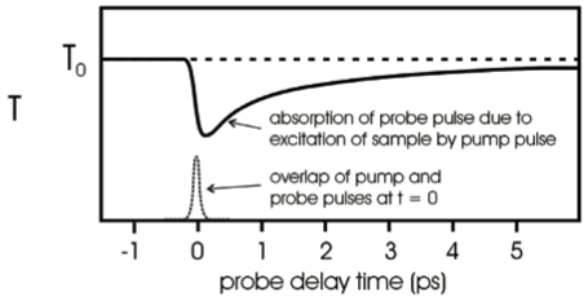

Figure 1.11. Transmitted pulse probe intensity as a function of probe delay time. From F. Hegmann[63]

The transient photoinduced absorption is normalized, as $\triangle T/T_0$, and typically plotted as $-\triangle T/T_0$ as in Figure 1.12, which thus shows the transmitted THz probe pulse intensity as a function of probe delay time.

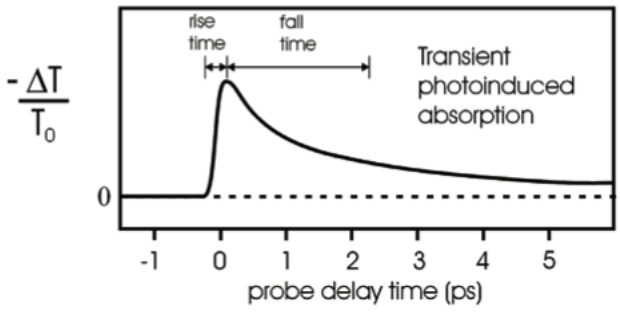

Figure 1.12. Transient photoinduced absorption as a function of probe delay time. From F. Hegmann[63]

1.4.3 Non-contact Methods: All-optical Pump-Probe

A typical all-optical pump-probe apparatus is seen in Figure 1.13. All-optical pump-probe methods can be used to investigate reflectivity, transmission, Raman scattering, and photo-induced absorption.[31] In cases where the probe pulse is desired to be swept across a wavelength band, one may focus the pump pulse into a material like water, ethylene glycol, or a glass fiber. One obtains then what is called "super-continuum generation," and a wavelength may then be selected from the continuum to use as the probe pulse. All-optical pump-probe methods do not differentiate between bound and free carriers. Hence this method can not be used for photoconductivity measurements.

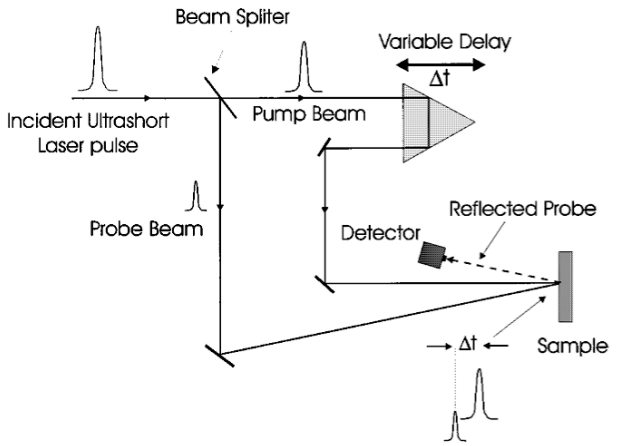

Figure 1.13. A typical excite-and-probe experimental setup. The ultrashort laser pulse is separated into a pump and a probe beam with a variable optical delay between them (Δt). The pump beam is normally used to excite the semiconductor, whereas the probe beam, typically much weaker than the pump beam, is used to measure the changes induced by the first pulse as a function of the optical delay between them. From A. Athonos [31]

1.4.4 Contact Methods: DSO

In contact methods, one seeks to examine the influence of environmental factors such as an applied field, or pressure. It has been found that methods such as optical-pump/THz-probe are hampered by the application of voltage across a sample, at least

a polyacene sample. The applied field introduces a prohibitive amount of noise. One therefore uses an instrument such as a high-bandwidth digital sampling oscilloscope (DSO) to examine photoresponse in real time.

The sample is prepared, for example, as a film on a suitable substrate (glass or mica). Electrodes are vapor-deposited metal; the work function must be chosen to be suitable to the particular material under investigation. Sample electrode may be simple coplanar, sandwich, or something more sophisticated. The sample is placed in a simple fixture, such as that shown in Figure 1.14. The fixture is usually so arranged that incident pump-pulses are normal to the film. Photoresponse, as photoinduced current, is read off the load resistor R1 as a voltage, by the DSO, and can readily be converted to current by Ohm's law.

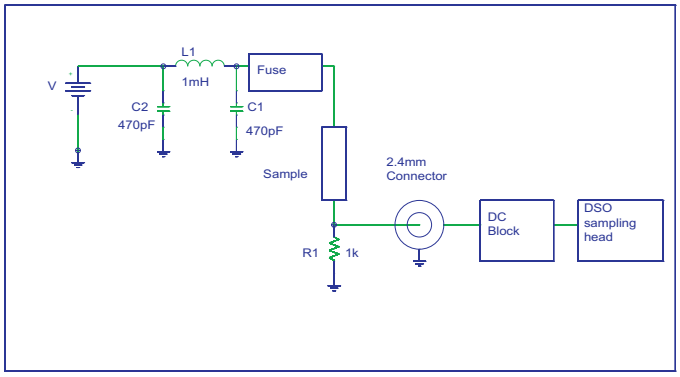

Figure 1.14. Schematic of fixture for measurement of transient photoresponse with an applied potential

1.4.5 Temperature and other environmental parameters

The observation of the variation of carrier behavior, however measured, under change in temperature is critically important to understanding the underlying transport dynamics. One of the principal observations which has been made in the process of investigating conductive polymers and polyacenes is that, in some cases, the change of carrier behavior under change in temperature is so fundamental that different models appear to apply in different temperature regimes. In other cases, certain of the key

parameters do not change at all. Hence, cryostats of various types have been widely employed, so that the behavior of carriers at temperatures down at least to 10 Kelvins have been investigated.[29,32]

Samples have also been placed in hydrostatic pressure chambers, to investigate the change in carrier mobility in pentacene and tetracene with change in pressure.[33] It was found that mobility goes up with pressure.

1.5 Overview of this Thesis

In the next chapter, an attempt will be made to discuss some of the published scientific literature relevant to the research described in this thesis. The literature is larger than vast; it is hoped only that the articles and books discussed in that chapter are a few of the more relevant. The principal topic of Chapter 2 will be a discussion of a debate, some decades old and still ongoing, regarding the actual nature of the charge carriers in organic semiconductors, both on very short time scales (relevant to carriers arising from very brief optical excitations), and on long time scales (relevant to steady-state currents, with the influence of incident light and without it (dark currents)). Chapter 3, the heart of the thesis, describes an extensive investigation of the electrical and photo-electrical characteristics of some novel polyacene and anthradithiophene derivatives, on time scales from ∼30 picoseconds to many seconds. Chapter 4 extends this investigation, describing experiments in which the effects of doping on the electronic behavior of two novel anthradithiophene derivative are investigated. This is of practical significance, for purposes of device design, and sheds some light as well on the energy structure of these materials, and on the way it shapes the transport of charge through them. Chapter 5 discusses investigations into the way the behavior of simple systems in which these materials are embedded is changed, when the metal of the contacts with which they interface is changed. The final chapter will summarize the research, and discuss the conclusions derived from it.

CHAPTER 2
BACKGROUND

2.1 Carrier Photogeneration

Organic materials were found, over a hundred years ago, to exhibit photoconductivity. But despite extensive investigation, important questions regarding the nature and dynamics of this phenomenon remain open. First, what is the form of the primary photoexcitation? That is, on extremely short time scales, immediately after a photon hits but before the excitation has time to propagate or to interact with the lattice, what has happened? Next, what is the subsequent evolution of the excitation – especially under conditions of applied electric field?

In recent years, different views of these issues have emerged. These may be placed upon a spectrum with, at one end, the view that the carrier dynamics in question are much like those in inorganic semiconductors, and with the opposing view at the other end. This latter view, in which nothing like a true band model is held to be appropriate for understanding organic semiconductors, is the consensus view at present. Most workers believe that the primary excitation is an exciton, a bound hole-electron pair, which must dissociate, through thermal activation or through the action of an applied field, or both, in order to give rise to free carriers.[34–39] No less an authority than Pope and Swenberg state unequivocally that, "In molecular crystals, it is well established that autoionization is the dominant process for the intrinsic generation of free carrier pairs."[21] Nevertheless, there is another view – held principally by Daniel Moses and his group – that sees evidence that at least some of the primary photoexcited species are

in fact free carriers, generated without the intermediate stage of exciton formation and dissociation. These two models are illustrated in Figure 2.1.

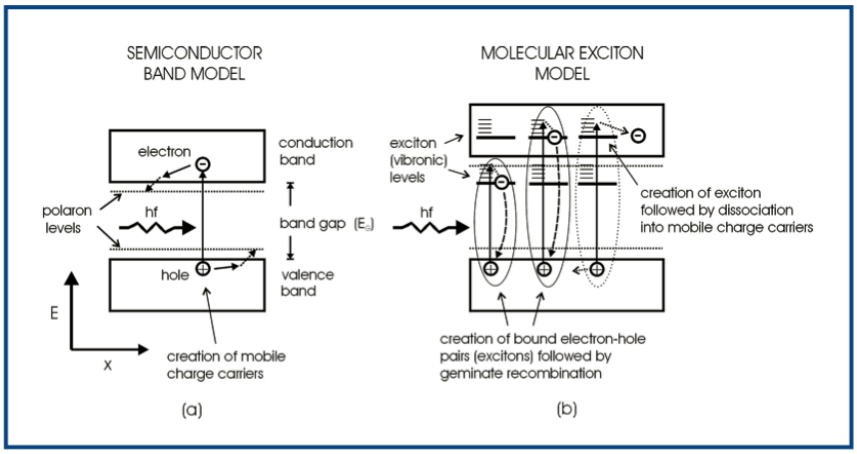

Figure 2.1. Energy band diagrams of photoexcitations in organic semiconductors according to (a) the semiconductor band model and (b) the molecular exciton model. (From F. Hegmann.[5])

Carriers in organic semiconductors can arise as a byproduct of doping the material, as is often done with polymers, or they can arise through thermal, electrical or optical stimulation. Carriers may be generated in undoped polyacene or functionalized polyacene crystals by means of applied fields, as in field effect transistors (FETs) or by means of incident light. Such light may be CW (continuous-wave) or it may take the form of pulses.

If an incident photon is energetic enough, it can excite an electron from the ground state into a higher energy state. In inorganic semiconductors, where the band model applies, such an electron is almost immediately promoted to free carrier status. But in organic crystals, in the molecular exciton model, an incident photon with only enough energy to generate an exciton has not succeeded in generating free carriers. Here, the excitation consists of neutral, bound electron-hole pairs, which require an applied potential, or scattering from a phonon, or a thermal action to be dissociated into mobile carriers.[5,34] As can be seen from Figure 2.1, such a minimally energetic, dissociated, exciton will almost immediately experience what is called "geminate recombination."

Geminate recombination is the reunion of hole-electron pairs arising from the same molecule.[21] The quantum yield of free carriers (defined as the ratio between the number of free carriers generated and the number of incident photons, typically labelled η) will in this case tend to be quite small. The trajectory of the elements of the pair from initial separation at excitation back towards recombination is viewed as a random walk, like the movement of particles in Brownian motion. It will require a photon energy significantly higher to generate an exciton in which the hole-electron pair has enough energy for this random walk to lead to dissociation and to the formation of free carriers. This is the Onsager model.[11,21,40,41] The relation between photocarrier quantum yield and applied electric field is an important signature of materials obeying this model. Typical curves for the Onsager relation betwenn quantum yield and applied field strength may be seen in Figure 2.12.

A material with structure which fits this model will show a quantitative difference between two parameters: the absorption edge of the optical spectrum, and the photon energy necessary to generate photoconductivity. When an absorption spectrum is taken, leading to a spectrum like that in Figure 2.2, one observes a threshold wavelength, above which there is no absorption. This edge is at around 750 nm in this case, that of pure pentacene film on either glass or mica. This wavelength corresponds to a photon energy of 1.8 eV. But if the material obeys the Onsager model, then when one obtains data for the photon energy/wavelength corresponding to the onset of photoconductivity, one finds that incident light of 1.8 eV is not sufficient to generate photoconductivity. This onset requires incident light of an energy around 2.2 eV for pure pentacene. In other words, according to this model, incident photons with energies between 1.8 eV and 2.2 eV are absorbed and generate excitons which, however, experience geminate recombination and do not form carriers. Incident light of energies equal to or greater than 2.2 eV is required to overcome the Coulombic interaction between the electron and the hole, allowing an external field or thermal activation to dissociate the two into free carriers.

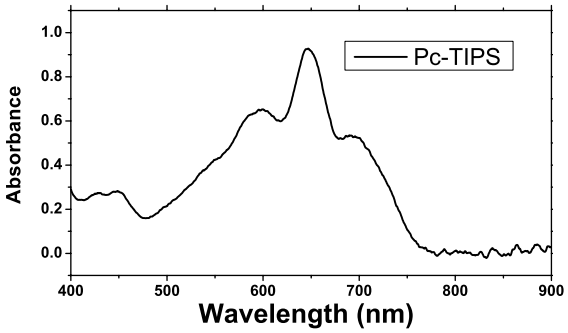

Figure 2.2. Example spectrum of pure pentacene films showing absorption edge at 750 nm.

In the band model, incident radiation of the correct frequency excites electrons in the organic material into "bands" – that is to say, this model views the excited state as electrons (and, by implication, holes) occupying energy levels or "conduction bands", in which they move as free, de-localized carriers .[42] Mere inspection of a typical organic crystalline structure such as that in Figure 1.7 may raise doubts about the applicability of the band model to such structures. But "band-" or "band-like" behavior has nevertheless been observed in organic materials, especially at low temperatures .[29,43] One of the signatures of band- or band-like behavior, in point of fact, is an increase in conductivity with a decrease in temperature. On the other hand, the exciton model leads one to expect the opposite, since dissociation of exciton pairs into mobile charge carriers happens more readily as the temperature goes up.

2.2 Carrier Transport

In the organic crystal, molecules are bound by Van der Waals forces rather than ionic or covalent, and hence the ovelap integral between states on one molecule and those on another is relatively small. Consequently, carriers tend to be more localized than in inorganic crystals (Silicon, GaAs), and to interact more strongly with the crystal lattice

at room temperature, i.e., to form polarons [11,44] whose effective mass is many times that of an unbound electron or hole, or that of a carrier in an inorganic semiconductor. Carrier transport is thought by some to take the form of hopping transport of polarons (from molecule to molecule), at room temperature, shifting to a more band-like behavior, with longer mean free paths, at low temperatures.[11,44] Such behavior, marked by the signature of an increase in carrier mobility, or of transient photoresponse, at lower temperatures, has been noted by many.[29,45] But the exact dynamics behind such behavior remain very much an open question.

If one is investigating organic crystals, it is worthwhile to remember, as was pointed out by Pope,[21] that molecular crystals can be highly anisotropic, and that both modes – hopping and band-like transport – can coexist in the same crystal, depending on the orientation of carrier motion with respect to the crystallographic axes.

There is no reason to deny *a priori* the possibility that, in a given electronic process in an organic crystal, several perhaps very different species of carrier may be present at the same time. In such a case, the contributions of each type of carrier to a measured process, such as a transient photocurrent, must somehow be teased apart from one another. This is the approach taken in Chapter 3, in which two populations of carrier are posited: one with carriers in "extended states," the other with "thermally assisted" carriers, hopping from trap to trap or from site to site. It is argued there that differences in observed carrier behavior (photoresponse) under different circumstances, or on different time scales, are due to differences in the relative proportions and contributions of the two populations. (A similar and analogous problem is discussed in Chapter 3, Section 3.3.2, in which work is briefly described showing that it is possible that a transient photocurrent attributed solely to mobile free carriers may in fact be receiving a substantial contribution from displacement current.)

To take the first type first, what are called extended states are states in which carriers are to some extent "delocalized." The most delocalized states are those for which a Bloch function may, at least in principle, be defined. The essence of a Bloch function is that it is a wave function defined for a particle moving in a periodic lattice environment,

a wave-function whose periodic waveform is a summation of a relatively small spread of Fourier components, and whose position is "smeared out" to a corresponding degree, in keeping with the Uncertainty Principle. A particle described by a Bloch function does not fit within a "wave packet," and has in no meaningful sense a location within the crystal. It is more like the modes or quanta of light in a laser cavity which, though we may refer to them as "photons," must also not be imagined to be particles with well-defined positions, like tiny billiard balls bouncing back and forth between two mirrors. Concomitant with this quantum description is a classical or semi-classical description, which says that the mean free path of the carrier described by a Bloch function is relatively long. Organic molecular crystals are spatially far more complex than inorganic crystals, and it is not clear how a carrier in such a crystal, with Van der Waals binding and weak overlap between molecular π and $\pi*$ orbitals, can have a mean free path (l) much longer than the lattice constant (a_0). Nor is it clear how it might move through the crystal in a manner for which a Bloch function, or something closely analogous to a Bloch function, could be defined. Scattering events at room temperatures are of a frequency which seem to render the sort of coherent transport found in inorganic crystals impossible.

Nonetheless, we will see below that since the mid-1980s some workers, principally Daniel Moses and his associates, have maintained that some of the signature behaviors of organic semiconductors cannot be explained other than by invoking a band model, with carriers occupying, at least on very short time scales, states which are delocalized to a degree which suggests that Bloch functions may exist for these states. This necessarily implies relatively long mean free paths.

LeBlanc, in 1961[46] performed the first band-structure calculations for anthracene crystals, using the tight-binding approximation, and concluded that the effective band-widths for electrons and holes were very narrow. His results were controversial, but supported the notion of carriers in anthracene being localized charges rather than charges in a band. Glaeser and Berry argued in 1966[14] that the band model was not applicable to crystals of the anthracene type (Ac). Their contention was that the charge

carrier interacts so strongly with lattice vibrations that the **k**-vector is not conserved, and wavelike carrier motion is replaced by a Brownian-like thermally assisted hopping motion. The criterion cited by Silinsh *et al*[11] for the applicability of the band model is that $l \gg a_0$, that is, that the mean free path of the charge carrier is much greater than the lattice constant.

The principal signature of carrier transport via thermally-assisted hopping is a direct, positive dependence of carrier mobility on temperature. But different dependencies from this have in fact been observed, both weak or no dependence in the case of the polymer *p*-phenyl vinyene (PPV) and its derivatives, and negative dependence in the case of organic crystals. In consequence, models based on carrier generation via exciton dissociation, and transport via hopping, have had to be modified, as will be discussed below. On the other hand, the body of evidence which supports relatively large binding energies for excitons in these materials is large and growing, and models which appeal to some form of coherent transport, at least on short time scales, with correspondingly weakly bound excitons, must relate these models to that evidence.

2.3 Problems with the Onsager model

Daniel Moses and his associates have worked since the late 1980's with a variety of polymeric materials.[1] He has consistently maintained the applicability of the band-model, or the invalidity, for the polymers with which he has worked, of the Onsager/molecular-exciton model.

2.3.1 1987: Polydiacetylene

In work done in 1987,[45] Moses, M. Sinclair and A. Heeger looked at transient photoconductivity in polydiacetylene, using the Auston switch technique in a setup

[1] with poly (*p*-phenylenevinylene), with polydiacetylene-(*bis* *p*-toluene sulfonate (PDA-TS), with poly(*p*-phenylene vinylene) (PPV), with poly [2-mehoxy,5-(2'-ethylhexyloxy)-*p*-phenlyene vinylene] (MEH-PPV) and poly[2,4-*bis*(cholestanoxyl)1,4-phenylene vinylene] (BCHA-PPV), both MEH-PPV and BCHA-PPV in synthetic combination with C_{60}, with α-octithiophene, *trans*- polyacetylene, wth poly(2,5-*bis*-[*N*-methyl-*N*-hexylamino]phenylene vinylene (BAMH-PPV)

giving 50 ps time–resolution. The transient photoresponse curves they observed showed a "fast initial response, followed by a fast decay to a more slowly decreasing 'tail'." These photocurrent curves were integrated over different time scales, to yield figures for total charge transported in a given time interval. The fast initial component was integrated to yield charge $Q_{initial}$, the slower "tail" component integrated to yield Q_{tail}. The fast initial component $Q_{initial}$ was found to be independent of temperature, implying that the product of the quantum efficiency η and the probability ϕ of escaping early-time recombination was independent of temperature. (The quantum efficiency η, in this context, is the number of generated e-h pairs per incident photon.) Q_{tail}, on the other hand, varied directly with temperature T (the exact relation was not determined), suggesting some form of thermally activated transport on longer time–scales after the initial excitation.

By varying the gap of the Auston switch, and by inspection of the resulting transient waveforms, they determined that the carrier mobility μ was independent of field strength. It was also observed that photocurrent was linearly dependent on field strength E. Using $\sigma = (\eta\phi)\mu eN$ and $j = \sigma E$, where N is the incident photon density, these observations led to the conclusion that the $\eta\phi$ product was independent of electric field strength.

These implications were held to be in unambiguous disagreement with the Onsager model. In Moses' interpretation, that model predicts that the quantum yield should vary as the probability of escape from geminate recombination, and is both thermally and E-field assisted, contrary to his group's findings.

The general conclusion was that the Onsager model was inapplicable to the material under consideration (a polydiacetylene derivative). It was proposed that the behavior observed was due to the presence in such conjugated polymers of broad π bands, in which carriers may be extensively delocalized.

2.3.2 1993 – 1994: PPV

In 1993 Moses *et al* performed experiments with MEH-PPV sensitized with the buckminsterfullerene C_{60}.[28] Transient photoresponses curves were fit to the following equation:

$$I_{ph} = A_1 e^{(-\frac{t}{\tau_1})} + A_2 e^{(-\frac{t}{\tau_2})} \tag{2.1}$$

where τ_1 and τ_2 are the lifetimes of two components of the transient response, fast and slow. The coefficients A_1 for the fast component and A_2 for the slow were mapped later (1994) against temperature;[43] they are mapped in this study against C_{60} concentration. Small concentrations (1%, 2%) make the most difference, overall. Increasing concentration from 5% to 50% makes a great difference to the fast component A_1 ($\sim$ factor of 4), but little difference to the slow component A_2 ($\sim$ factor of unity). The time constants τ_1 and τ_2 ranged, for C_{60} concentrations from 1 % to 50 %, from 320 ps to 523 ps, and from 1.86 ns to 9.89 ns, respectively. The C_{60} acceptors make a greater difference to the fast component than to the slow because the fast component pertains to "pre-trapping transport", when the excitation is not yet localized; the slow component pertains to transport when the effects of trapping have come to dominate, and transport becomes a thermally–activated trap–and–release process. The C_{60} electron acceptors have then formed "localized electronic states below the mobility edge"; they presumably have accepted their full complement of electrons and, even should they be present in greater numbers, this will make less difference to transport on longer time scales.

Higher concentrations of C_{60} probably make less difference, especially on the nanosecond time scales of the photoresponse decay "tail," because the probability of recombination increases with increasing proximity of holes to electron acceptors, as the density of the C_{60} increases, which damps its enhancement effect.

The bi-exponential fit is applicable to short time-scales (5 ns). On longer time-scales, the loglog plot fit is a power-law. This is said to be "characteristic of dispersive transport" (in disordered systems).

In MEH-PPV Moses found a quasi-linear dependence of the peak photocurrent (PC) on beam intensity, PC $\propto I^{0.9}$. This is what one expects, if the mobility μ and the quantum efficiency η are independent of intensity, and one can use simply $j = \sigma E$, $\sigma = ne\mu$, $n = \eta N_{photons}$, where n = carrier density. The temperature dependence of peak PC was weak (Fig 2.3). This implies a weak temperature dependence of efficiency or mobility or both. The view, again, was that such behavior was characteristic of "pre-trapping transport," i. e., of transport on short time-scales, when the excitation is still delocalized and perhaps coherent. On the other hand, the slow component, that belonging to the tail of the decay profile, was found to be thermally activated, which would be more characteristic of carriers in localized states.

The continuous-wave (CW) PC dependence on beam intensity was found to be slightly sublinear: PC $\propto I^{0.8}$. A linear relation is what we expect, again, if mobility and quantum efficiency are independent of intensity. On the other hand, the CW PC dependence on electric field strength was found to be superlinear, PC $\propto E^{1-1.5}$.

In 1994, Moses and his associates pursued further these investigations into transient photoconductivity in PPV.[43] They found the same kind of transient response, with a fast initial component of the transient photocurrent, with a decay time of about 100 ps, followed by a slower component with a decay time around 600ps. They attributed the fast component to polarons and the slower component to bipolarons. They also found, with this material, that the onset of photoconductivity and the optical absorption edge were the same, behavior they held to be consistent with the band model. Both polarons and triplet excitons are formed. It was held to be "likely" that polarons were formed at short times, bipolarons later. Transient curves were fitted again to Equation 2.1. In this case, the values extracted, from best fits of this equation to transient decay curves, for τ_1 and τ_2 were much shorter than in the earlier work with MEH–PPV doped with C_{60}, 128 ps at room temperature for τ_1 and 601 ps for τ_2. The extracted values for the

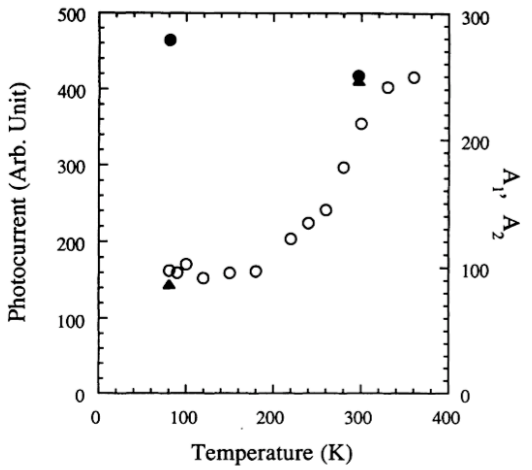

Figure 2.3. Temperature dependence of the peak transient photocurrent from 360 to 81 K (open circles); the magnitudes of the fast (solid circles) and slower (solid triangles) components at 297 and 81 K are indicated. (From Lee *at al*, PRB **49** 2396 (1993)).

two components (A_1, A_2) are plotted with respect to temperature in Figure 2.3. The fast component varied linearly with respect to beam intensity, photoresponse $PR \propto I^1$, "consistent with interband transitions." (In contrast, exciton dissociation is expected to have a quadratic dependence on intensity.[43]). On the other hand, the slow component $\propto I^{\frac{1}{2}}$. This was associated with formation of bipolarons from polarons. While the slow component decreased with decreasing T, consistent with thermally–activated trapping/detrapping transport, the fast component was again found to be independent of T (Figure 2.3), which was "unambiguously inconsistent with the Onsager model." Rather, this behavior was interpreted in terms of "interband transitions."

In this work, Moses and his associates addressed the question whether the transient photocurrent observed in organic semiconductors on short time scales was in fact due, not to the movement of free carriers, but rather to a displacement current, arising from the polarization of bound pairs with a large binding energy. Their approach was to assume that the answer was yes; i.e., assume binding energy is great, and inquire whether this assumption led to any absurdities.

The polarizability may be written as

$$\alpha_{exc} = \frac{1}{\epsilon_0 N_{exc} E} \int_0^\infty j(t)dt. \tag{2.2}$$

Their measured transient waveforms were integrated in accord with this equation, to obtain $\alpha_{exc} \approx 10^6 \text{Å}^3$. This value is two orders of magnitude greater than that obtained by Weiser for PDA-DCHD,[47] with polarizability $\alpha_{exc} \approx 8200 \text{Å}^3$. Hence the exciton binding energy in PPV must be proportionately *smaller*, since the polarizability and the binding energy are inversely proportional. The binding energy for PDA-DCHD = 0.4 eV; so two orders of magnitude smaller yields a binding energy of 4 meV. Under the assumptions made in the argument, this must be taken to be an upper value for the binding energy. This implies that the original assumption of polarized and tightly bound excitons, generating a transient displacement current under the influence of an applied electric field is invalid.

More can be said about exciton binding energy. The relevant equation is

$$E_{opt} = E_g - E_{exc}, \tag{2.3}$$

where E_g is the "single-particle energy gap," E_{opt} is the optical energy gap, and E_{exc} is the exciton binding energry. If the exciton binding energy is small, E_g is very close to the same as the energy for the interband optical $\pi - \pi*$ transition E_{opt}. However, if electron and hole are tightly bound, the $\pi - \pi*$ transition energy will be measurably less than the injection-energy gap. But Eckhardt[48] found the two to be same, hence E_{exc} must be small.

2.3.3 1995: Electron transfer polymer-to-fullerene. MEH–PPV

In 1995, Moses' group returned to work with MEH-PPV doped with a fullerene, in this case the methanofullerene [6,6] PCBCa.[49] The method used was to compare the photoinduced absorption, using pump-probe methods, in pure MEH–PPV and in MEH–PPV doped with 2 % and 50 % [6,6] PCBCa.

The model employed here viewed excitation as a "charge-separated state," with the electron on the fullerence acceptor, leaving a hole 50 monomer units away, on the average. It was proposed that the fast initial decay (Fig 2.4) in the photoabsorption results from geminate recombination of the initial excitation (although they did not call it exciton recombination). The fast decay can be prevented by 2% addition of [6,6] PCBCa (acceptor). If the excited electron does not get accepted, it geminately recombines. Let it be assumed that the excitation is localized to one monomer. The average distance between the initial excitation site and the acceptor is 50 monomer units. The diffusion length $l \approx D(t)^{1/2} \approx 100$Å, where D = diffusion constant, t = travel time ($\approx$ 700 fs). The diffusion constant D was estimated to be on the order of $D \approx 1$ cm^2/(Vs). Einstein's relation for mobility μ in a nondegenerate electron gas, $\mu = eD/k^BT$ was used to estimate mobility: $\mu \approx 10$ cm^2/(Vs). This value is far too large for conjugated polymers. The conclusion, then, was that the spatial extent of initial photoexcitation was much greater than the size of the monomer repeat units; that is, *the excited state is delocalized.*

2.3.4 1996: Transient photo-conductivity and -luminescence in PPV at high fields

Moses' and his colleagues' results up to this point may be summarized as follows: Fast transient photoconductivity (TPC) in conjugated polymers like PPV is independent of temperature, and linearly proportional to E-field and to beam intensity. The displacement current is too small to matter. These results imply that the quantum efficiency η must be independent of temperature and E-field. We get the same number

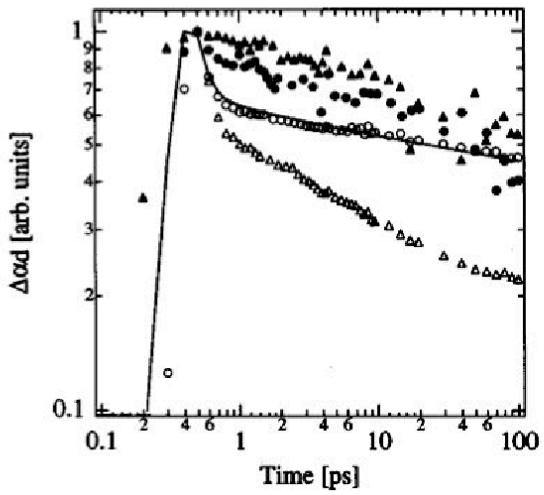

Figure 2.4. The time dependence of the PIA of MEH-PPV/[6,6]PCBCa (2%) at 1.45 eV (open circles) and at 1.2 eV (open triangles), and of MEH–PPV/[6,6]PCBCa (50%) at 1.45 ev (closed circles) and at 1.2 eV (closed triangles). (From Kraabel *et al* J. Chem. Phys. **104** 4267 (1996))

of carriers per incident photon, regardless of temperature and E-field. That is to say, generation of carriers is not thermally- or field-assisted. "Illumination by light with photon energy greater than the absorption edge generates carriers that **promptly** contribute to the photoconductivity.... As the carriers thermalize to the band edges, they **may** form weakly bound excitons." (Emphasis added).

In work in 1996 with samples of PPV oriented by tensile drawing, Moses' group examined transient photoresponse, using the Auston switch technique as before, but at electric fields up to 10^6 V/cm.[50] The peak transient photocurrent was found to be, again, independent of temperature. (Fig 2.5). Both the photocurrent and the dark current were linear with respect to E–field, up to 5 x 10^4 V/cm. This linear dependence is "consistent with direct photogeneration of charge carriers that then move with a constant field-independent mobility." (Using, again, $j = \sigma E$, $\sigma = ne\mu$, $n = \eta N_{photons}$). Dark current, however, is not independent of T (Fig 2.5).

Moses took note of an argument by R. Kersting's,[36] a member of Bässler's group, that quenching of photoluminescence due to an applied E-field means that excitons

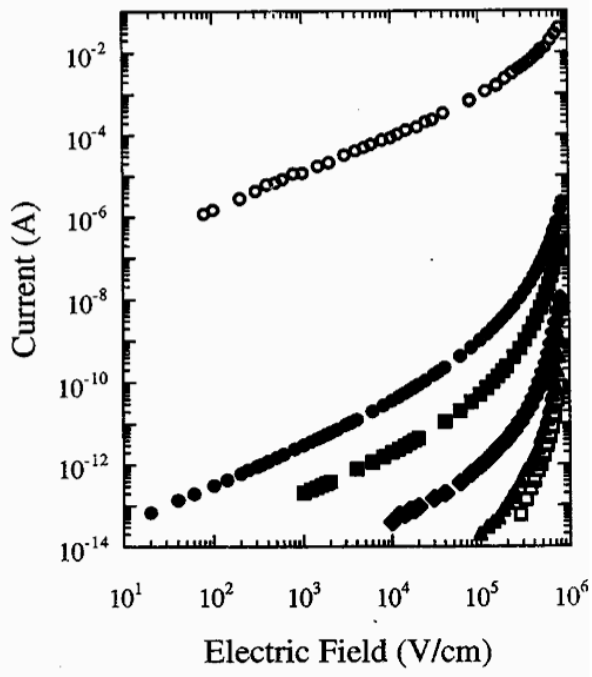

Figure 2.5. The dependence of the peak transient photocurrent (I_P) and dark current (I_D) on external field at various temperatures in tensile drawn, oriented PPV, $l/l_0 = 10$. The top curve (open circles) shows that I_P is temperature independent. The lower curves represent I_D: 300 K (solid circles), 250 K (solid squares), 200 K (solid diamonds), 150 K (solid triangles), 100 K (open squares). From Moses *et al* (1996[50]

(which would otherwise recombine & luminesce) are dissociated by field and do not luminesce. Therefore the primary photoexcitation is excitons. Moses' response was that "photoconductivity linear in E is observed in fields that are orders of magnitude below the onset of photoluminescence quenching." (p. 4751)

2.3.5 2000: IRAV

Moses' work in 2000 was based on the following facts, or postulates: 1) that the backbone of a neutral conjugated polymer is characterized by even-parity Raman vibrational modes, and 2) that carriers introduced to the backbone will break the parity

and transform those modes into infrared-active vibrational modes (IRAV).[2] The IRAV modes are distinguished from the "normal" IR-active modes by being in 1:1 correspondence with the strongest Raman-active modes. This is revealed by resonant Raman scattering. The IRAV modes are "turned on" by local charges, whether introduced by doping or by photoexcitation. Hence IRAV absorption provides a means of probing the carrier density.

Moses and his group used a modified Spectra Physics OPA system. It generated pump and "idler" beams, at frequencies ω_i and ω_s. These were mixed in a nonlinear $AgGaSe_2$ crystal to generate the probe beam, at $\omega_{probe} = \omega_s - \omega_i$, which could be tuned to the desired probe frequency. For the pump beam, they used the fundamental, first and second harmonics of the laser, at 800 nm, 400 nm, and 267 nm.

In their experiments, photo-induced absorption (PIA) – or, in this case, photo-induced scattering – was detected only when the probe beam was tuned to the IRAV modes, around 7 and 9 μm.

Figure 2.6 shows their PIA results, on a time scale roughly equivalent to that seen at the top of Figure 2.14, from Graupner's work. It may be seen that photogeneration of charged carriers is very fast ($<$ 100 fs). It was also found that the quantum efficiency was as much as 10 %, and independent of the photon energy of the pump pulse. Molecular exciton models, however, predict an increased efficiency at higher photon energies. Moses describes an "absence of correlation" between the $<$ 100 fs generation of charge carriers and the approximately 300 ps lifetime of excitons.[3]

Moses *et al* concludes that their results are all inconsistent with the Onsager model, but rather agree with a model in which charged (free) carriers are the primary photoexcitation.

[2]Raman vibrational modes are those which give rise to scattered light of frequencies $v - v_R$, where v is the frequency of the incident light and v_R is the frequency of the Raman-active mode

[3]Note here the difference in the photoresponse rise-times which can be read off the plot in Figure 2.6, from those seen in the plot at the top of Figure 2.14

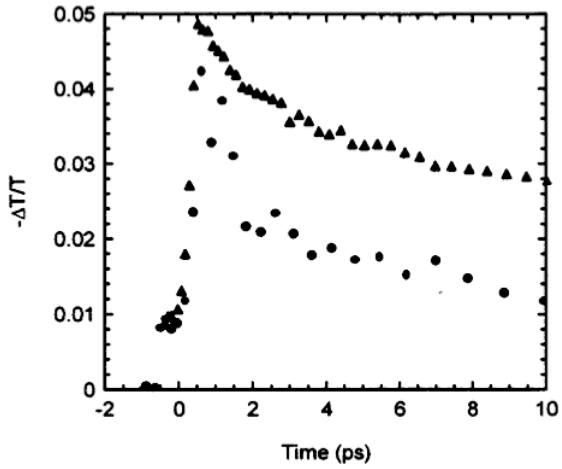

Figure 2.6. Comparison of the PIA wave form in MEH-PPV (solid circles) and MEH-PPV/C_{60} (50 % C_{60} by weight) (solid triangles), when pumped at the same light intensity at 800 nm and probed at 7 μm. From D. Moses *et al*, [42]

2.3.6 2006: Tetracene

In 2006, Moses and associates, in work with single-crystal tetracene, invoked again what might be called the two-mechanism model for carrier dynamics in transient photoresponses: a short-time-scale mechanism with coherent transport of carriers occupying extended states, and a longer-time-scale mechanism with carriers moving via hopping, with trapping and de-trapping from localized states. They found that the peak transient photocurrent varied inversely with temperature, PC $\sim T^{-2.09}$. Citing evidence from the literature that the mobility in tetracene varies in essentially the same manner, they concluded that the photogeneration efficiency must be temperature independent. This behavior of the mobility is essentially the same as that cited by Silinsh (see below), but Moses *et al* interpret it much differently. Where Silinsh explains this temperature dependence in the context of the nearly-small polaron, stepping-via-tunneling model, Moses concludes that it indicates "the existence of a coherent transport" regime.

A superlinear dependence of peak photocurrent on E-field was found, PC $\sim E^{1.6}$. Moses was unable to account for this behavior, but suggested that, if it was due to

exciton dissociation due to an applied field, the binding energy implied is much smaller than that which one would expect for localized excitonic excitations, and more like that found in systems which may be described by a band model.

2.4 The nearly-small molecular polaron model

As a result of work in the late 1980s and early 1990s with organic crystals, Silinsh and Capek[11] proposed the model of the charge carrier in organic crystals as a special sort of quasiparticle, the nearly-small molecular polaron. A nearly-small molecular polaron is "formed as the result of interaction of a charge carrier with intermolecular vibrations of the molecule on which it is localized during the residence (localization) time τ_h, and also due to interaction with polar IR-active vibrational modes of the nearest neighbor molecules."[4]. A "nearly small" polaron interacts with vibrational modes of nearest neighbors, whereas a "small" polaron involves small displacements of the neighboring lattice due to interactions with the dipole moments of its neighbors. The transport model proposed by Silinsh for this type of quasiparticle is "stepping via tunneling," or "stepwise tunneling." The main difference between stepwise tunneling and the sort of hopping described in the previous paragraph is that stepwise tunneling is not dependent upon thermal activation. (This transport model is often also referred to as "hopping via tunneling," but Martin Pope has proposed that the name "stepping via tunnelling" or "stepwise tunneling" be substituted, since "hopping" typically suggests a process requiring thermal activation). A feature of the nearly-small molecular polaron model which is of particular relevance to this paper is that it predicts an inverse dependence of mobility on temperature in pentacene (and presumably in other similar molecular crystals).[11] This inverse dependence arises, in Silinsh's account, from an inverse dependence of the carrier's effective mass on temperature.

Silinsh developed a simulation based on the Fokker-Planck equation for drift and diffusion. The model assumes no specific transport mechanism or carrier type. The model had just two adjustable parameters: the effective mass of the carrier, and the

[4]Silinsh and Capek, *Organic Molecular Crystals*, p. 127

relaxation or thermalization time, which was the characteristic interval in which the particle's "memory" of its initial (photoexcited) radial velocity is lost. The effective mass was assigned an *ad hoc* inverse relation with temperature, in order to get good simulation/data fit. At low temperatures, the relation is exponential; at higher temperatures, a better fit to data is obtained with a power law dependence.

The model survives several experimental tests. First, one may extract from it values for thermalization radius r_{th} versus initial kinetic energy or, equivalently, versus energy ($h\nu$) of incident radiation. At T = 204 K, the model gives, for $h\nu$ = 2.4 eV (close to 530nm), r_{th} = 4.7nm (about 6 lattice constants). For $h\nu$ = 2.7 eV (about 457 nm), r_{th} = 8.0 nm (about 10 lattice constants). Recall that the lattice constant in these crystals is $\sim$ 0.8 nm. Experimental data r_{th} versus for $h\nu$ was found to be in satisfactory agreement with these values: r_{th} = 4.0 at $h\nu$ = 2.4 eV; r_{th} = 7.9 at $h\nu$ = 2.7 eV.

Next, using data for the dissociation probability of e–h pairs versus $h\nu$ and E–field, the model parameters were adjusted for good fit between simulation and data: effective mass = 1550 m_e, thermalization time τ_{th} = 1.1 ps, adiabatic energy gap E_G^{Ad} = 2.43 eV. These values for the adjustable parameters were found to agree well with values in the literature. The results of the simulation for dissociation probabilities were found to be in good agreement with experimental photogeneration quantum efficiency data.

From the model, Silinsh derived the following relation between mobility and temperature:

$$\mu_0(T) = \frac{\sqrt{3}el_0}{[m_{eff}(T)kT]^{1/2}} \tag{2.4}$$

The result: $\mu_0 \sim T^{-n}$, with n = 2.1. This agrees with experimental determinations of $\mu_0(T)$ in *a*-*b* plane in Ac-type crystals. Finally, the model's predictions for electron drift under E-field during thermalization agree with experimental data.

The particular molecular polaron model which Silinsh chose was one which made sense of the simulation results, in particular the predicted relation between mobility and temperature. This was the "nearly small molecular polaron" model, with transport via stepwise tunneling.

2.5 The development of a modified Onsager model

2.5.1 1991: DC and Transient photoconductivity in PPV

In work with PPV in the early 1990s,[35] Bässler and his associates found that DC photocurrent varied directly with intensity. The Stokes shift found was an order of magnitude less than "previously assumed." The action spectra of photoconductivity in PPV correlated with absorption spectra, with a peak at 2.5 eV, construed to be the bandgap. Hence, the dominant optical transition led to production of charge carriers, "in **apparent** agreement" with the band model (emphasis added). On the other hand, inquiry into the quantum yield for DC photocurrent ϕ found that it varies directly but not linearly with E. It was found that the plot can be fitted to Onsager dissociation yield curve for 1D topology (Fig. 2.7).

2.5.2 1994: Quenching & Excitons

Kersting, Bässler *et al* in the mid-1990s did work with a PPV/polycarbonate blend (Blend: 20 % PPV, 80% polycarbonate (PC)), looking at the relation between photoluminescence quenching and exciton dynamics.[36] They employed a sandwich geometry, with an E-field strength of 2 MV/cm. They observed that when the field was applied, quenching did not follow instantaneously, but evolved on ps time-scale; they concluded *therefore* that quenching is governed by a dynamic process of field-induced exciton dissociation (Fig. 2.8). (The response of Moses *et al* response is mentioned briefly in Section 2.3.4).

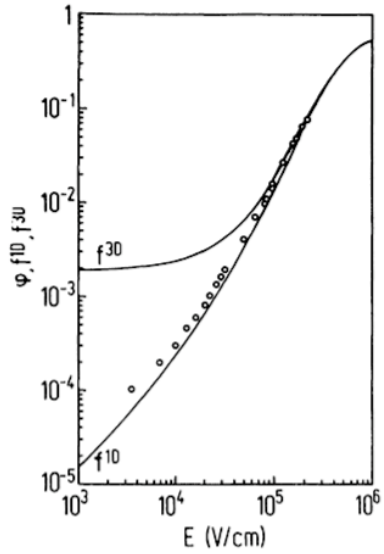

Figure 2.7. Data points represent the quantum yield ϕ of the dc photocurrent as a function of electric field (λ_{exc} = 400 nm, T = 295K). Solid curves are Onsager dissociation yields calculated for an initial pair separation of 25Å, assuming 3D (upper) and 1D (lower) topology, respectively. (From Gailberger and Bässler, PRB **44** 8643, (1991))

This was modeled in terms of the effect of the E-field on the energy difference between the on-chain and near-chain densities of states (Figure 2.9). The increased overlap between on-chain and near-chain DOS with applied E-field meant that electrons were more likely to be lost to nearby-chain-states, quenching photoluminescence.

2.5.3 1997: PPV: Geminate Pair Dissociation

In work in 1997 Bässler *et al* investigated DC photoconductivity in PPV derivatives, again using a sandwich geometry: one electrode indium tin oxide (ITO), the other aluminum.[38]

At the outset, they acknowledge that absorption edge and the photo–conductivity edge in such materials have been observed to be the same, but argue that this is an interface effect rather than a signature of generation of free carriers. Excitons generated by photons at the energy of the exciton absorption edge diffuse to the organic-electrode

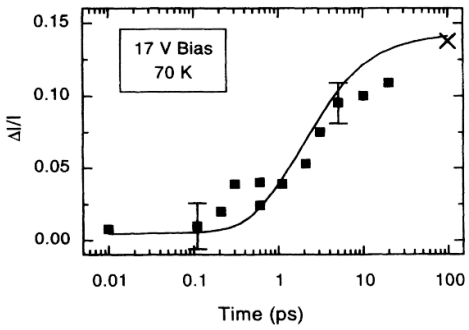

Figure 2.8. Transient luminescence quenching at 70 K as detected with luminescence upconversion (squares). The data are extracted from the time-resolved luminescence signals taken without bias and with an applied voltage of 17 V. The cross indicates the value obtained in CW measurements. (From Kersting *et al*, PRL **73** 1440 (1994)).

interface can dissociate there, one charge going to an acceptor level inside the electrode metal, the other becoming a free carrier.

As a means, therefore, of separating intrinsic from extrinsic sources of electro–optical carrier generation, a 8–10 nm–thick SiO layer was deposited on some of the ITO electrodes, to block photoinjection of charge carriers. With the ITO layer positively biased, this charge–injection block reduced photocurrents by three orders of magnitude.

In this work, Bässler and his associtates refined the model of photoresponse in terms of geminate pair dissociation.[39] The model invoked in this work views the primary excitation as a Franck-Condon state, that is, an excited state in which the nuclei of the material have not yet shifted from their positions in the unexcited state to establish Coulomb equilibrium with the disposition of the electrons in the excited state. Such a state has a certain probability for dissociation onto adjacent chain segments. This dissociation must proceed against the Coulomb potential, and is therefore endothermic. If an excitation has excess energy, it may form a geminate e–h pair, which may either recombine to form a potentially fluorescent S_1 state, or dissociate in a manner for which the Onsager is the appropriate model. The principal result of this work was the claim that "field dependence curves fit perfectly into the family of yield curves

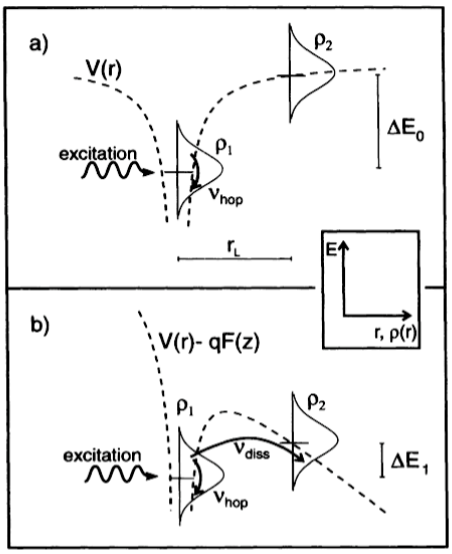

Figure 2.9. Scheme of the relaxation and dissociation processes involved without bias (a) and with applied field (b). ρ_1 denotes the density of states of the excitons. ρ_2 is the density of states if one of the carriers is transferred to a neighboring site. The arrows indicate the relaxation paths. ΔE_0 (with field) and ΔE_1 (without field) indicate the energy differences between an exciton and a geminate e–h pair with a charge separation r_L. (From Kersting *et al*, PRL **73** 1440 (1994)).

calculated by Pai and Enck, under the premise of Onsager type geminate dissociation in 3 dimensions"[52] (Figures. 2.11, 2.12). This claim was modified in future work (see next section). Questions regarding the time-scales on which the processes incorporated into this model take place, and the critical question regarding the evident contradiction between the quantum yield temperature dependence implied by the Onsager model and that observed experimentally were not addressed in this work, but were addressed later (see below).

This group also presented a further explanation of the coincidence of the onset of photoconductivity and the optical absorption edge, in terms of intrinsic properties of PPV rather than interface effects, as follows:

> "While in organic crystals an energy gap usually exists between the excitonic absorption edge and onset of intrinsic photoconductivity, this gap narrows and may even approach zero in random media

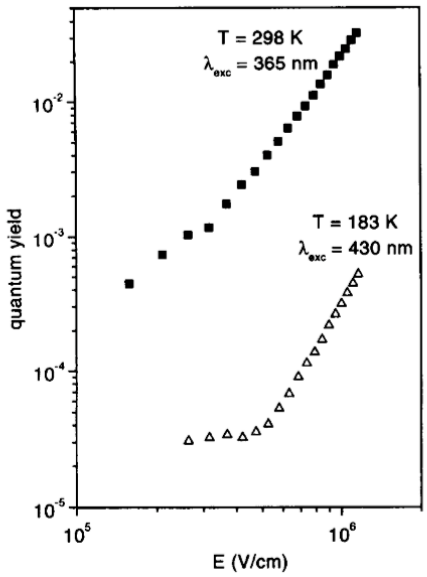

Figure 2.10. Field dependence of the intrinsic photocurrent in a 95 nm thick PPV–ether film. The photocurrent was measured upon irradiating through the ITO/SiO electrode at positive bias. (From Barth *et al*, Chemical Physics Letters **274** 165 (1997).)

> because the expense in Coulombic energy may be compensated for by an increase in site energy, albeit with low probability."

2.5.4 1999–2000: Dissociation of hot excitons; extended states

In 1999–2000, working again with PPV derivatives, Bässler and his associates looked more closely at what happens on very short time scales immediately following an optical excitation.[37] In particular, they examined the temperature–dependence, or lack thereof, of the photoresponse of conjugated polymers, both strongly and weakly disordered. They concluded that a weak temperature dependence arises from the initial excatation taking the form of on–chain extended states, which renders the diffusive dissociation characteristic of the Onsager model inappropriate for description of these processes. The model developed was "based on the assumption that carriers are delocalized within a conjugated segment, preventing diffusive intrasegmental motion of carriers."

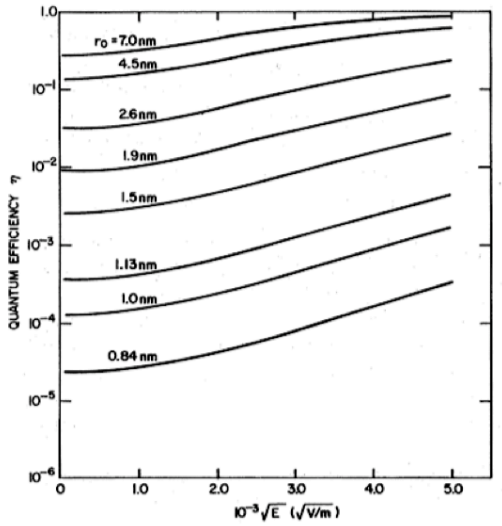

Figure 2.11. Onsager dissociation efficiency vs. square root of the applied electric field for several separations. (From Pai and Enck (PRB **11** (1975) 5163)

In this model, an optical excitation into the vibronic manifold at t = 0 yields a Franck-Condon state, which immediately begins to relax. The probability for dissociation of the exciton is a function of the effective temperature, $T_{eff}(t) = T + T_0\Theta(t)$, where T is the ambient temperature, T_0 is the temperature jump at the site of the excitation at t = 0, and "$\Theta(t)$ describes dissipation of the vibronic energy into the equilibrium phonon bath." $\Theta(t)$ is probably proportional to $exp(-t/\tau)$, where τ is a very short dissipation time constant.

> "On a time scale of less than 100 fs the structural skeleton of that part of the chain, where the excitation was initially localized, relaxes into an equilibrium configuration characteristic of the first singlet state, and the excess energy, $E_{exc} = h\nu - E(S_1)$ will be distributed among the vibrational modes due to vibronic coupling."

The hot exciton thus generated very quickly "cools" to the ambient temperature. If it cools too quickly for vibrational coupling to the ambient phonon bath, then the effective temperature governing dissociation probability is only that of the temperature jump at excitation, not summed with the ambient temperature. If this is the case, then the quantum yield becomes independent of the ambient temperature.

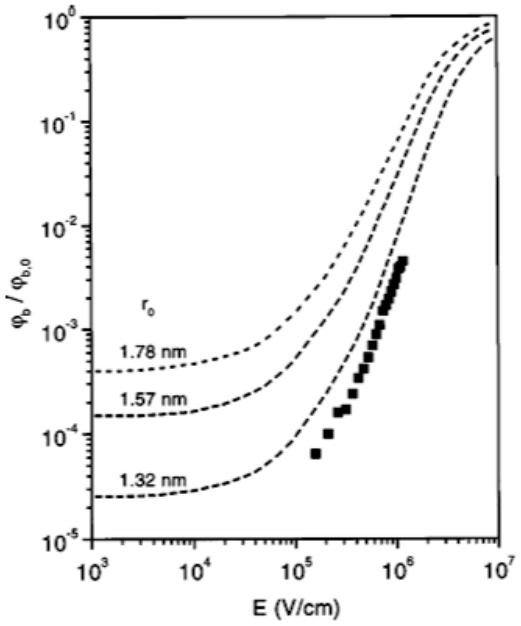

Figure 2.12. Comparison between the experimental field dependence of the intrinsic photocarrier yield in undiluted PPV-ether, and theoretical 3D Onsager fits for $\epsilon = 4$ and variable thermalization distance r_0. (From Barth *et al* PRB **56** (1997) 3844)

Experimental values for the photogeneration efficiency were plotted against curves derived from their mathematical model, and found to be quite close. One of the parameters used for curve fitting was the exciton binding energy, which took the value of 0.46 eV, very close to what is presently the consensus value of 0.4 eV.

The assumption in this model that "carriers are delocalized within a conjugated segment" is strikingly similar to what Moses, Sinclair and Heeger said in 1987, that "the broad π bands of conjugated polymers tend towards extensive delocalization." Delocalized states are important to this model, and in this respect it bears some resemblance to the models proposed by Daniel Moses and his group, but it is important to note that at no time do Bässler *et al* invoke the concept of *bands*. Probably the key difference between the two models is with respect to the question of exciton binding energies. Moses and his group believe that these binding energies are of the order of k_BT, i.e.,

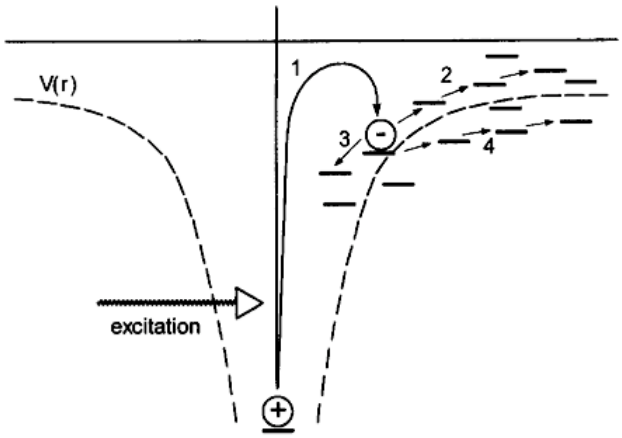

Figure 2.13. Schematic view of geminate pair dissociation in an energetically random hopping system. At high temperatures a carrier generated optically (process 1) at a certain thermalization distance r_0 can either dissociate via thermally activated jumps involving states close to the center of the manifold of hopping states (route 2) or recombine (route 3). At low temperatures escape proceeds via the tail states of the DOS (route 4). This route requires less thermal energy. (From Barth, Bässler, *et al*, CPL **274** (1997) 165-170)

$\sim$ 25 meV. Bässler's group adopts what is essentially the consensus view at present, that they are in the neighborhood of 0.4 eV.

2.6 Results of other recent work

Here are briefly summarized the results of recent work done by some other important groups in this field.

2.6.1 Graupner Group

W. Graupner and associates worked with methyl-substituted ladder-type poly(*para*-phenylene) (*m*-LPPP).[34] In their study, organic LED devices (OLEDs) made from thin films of m-LPPP were excited with 390 nm (3.18 eV) pump pulses. A super-continuum probe pulse selected at 649 nm (1.91 eV) was used to monitor polaron density in the sample. A second probe pulse selected from the super-continuum at 490 nm was able to

induce stimulated emission from singlet excitons generated by the pump pulse. An electric field across the sample was modulated so that the exciton population was quenched (thus reducing exciton stimulated emissions) while at the same time increasing the polaron density. In Figure 2.14, the bold lines represent the polaron population and the finer lines the exciton population. it may be seen that the polaron population has an approximately 10 ps rise-time, and that the exciton(-quenching) population peaks, 1 to 2 ps after the pump pulse. Graupner's conclusion, from inspection of the time difference between the two peaks, was that field-induced exciton-breaking led directly to polaron formation, over a 10 ps time-scale, with no signature of intermediate states. That is to say, free charge carriers were not the primary photoexcitation.

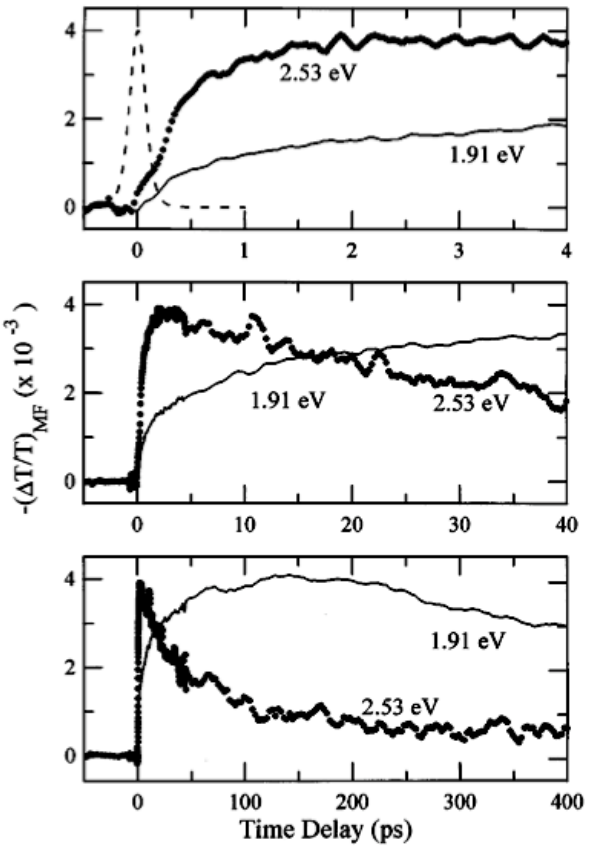

Figure 2.14. Field–induced differential transmission $(-\Delta T/T)_{MF}$ at 1.91 (solid line) and 2.53 eV (dots) as a function of pump-probe delay. Upper panel (dashed line) pump pulse autocorrelation). From W. Graupner, *et al* [34]

2.6.2 Hegmann, Ostroverkhova Groups

F. Hegmann and O. Ostroverkhova, and their associates, have both worked with organic materials, sometimes in collaboration. The organic materials under investigation by these groups have primarily been polyacenes rather than polymers.

Hegmann used optical-pump THz-probe methods on functionalized pentacene derivatives, in which side groups of triisopropylsylilethynil side groups are added to the pentacene backbone (TIPS-pentacene).[32] The rise times observed were sub-picosecond, limited by the resolution of the pump-probe setup – probably much shorter. The differential transmission $- \triangle T/T_0$ (see Chapter 1, Section 1.4.2), plotted on a log-log scale in the lower graph of figure 2.15, shows two different power-law decay rates for the 1 - 3 ps and the 3 - 40 ps time-scales.

It was found that the magnitude of the $- \triangle T/T_0$ signals was independent of the amplitude of the THz probe signals. Hence THz-field-induced breakup of excitons could be eliminated as a possible carrier generation mechanism. The sub–ps rise–time agrees well with times for polaron formation reported by others,[42,53] but not as well with data for field-assisted exciton dissociation.[34] Hegmann suggested that the fast initial rise-time corresponds to band-like carrier photoexcitation, in which carriers then couple to the lattice to form polarons. The power-law decay observed for time-scales longer than 4 ps is attributed to dispersive transport.

Hegmann notes[32] that this form of behavior fits with the nearly-small polaron model, proposed by Silinsh *et al*,[11] in which bandlike transport is described via non-thermally-activated tunneling.

O. Ostroverkhova has worked with functionalized pentacene (FPc) single crystals and FPc and Pc (pure pentacene) thin films, on glass and mica.[29,40] The same sort of differential transmission behaviors of these materials was observed as by Hegmann, as may be seen in Figure 2.16. A significant increase in carrier mobility with decreasing temperature was observed, a signature of bandlike transport. The overall power-law profiles observed agree with those of Hegmann, and with the nearly-small polaron model,

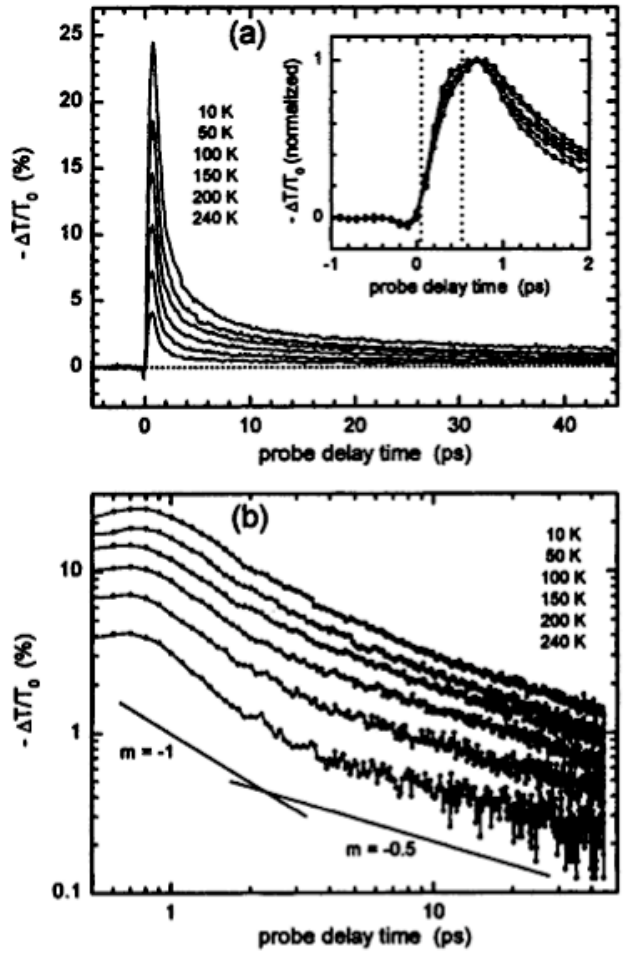

Figure 2.15. (a) Percent differential transmission of the peak of the THz probe pulse as a function of delay time and temperature. (b) Log-log plot of data shown in (a). Lines labeled m = -1 and m = -0.5 are guides to the eye for power law decay rates of t^{-1} and $t^{-0.5}$, respectively. From F. Hegmann.[54]

in which the slow power-law decay is due to dispersive charge transport through multi-step tunneling.

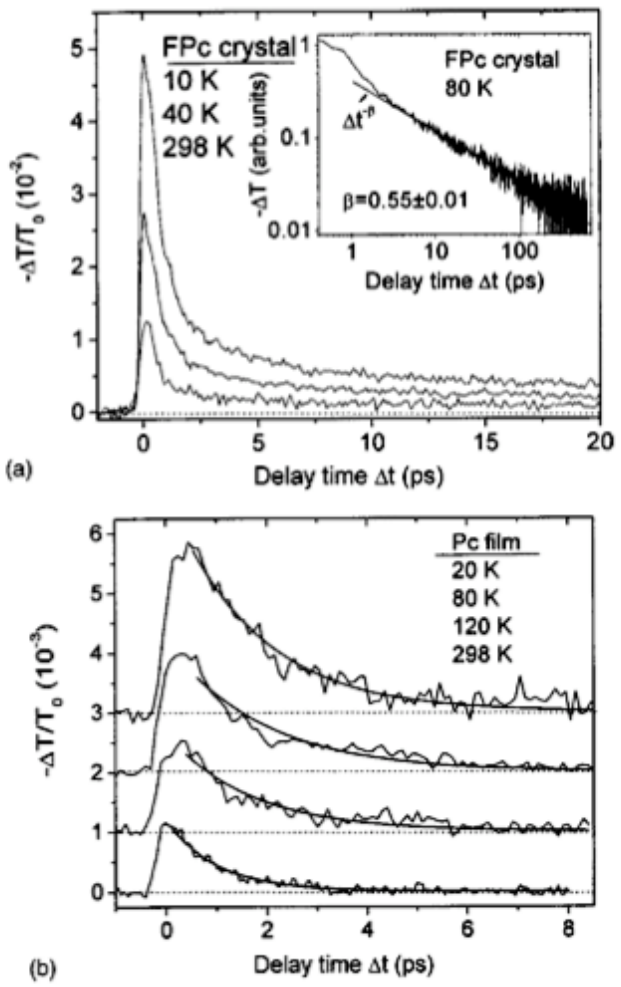

Figure 2.16. Differential transmission of the peak of the THz probe pulse as a function of delay time and temperature. (a) FPc crystal under optical excitation at 400 nm with $F \sim 0.4$ cm^2 at temperatures of 298, 40, and 10 K. The inset shows a power-law fit $\Delta t^{-\beta}$ ($\beta = 0.55$) to the data obtained at 80 K for Δt ¿ 2 ps. (b) Pc thin film under optical excitation at 580 nm with $F \sim 1$ mJ/cm^2 at temperatures of 298, 120, 80, and 20 K. Single-exponential fits to the data are also shown. From O. Ostroverkhova.[29]

2.7 Summary

This discussion of a very small portion of the literature relevant to this thesis, incomplete as it is, shows that many questions regarding the electronic behavior of organic semiconductors are yet unanswered.

It will not have escaped the reader's notice that the debate chronicled above has centered largely, though not exclusively, on questions of carrier generation and transport in conjugated polymers, rather than organic crystals – which are, after all, the subject of this thesis. There are two main reasons for this. First, most of the discussion of the controversies centered on these materials over the last two decades has been in the context of research into the polymers. This is largely due to the fact that the development of synthesis, processing and purification capabilities for organic crystals, to the point where they have become commercially viable electronic materials, is a relatively recent development. Many of these materials are still being synthesized for the first time. Second, in spite of their differences, conjugated polymers and organic crystals are alike enough, in several important respects, for many of the advances in theory and methodology which have been made in the area of research into polymers to be very relevant to their crystalline cousins. For example, where bandwidth calculations have been made, the bands have typically been found to be very narrow. Hence, the energy structures of both types of materials have come to be generally analyzed with reference to HOMO and LUMO levels, rather than "conduction" and "valence" "bands.". Again, both types of materials have π and π^* orbitals, in one case along a conjugated segment, in the other case along the polyacene backbone, orbitals which some believe may support the existence of extended states. Excitons in both materials are Frenkel rather than Wannier excitons.

The primary difference between conjugated polymers and organic crystals is, of course, that crystals are *ordered* materials. This means, for example, that a conjugated polymer may be made to be anisotropic in conductivity or mobility by the way in which it is fabricated, but an organic crystal is intrinsically anisotropic. The ordering of the crystal means that overlap integrals between π orbitals tend to be much greater along certain axes of crystal symmetry than along others. When Moses interprets the temperature dependence of the peak photocurrent in tetracene crystals in terms of coherent transport,[92] surely this analysis bases some of its appeal on the ordered, crystalline character of the material in question.

On the other hand, it should be noted that when the term "bandlike" was used in the context of some of the work discussed in earlier sections, this should not necessarily be taken to mean that a real band model is being invoked. For example, the power-law temperature-dependence of mobility in Silinsh' discussion arises as a consequence of the nearly-small polaron, stepping-via-tunneling model. This dependence is band-"like", but Silinsh is very much in the camp of those who deny the applicability of band models to organic crystals and polymers. However, when Moses uses the term "interband",[92] it seems plain that he is using the term "band" very much in its conventional sense.

The consensus in the literature at this time seems to weigh against the views of Daniel Moses and his associates. That is, it is generally thought that something like Silinsh's view is correct, that the wave number **k** for charge carriers in these materials, at least at room temperatures, cannot be a good quantum number, even on the shortest time-scales, as it must be for the band-model to be applicable. Hence, when data, such as that for the dependence of parameters such as quantum efficiency or mobility on temperature, is not in agreement with the Onsager model, this must be accounted for in some other way. As discussed above, Bässler and his associates have recently put forth models, essentially modified Onsager models, which actually bear some relation to those of Moses *et al*, at least with respect to the nature of the initial excitation. That is to say, they see the initial excited state as "delocalized," as an on-chain extended state, which gives rise to a weak dependence of the initial photorespose (Section 2.5.4) on temperature. But the delocalization they envision is not the same as that associated with a "band," inasmuch as it is restricted to a polymer chain, and is therefore presumably not the sort of state for which one can define a Bloch function. On the other hand, while their model can account for weak or non-dependence of mobility on temperature, it cannot account for evidence that the dependence may be negative.[8,32]

Transport on longer time-scales is perhaps more relevant to practical questions of device design. Here the picture is also uncertain. The question is, what is the nature of the majority carrier, and how does that nature evolve after an initial excitation? To what degree is the initial state localized or delocalized, and how and to what extent does

it become localized as time passes, and the transport mode relaxes towards steady-state? Models for these processes are still in flux. For example, the model proposed by Silinsh discussed above (Section 2.4) in which the carrier in steady-state transport is a "nearly small molecular polaron" has survived well. But the carrier in this model is regarded as "dressed," which means that the effective mass of a carrier may by much greater than the mass of an electron, perhaps two orders of magnitude greater. But recent work[60] has provided evidence that under certain conditions, in this case in organic FETs subject to high gate voltages, the majority carrier may be a light "quasiparticle" with an effective mass close to m_e – apparently not "dressed" at all.

Our research supports the following position with respect to carrier generation and transport in functionalized oligoacenes and anthradithiophene: that carrier photogeneration is assisted weakly, if at all, thermally or by applied fields, that carriers are initially in extended states and transport is "bandlike" (picoseconds to nanoseconds), relaxing then into more localized states, transported via thermally assisted hopping (nanoseconds to seconds). We observe the sort of negative dependence of photocurrent amplitude on temperature, on very short time-scales, which is not accounted for by Bässler's modified Onsager model, suggesting behavior rather more akin to the traditional notions of "bandlike." This will be discussed further in the chapters which follow.

On the Photoresponse of Several Novel Functionalized Oligoacene
and Anthradithiophene Derivatives

CHAPTER 3
TRANSIENT AND CW PHOTORESPONSE: 285–350 K

3.1 Introduction

Organic semiconductors have attracted attention due to the possibilities they offer for organic thin-film transistors (TFTs), light-emitting diodes (LEDs), photovoltaic cells, organic lasers, photorefractive (PR) devices, and many other applications.[1,3] Recently, considerable progress has been made in materials design and device performance:[2,3,55–58] charge carrier mobilities of over 20 $cm^2/(Vs)$ have been reported in rubrene and pentacene single crystals,[59,61] power conversion efficiencies over 6% have been observed in solution-processed polymeric solar cells,[62] and PR two-beam-coupling net gain coefficients in organic glasses and polymer composites approached 400 cm^{-1}.[3] However, understanding of the physics of charge carrier generation and transport in organic semiconductors, which determine electronic and opto-electronic characteristics of these devices, is lacking, and basic questions regarding the nature of these processes remain open.[4,6,6–10,63–66,92]

One approach to the investigation of these questions, as described in Chapter 1, is to examine the response to light of a photo-active material, especially on very short time scales. This is potentially extremely revealing of both its physical and its electronic and energy structure. The energy structures of organic crystals differ from those of inorganic crystals, as mentioned above, in fundamental ways. Bandwidths have been determined using a variety of methods, from early work by Leblanc using the tight-binding approximation[46] to more recent work using Density Functional Theory (DFT).[67] The values obtained by these different methods for bandwidths in pure polyacences

(anthracene, pentacene) have ranged from the very small values obtained initially by Leblanc (∼0.015 eV), to recent values obtained using DFT, yielding bandwidths for HOMO and LUMO levels in pentacene thin films of ∼0.7 eV and ∼0.8 eV, respectively. Bandgaps in pure pentacene were calculated by Silinsh to be 2.83 eV for the optical energy gap and 2.47 eV for the adiabatic energy gap.[11] Comparable values for the bandwidth of silicon are more than an order of magnitude higher, although the bandgap is of the same order of magnitude (1.5 - 2.0 eV). Such narrow bandwidths are in keeping with the relatively low measured mobilities of pure and functionalized pentacenes.

Such work has been done primarily with pure forms of the oligoacenes. Preliminary results for certain of the functionalized pentacenes, in contrast, show stronger photoresponse than the pure form, suggesting perhaps wider bandwidths. These materials have proven also to be solution-processable, enabling thin films to be fabricated by simple drop-casting from solution onto a suitable substrate. This ease in processing makes these materials attractive subjects for investigation of photoresponse. Such response can be viewed in either the time or in the frequency domain. Viewing the response in the time-domain allows one to record a "movie," so to speak, of the photoresponse, allowing, in principle, the testing of predictions of trapping and detrapping rates, relaxation times and the like. This, in turn, allows deductions from one's model of the material's energy structure, photoexcitation processes, and transport mechanisms, to be tested. This chapter is devoted to discussion of results obtained, using the time-domain approach, with two important varieties of functionalized acene.

One of the challenges encountered when probing electronic and opto-electronic properties of organic materials is that different charge generation, transport and trapping mechanisms may dominate the performance under different experimental conditions. As a result, different experimental techniques can produce results that are difficult to compare and, often, hard to reconcile. For example, methods probing charge carrier dynamics on short (sub-nanosecond) time scales after photoexcitation (such as ultrafast time-resolved terahertz (THz) pulse spectroscopy,[7–10,68] infrared active vibrational (IRAV) spectroscopy,[69,70] and Auston switch-based ultrafast photocurrent

measurements,[50,71,92]) often yield results different from those obtained using field-effect transistor (FET),[59] space-charge-limiting current (SCLC),[61] or continuous wave (CW) photoconductivity[72,73] measurements, in similar materials. To reconcile these differences in each particular case and develop understanding of all mechanisms involved, it is important to use a combination of several experimental techniques, for example those that probe charge carrier dynamics on various time scales, in the same samples. An example of such combination is measurements of time-resolved and CW photoconductivity, which have been previously applied in studies of photoconductive polymers,[74] organic single crystals,[75,92]and thin films,[76]and which we used in our studies.

As mentioned above, of particular technological interest are low-cost, solution processable, high-purity materials that can be cast into high-performance conductive and photoconductive thin films. This motivated the selection for our studies of several novel small-molecular-weight photoconductive materials that form thin films with good coverage by solution deposition. These are functionalized anthradithiophene (ADT), functionalized pentacene (Pc), and dicyanomethylenedihydrofuran (DCDHF) derivatives. Functionalized ADT and Pc polycrystalline films have been previously explored in thin-film-transistor (TFT) applications,[2] and TFT mobilities of over 1 $cm^2/(Vs)$ have been recently reported in solution-deposited functionalized Pc thin films.[2,24] DCDHF derivatives are glass-forming molecules originally developed for PR applications, and DCDHF-based monolithic amorphous glasses are among the best-performing organic photorefractives.[3,25,26] In addition, a number of functionalized ADT and DCDHF derivatives are highly fluorescent,[77–79] which broadens the range of their possible applications. For example, DCDHF derivatives have been utilized as fluorophores in single-molecule spectroscopy.[78,79]

Presented in this chapter are the results of a study of photoexcited charge carrier dynamics, on time scales from several tens of picoseconds to many seconds after excitation, in functionalized anthradithiophene, functionalized pentacene and DCDHF thin films, together with semi-insulating GaAs as a benchmark. Using time-resolved photocurrent measurements, we observe fast charge carrier photogeneration, and charge

carrier mobility decreasing as the temperature increases, on picosecond time scales after photoexcitation, in all samples. Observed variations in decay dynamics and in equilibrium photoconductivity among these materials are correlated with differences in charge trapping and recombination properties. Measurements of time-resolved and CW photoconductivity in the same samples, as a function of various parameters, allow us to observe charge carrier localization process that depends on the material.

3.1.1 Traps

In view of the fact that in much of the discussion in this chapter, results are interpreted in terms of carrier traps and trapping in organic materials, a brief account of such matters is appropriate.

A carrier trap in a semiconductor is any location in the material which has a significantly higher affinity for the type of carrier in question than the bulk material. Carriers in a given semiconductors are usually both electrons and holes, but other than in a completely "pure" intrinsic semiconductor, it is likely to be the case that one or the other is the dominant or majority carrier. Inorganic semiconductors in which the majority carrier are electrons are "n-type," those in which the majority carrier are holes are "p-type." These terms are used less in the literature on organic semiconductors, but the basic fact remains that a given material may be primarily a hole transporter or an electron transporter. A given real organic material will certainly have traps for its majority carriers, but will very likely also have traps for the minority carrier. Traps for the majority carrier will of course have an effect, perhaps a great effect, on the material's electronic behavior, but traps for the minority carrier may also play an important role.

Traps arise from a variety of causes. In our materials, perhaps the largest population of trapping sites is that found at the walls between the domains of the poly-crystal. Defects and impurities within the crystal in a particular domain are undoubtedly present. But experiments with doping described in Chapter 5 show that other kinds of traps also play a non-negligible role. These sorts of traps are understood in terms of the energy structure of an organic semiconductor. In close analogy

to inorganic semiconductor band theory, such traps often (but not always) reside somewhere in the "band gap"; that is to say, somewhere between the HOMO and LUMO levels. The "depth" of a trap is determined by its energetic distance from the level in which the carriers which it may trap are generally transported. "Shallow" traps are energetically near to the relevant level, "deep" traps are distant. One of the important parameters in discussions of the behavior of carriers in the time domain is the trapping or the de-trapping rate. The trapping rate is the reciprocal of the mean time a carrier spends between trapping events, the de-trapping rate is the reciprocal of the time the carrier spends in the trap. De-trapping a carrier from a shallow trap is energetically much easier than de-trapping a carrier from a deep trap, and the de-trapping rates differ correspondingly. Shallow traps may be emptied of their trapped carriers on nanosecond time scales, or shorter. Deep traps may take hours to empty, or longer.

Carriers in traps require energy to get out, energy which can be supplied in several ways. At room temperature, especially in the case of a shallow trap, simple vibrations of the lattice are often sufficient. An applied field or an incident photon also may serve to assist de-trapping.

Finally, of great importance in the role played by traps in the overall electronic behavior of the material is their density. Two otherwise very similar films may vary greatly with respect to trap density, either unintentionally, as a result of variations in film morphology resulting from unintentional variations in how they were prepared, or intentionally, as a result of how they are, for example, doped.

3.1.2 Materials Preparation

The principal materials used in this part of this work, ADT-TIPS-F, Pc-TIPS, and DCDHF, have been described in detail in Chapter 1, Section 1.1.2. To recapitulate: ADT-TIPS-F is a fluorinated anthradithiophene derivative functionalized with triisoproplysilylethynyl (TIPS) side-groups,,[2] Pc-TIPS is a pentacene derivative also functionalized with TIPS groups,[2,8,9,24] and DCDHF is a 2,6-naphthalene functionalized with dihexylamino donor and dicyanomethylenedihydrofuran acceptor[3,25,26] (Fig.

3.1). Pc–TIPS and ADT–TIPS–F both exhibit brick-wall-type crystal packing with significant π-overlap,[2,80]favoring high TFT mobility.[24] Both materials form polycrystalline films[9] when deposited from solution, with the a-b plane in the plane of the film. Under similar conditions, DCDHF forms an amorphous glass[25] with a glass transition temperature (T_g) of 32°C.

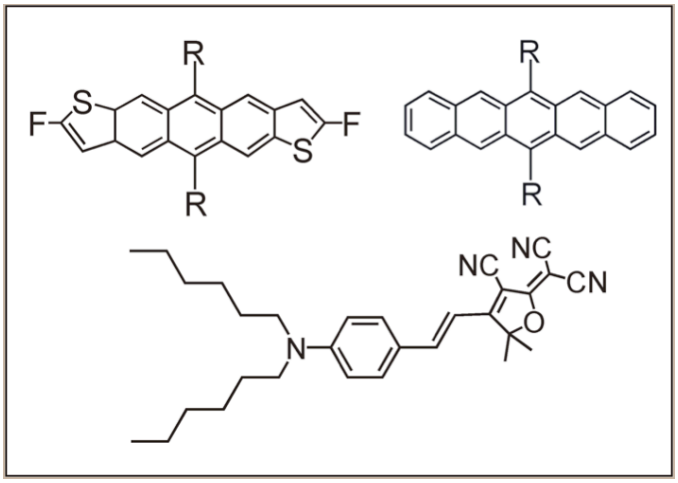

Figure 3.1. Molecular structures. R = Si(i-Pr)$_3$.

Investigations into the photoresponse of organic semiconductors, under the influence of an applied field, may involve non-contact methods (such as THz pump-probe methods), or they may use contact methods, often taking the form of placing the organic material between metal electrodes. Here we describe results obtained using contact methods. The two principal electrode geometries commonly employed are the sandwich geometry and the coplanar geometry. The sandwich geometry typically employs, first, a transparent bottom layer of conductive indium tin oxide (ITO) on a glass substrate, ITO being largely transparent to visible (laser) light, but also conductive. Upon this a layer of the organic material under investigation is deposited, either by spin-coating or by vacuum deposition. The upper layer of the sandwich is usually a vacuum-deposited thin film of the metal chosen for the other electrode, commonly gold, chromium, or aluminum. Optical excitation of the sample is achieved by illumination through the ITO layer. The sandwich geometry has the advantage that very high electric field strengths

may be achieved, since the gap between the two electrodes is only the thickness of the organic film, usually between 100 nm and several μm. The film, however, must be of such thickness and uniform density that metal of the vacuum-deposited upper electrode cannot reach and make conductive contact with the lower electrode.

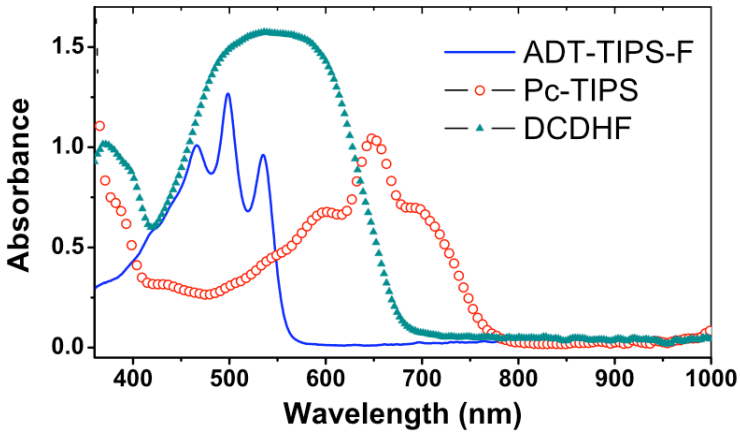

Figure 3.2. Optical absorption spectra of ADT–TIPS–F, Pc–TIPS and DCDHF films.

An effort was made, early in this study, to use the sandwich geometry. Films were deposited in vacuum on glass substrates previously prepared with indium tin oxide (ITO), The upper electrode was an approximately 100-nm-thick layer of gold, also deposited in vacuum. It was found that, perhaps due to the presence of pinholes in the organic film, there was indeed some degree of conduction between the two electrodes, through the film, with resistances between electrodes as low as 185 Ohms. This rendered the samples so prepared unusable for data collection. Rather than pursue this approach, we decided to explore the possibility that the coplanar geometry might be made to work.

A simple coplanar electrode pair, with a straight gap between the electrode, is not a particularly efficient geometry for examination of transient photoresponse to a pulsed laser beam. The diameter of the laser beam typically used for these experiments is of the order of a few millimeters. A gap between the electrodes of that length, and

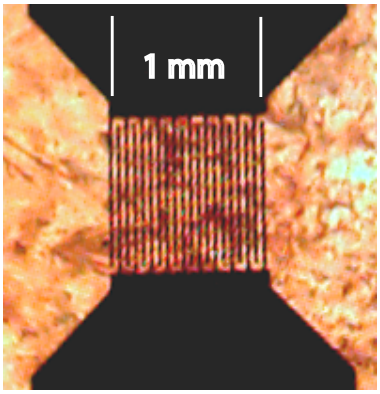

Figure 3.3. Typical interdigitated electrode pair: metal areas black, active area 1 mm, finger width 25μm, interfinger spacing 25μm. Film shown: ADT-TIPS-F

perhaps of 25 or 50 μm width, will enclose a relatively small volume of the organic film. As a result, the quantity of carriers generated by the laser pulse, at the quantum efficiencies typical of organic materials, will be very difficult to measure, even under very high applied electric fields. A much more effective construction of the coplanar geometry is the interdigitated electrode pair, in which each electrode extends several thin "fingers" (digits), with gaps between these digits where the corresponding fingers of the other pair lie. This is the geometry which we used (Figure 3.3). Glass substrates were prepared by photolithographic deposition of 100-nm-thick aluminum (Al) and 55-nm-thick gold (Au) electrode pairs. Each pair consisted of 10 interdigitated finger-pairs, with 1 mm finger length, 25 μm finger width and 25 μm gaps between the fingers of opposite electrodes. The length of the gap in this case is now two centimeters, while the total active area in which the interdigitated fingers are present, is only 1 mm^2. This area may easily be fully illuminated by a typical diode laser beam. The volume of organic material within such a gap is more than an order of magnitude greater than that within a straight coplanar gap of 1 mm length and the same width.

Such a coplanar electrode pair may be deposited on an opaque substrate such as alumina, or it may be deposited on a transparent substrate such as glass. A transparent substrate has the advantage of allowing illumination from the back side of the substrate, opposite to the side on which the organic film is deposited. The metal-organic interface is thus "in the shade," as it were, except at the very edges of the metal film, which means that photoelectric effects and effects from photo-injection at the metal-organic interface can be minimized. This question is discussed in Chapter 5, Section 5.4.6.

There are several techniques for depositing a thin organic film on a coplanar electrode pair so prepared. It was found that, for our purposes, the best method was one of the simplest, that of drop-casting. In this technique, the substrate is heated, in our case to approximately 70 degrees Celsius, in order to accelerate evaporation of the solvent. A solution of the organic molecule and a solvent, here toluene, is prepared. A thin-gauge (32 AWG) wire is prepared by winding one end into a small loop, approximately 1.5 mm in diameter, bent into a plane at right angles to the axis of the straight wire. This loop is cleaned in a toluene cleaning solution and then dipped into the organic/toluene solution. The wire with its loop is withdrawn from the solution, with a bead of the solution suspended within the loop. When this bead is lowered carefully down onto the active (interdigitated) area and makes contact with the substrate on the heater, surface tension wicks it quickly out of the loop and onto the substrate surface. The volume of the bead is small enough that it will not spread far beyond the active area before the heater has evaporated out the solvent, and a polycrystalline film has formed.

In this way, polycrystalline thin films of ADT-TIPS-F and Pc-TIPS[8] and amorphous films of DCDHF[25] (with a glass transition temperature of 32°C), with thicknesses of 0.5–2 μm were drop-cast onto our substrates. Up to ten samples of each kind were studied. Optical absorption spectra of films are shown in Fig. 3.2. A GaAs sample was prepared by deposition of coplanar silver epoxy electrodes of $\sim$3 mm length (with a gap of $\sim$2 mm) on a semi-insulating GaAs wafer (University Wafer, Inc.).

3.1.3 Instrumentation

A schematic of the instrumentation setup for transient photoconductivity measurements is shown in Figure 3.4. An amplified Ti:Sapphire laser (800 nm, 100 fs, 1 kHz) was used in conjunction with a frequency-doubling BBO crystal to excite the samples. In GaAs samples, additional data were obtained with 800-nm pulses. Fluences in the 10-100 μJ/cm^2 range were used to excite organic films, while much lower values were used in measurements of GaAs, to keep the total number density of photogenerated carriers below 10^{16}cm^{-3}. Samples were placed in a fixture configured, as shown in Figure 3.4, so that the sample was essentially the upper resistor in a two-resistor ladder network between the power supply rail and ground, the lower resistor being the load resistor. The junction between the two was at the center-pin of an SMA coaxial connector, to enable signal output via a coaxial cable assembly to measurement instruments. The fixture, in its final version, incorporated a thermoelectric unit for temperature control in the 285–350 K range; both heating and cooling cycles were used. Voltage was supplied by a Keithley 237 source-measure unit, and light pulse-induced transient photocurrent was measured with a 10 kΩ load by a 50-GHz CSA8200 digital sampling oscilloscope (DSO), as voltages across the load resistor developed by the photocurrent through it. The 10 kΩ load resistor served primarily as a path for current through the sample to reach ground; the effective load value for measurements of transient photo-currents was actually the 10 kΩ resistance in parallel with the input impedance of the receiving instrument; that is, close to 50 Ω.

It was clear at an early stage of this study that the photoresponse signals from the organic thin films might be undetectable without some form of amplification. A 30 dB broadband amplifier was purchased from Centellax. The gain of this unit is comparatively flat up to 50 GHz, which means that Fourier components of the photoresponse signal up to very high frequencies may be transmitted with minimal distortion. As it turned out, properly prepared samples often allowed us to obtain data without the use of the amplifier. Comparison of transient wave-forms obtained with and without the amplifier showed that, within the time-resolution imposed by other components of our

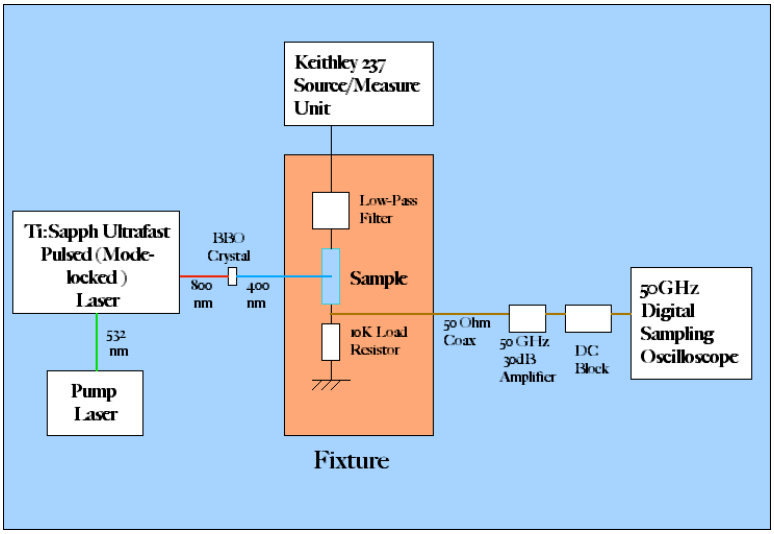

Figure 3.4. Instrumentation and fixture setup for measurements of transient photoresponse.

setup, the amplified signal showed no distortion. Data taken over a range of voltages, i.e., from 10 to 100 Volts, often required that the amplifier be used at low voltages but removed at higher voltages, when the amplitude of amplified signals exceeded the dynamic range of the DSO.

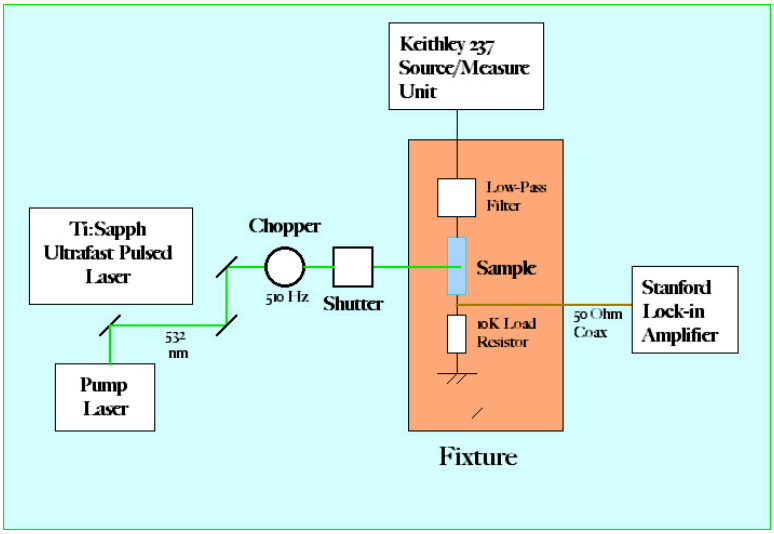

Figure 3.5. Instrumentation and fixture setup for measurements of continuous-wave (CW) photoresponse

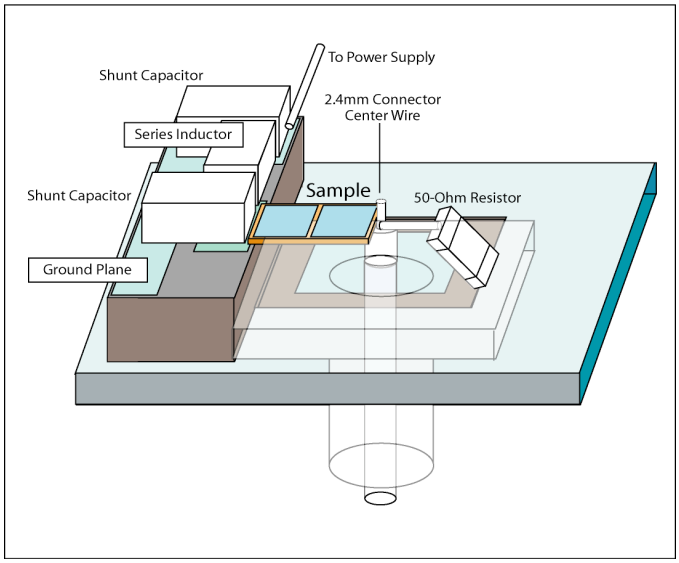

Figure 3.6. Early version of fixture. Shunt capacitor/series inductor network serves as low pass filter, to ensure that potential across sample/load resistor network remains constant.

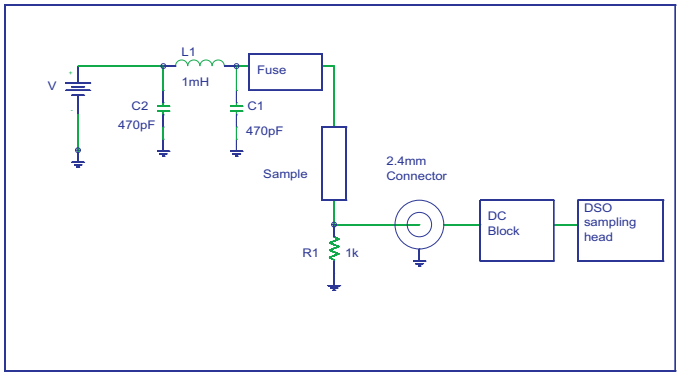

Figure 3.7. Schematic of fixture used in transient photocurrent experiments

In CW photoconductivity measurements, the sample was excited either by a Nd:YVO_4 laser at the wavelength of 532 nm or by a UV lamp and a filter combination with a center wavelength of 365 nm and a bandwidth of ∼40 nm. In one set of experiments, the beam was mechanically chopped at a frequency varied between 20 and 1000 Hz, with the chopper synchronized with the reference input of a SRS830 lock-in amplifier. Photoresponse of the sample was measured as voltage across a 10 kΩ load resistor.

In another set of experiments, the Keithley 237 source-measure unit was used to measure dark and CW photocurrent using the following protocol. The voltage was applied, and the dark current was monitored for 5 seconds. Then, the light beam was opened with a shutter, illuminating the sample, and the current in the presence of light was measured over 10-20 seconds. The CW photocurrent (subsequently referred to as "dc photocurrent" or "photocurrent measured under dc conditions") was calculated as the difference between the two. In all our experiments, the samples were illuminated from the glass substrate side, to minimize photoinjection and photoemission effects.[81,82] The data were taken point-by-point, with the samples kept in the dark between the data points, to avoid accumulation of space charge. The setup for CW measurements is shown in Figure 3.5

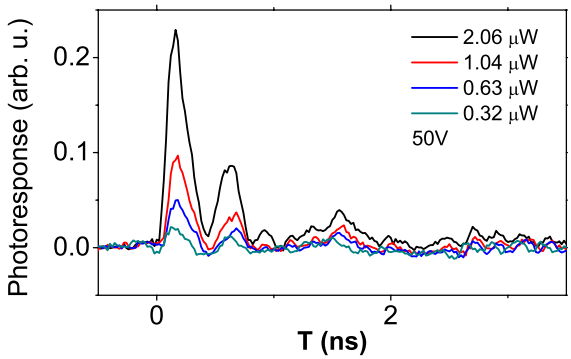

Figure 3.8. Transient photo-response of Pc-TIPS film with varied beam intensity, measured with early version of sample fixture, exhibiting severe "ringing."

3.1.4 Evolution of the Sample Fixture

A critical component of the overall experimental setup is the fixture in which the sample is embedded. An early version of the fixture may be seen in Figure 3.6. The fixture used in our investigations of real-time transient photocurrents went through several design iterations. A generic schematic may be seen in Figure 3.7.

In view of the fact that the fixture is employed for the acquistion of data on very short time–scales, with correspondingly high–frequency Fourier components, the high–frequency characteristics of the fixture are very important. This was the principal factor driving the design through its various versions. If a good impedance match is not achieved between the sample/load–resistor circuit node and the output coaxial cable, one sees "ringing," a high–frequency inductor/capacitor (LC) oscillation superimposed on the transient waveform. The length of signal paths is critical. For example, paths at the 3-way junction between the sample, the load-resistor, and the center–conductor of the output coaxial cable must all be on the order of 1 mm in length. Any non–zero signal path means a non-zero conductor length, which is a small, but non–zero inductance, which may have a significant effect on the high–frequency behavior of the fixture. Zero–mm length would be preferable, but is difficult to achieve. An example of transient photo-responses measured with an early version of the fixture is shown in Figure 3.8. This may be compared with a transient photoresponse, on the same time scale, taken with a later version of the fixture, shown in Figure 3.10. It can be seen that the waveform from the earlier fixture shows severe "ringing." The decay profile of the later waveform is not perfectly smooth, but it is much improved. The difference between the two signals corresponds to the difference between the fixtures shown in Figures 3.6 and 3.9.

Also, of great importance is the RC time constant. As will be discussed below, this plays a large role in determining the contributions of displacement currents to the transient photoresponse. The RC time constant of the measurement circuit here is taken to be that given by the electrode pair capacitance and the 50 Ohm input impedance of the DSO sampling head. For an interdigitated coplanar electrode pair with electrodes of length L and with electrode width equal to electrode spacing w_{sp}, and active area A, the capacitance of the pair is found from[83]

$$C = \epsilon \frac{A}{L} \frac{K'(sin(\frac{\pi w_{sp}}{2L})}{2K(sin(\frac{\pi w_{sp}}{2L})}, \tag{3.1}$$

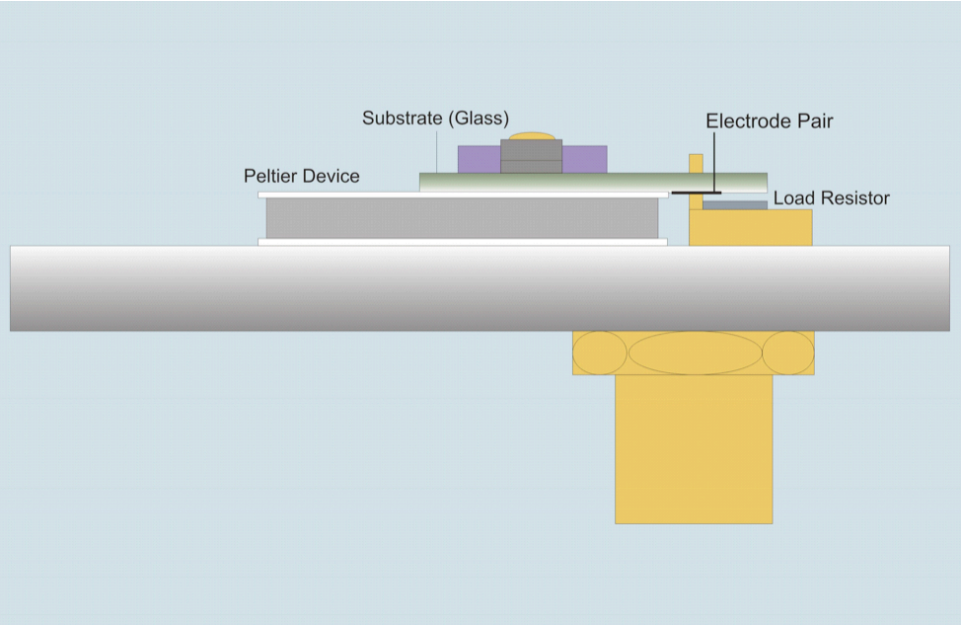

Figure 3.9. Later version of fixture. Electrode pair is shown end view.

where K and K' are the complete and the complementary complete elliptic integral, respectively, of the first order. The capacitance of our electrode pair is calculated from this to be approximately 76 femtoFarads. Assuming the resistance R in the circuit is 50 ohms, the input impedance of the DSO, one obtains an RC time constant of approximately 4 ps. The time-resolution of the DSO is defined by the shortest rise-time which it is capable of measuring, 7 ps.

Transient photocurrents obtained in ADT-TIPS-F, Pc-TIPS and DCDHF films upon excitation with 400-nm pulses at the fluence of 30 μJ/cm^2 and applied electric field of 1.2×10^4 V/cm are shown in Fig. 3.10. The data in this figure show rise-times of $\sim$30 ps. This is longer than both the DSO time-resolution limit and the theoretical RC time constant derived above. This suggests the presence of approximately 2 picofarads stray capacitance in the fixture setup.

The data establishes an upper limit of 30 ps for carrier photogeneration-times in all materials under study, in agreement with similar studies of tetracene single crystals[92] and with pump-probe data for similar materials.[7–10]

3.2 Results

The data presented in this chapter cover a wide range of time scales, from ∼30 picoseconds to tens of seconds. It will be seen that, at the two extremes of the time scales chosen, the mechanisms governing transport couple differently to such environmental parameters as temperature, field strength and light fluence. After an initial photoexcitation, the form of transport evolves through time as the excitation relaxes, and carriers interact more strongly with the lattice and become more localized. This means, for example, that carrier transport on long time-scales is likely to be more affected by temperature, or affected differently.

3.2.1 Transient Photoresponse

Transient photocurrents obtained in ADT–TIPS–F, Pc–TIPS and DCDHF films upon excitation with 400-nm pulses at the fluence of 30 μJ/cm^2 and applied electric field of 1.2×10^4 V/cm are shown in Fig. 3.10. The rise-time of the transient photoresponse observed in all samples was about ∼30 ps, a measure, as discussed above, of the time resolution of our setup.

Transients: general description. The behavior which was observed in this study, in transient photocurrents in ADT–TIPS–F and Pc–TIPS films, has been previously observed in several organic crystals.[8–10] The principal features of this behavior are: a fast initial decay, followed by a slow component. The fast initial decay is most likely due to deep trapping or to fast recombination of photoexcited carrier pairs; the slow componnet can be fitted with a power-law function ($I_{ph} \propto t^{-\beta}$) with $\beta \sim$ 0.5-0.7 over at least three orders of magnitude (inset of Fig. 3.10). (However, on the question of recombination versus trapping, see Chapter 4, Section 4.5.2.) This is independent of temperature in the range studied. In agreement with previous studies,[8,9] Pc–TIPS films of different quality showed considerable variation in the relative contribution of the fast and slow components to decay dynamics, particularly initial decay. This reflects deep trap density variation from film to film, and is consistent with the fast (∼200 ps) decay

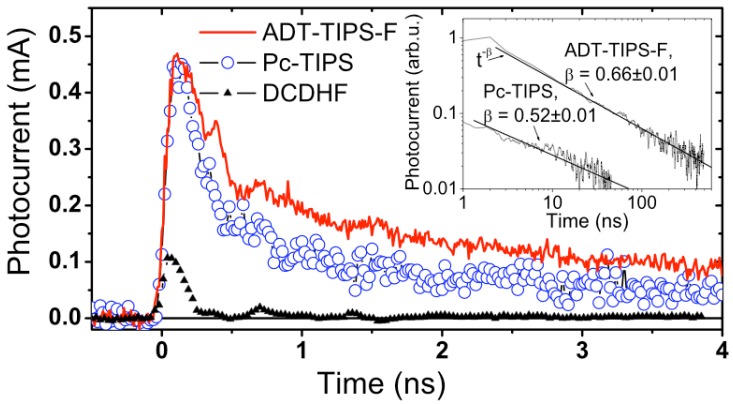

Figure 3.10. Transient photocurrent obtained in ADT–TIPS–F, Pc–TIPS and DCDHF films at 1.2×10^4 V/cm and 30 μJ/cm^2 at 400 nm. Inset: Normalized transient photocurrents (I_{ph}) in ADT–TIPS–F and Pc–TIPS films. Power-law fits ($I_{ph} \propto t^{-\beta}$) are also shown. Offset along y-axis is for clarity.

observed in the DCDHF amorphous glass (Fig. 3.10), which is known to have a high trap density (needed for excellent photo-refractor performance).[3,25,26] In any ADT–TIPS–F sample, the initial decay was less pronounced than that in the best Pc–TIPS films and even Pc–TIPS single crystals,[32] which may imply lower deep trap density in ADT–TIPS–F. A slower initial decay at higher electric fields in ADT-TIPS-F films (Fig. 3.11), which was not as pronounced in other materials, could be due to field-assisted detrapping of the carriers that became trapped in the first ∼30 ps after photoexcitation. This essentially increases the effective carrier lifetime. This would suggest shallower traps in ADT-TIPS-F, supported by the CW photoconductivity results discussed below.

Also, in ADT–TIPS–F films, transient photocurrent (inset of Fig. 3.10) did not completely decay up to at least microsecond time-scales, which suggests transport of mobile charge carriers even at >1μs after photoexcitation. In contrast, in the DCDHF amorphous glass, a fast decay, attributed to charge trapping at deep traps, was observed (Fig. 3.10). This prevented observation of mobile carriers in DCDHF at times longer than approximately 200 ps after photoexcitation.

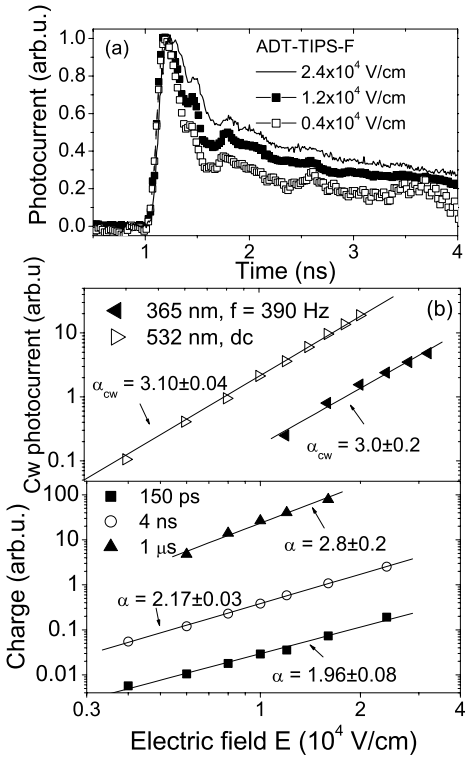

Figure 3.11. (a) Normalized transient photocurrents obtained in an ADT–TIPS–F film at various electric fields. (b) Bottom: The total charge (Q), obtained by integrating transient photocurrent with respect to time, collected over 150 ps, 4 ns and 1 μs after photoexcitation of an ADT–TIPS–F film as a function of electric field. The power-law fits ($Q \propto E^{\alpha}$) are also shown. Top: Photocurrents (I_{CW}) obtained in the same sample under CW photoexcitation as a function of electric field. CW photocurrents measured at 532-nm excitation under dc conditions and at 365-nm excitation at a chopper frequency (f) of 390 Hz are shown. The power-law fits ($I_{CW} \propto E^{\alpha_{CW}}$) are also included.

In GaAs, the ultrafast photoconductivity is generally a complicated function of time.[85] However, under our experimental conditions, the decay dynamics obtained in GaAs samples could be approximated by a bi-exponential function. At 400-nm excitation, time constants of τ_1=0.118±0.001 ns and τ_2=2.1±0.3 ns were obtained. The latter

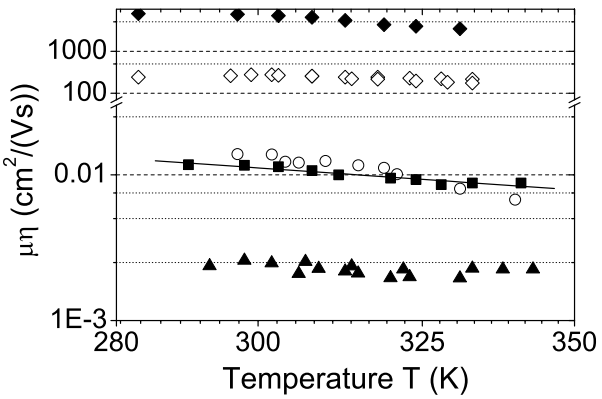

Figure 3.12. Product of mobility and photogeneration efficiency, ($\mu\eta$), obtained from the peak transient photocurrent in ADT–TIPS–F, Pc–TIPS, DCDHF films (solid squares, open circles, and solid triangles, respectively) at 1.2×10^4 V/cm at 400 nm and in GaAs at 150 V/cm at 800 nm (solid diamonds) and 400 nm (open diamonds) as a function of temperature. A power-law fit ($\mu\eta \propto T^{-n}$)to the ADT–TIPS–F data, with n=2.3±0.2, is also included.

time constant (τ_2) is in the range of bulk carrier lifetimes reported in the literature for similar samples (e.g. 2.1 ns in Ref.[85] and 3.5 ns in Ref.[86]). However, since at 400 nm the light penetration depth is only 14.5 nm,[87,88] τ_2 could still be affected by recombination at surface states, the process mostly likely responsible for fast initial carrier decay characterized by a time constant of τ_1.

Electric field dependence. In all samples, electric field dependence of the transient photocurrent amplitude could be described by a power-law function $I_{ph} \propto E^{\alpha}$) in the range of electric fields studied ((0.4-4)$\times10^4$ V/cm in organic samples and 25-250 V/cm in GaAs). GaAs exhibited linear dependence of the transient photoresponse on the electric field (i.e. $\alpha \approx 1$). In contrast, in organic films, α varied between 1 and 1.8, depending on the sample. This is consistent with $\alpha \approx 1.6$ in tetracene single crystals recently observed in a similar experiment.[92]

The electric field dependence of the shape of the transients, especially pronounced in ADT–TIPS–F films (Fig. 3.11), leads to a systematic change in α as a function

of the time after photoexcitation. Figure 3.11(b,bottom) illustrates time evolution of the electric field dependence of the collected charge (Q), obtained by integrating the transient photocurrent with respect to time in an ADT–TIPS–F sample, up to 150 ps, 4 ns, and 1μs after photoexcitation. In this sample, α describing the field dependence of the amplitude of the transient photocurrent (data not shown) is 1.8±0.1. As seen from Fig. 3.11(b, bottom), α obtained from power-law fits ($Q \propto E^{\alpha}$) increases from 1.96±0.08 at 150 ps to 2.8±0.2 at 1 μs after photoexcitation. Also included in Fig. 3.11(b, top) are electric field dependencies of the CW photocurrent (I_{CW}) in this sample, measured under CW excitation at 365 nm at the chopper frequency (f) of 390 Hz and at 532 nm under dc conditions (Sec.III.B). Power-law exponents α_{CW} obtained from fits with a power-law function $I_{CW} \propto E^{\alpha_{CW}}$ yield 3.0±0.2 and 3.10±0.04, respectively, and are higher than those observed in the transient photocurrent experiments, as discussed in Sec. 3.2.2.

The product of charge carrier mobility and photogeneration efficiency ($\mu\eta$). In all samples, transient photocurrent was linear with respect to beam fluence, implying negligible contributions from nonlinear optical effects or from bi-molecular recombination. From the peak values of the photocurrent, a product of charge carrier mobility (μ) and photogeneration efficiency (η) was calculated from the relation $\mu\eta = j_0/(n_{phot}eE)$, where$j_0$ is peak photocurrent density, E is the field, e is electron charge, and n_{phot} is the density of absorbed photons per pulse. (This relation is derived in Appendix A.) Generally, μ is a sum of electron and hole mobilities, but in the materials under discussion it is essentially mobility of the majority charge carrier: electrons in GaAs, holes in ADT-TIPS-F, Pc-TIPS, and DCDHF. The photogeneration efficiency η incorporates carrier loss due to trapping and recombination during the first ∼30 ps after excitation, not resolved in this experiment. It will be much less than the initial efficiency, η_0, the number of carriers photogenerated per number of absorbed photons. Even in the best Pc-TIPS films, more than 90% of photogenerated carriers are trapped or recombined within ∼30 ps after photoexcitation, as observed in optical pump-terahertz (THz) probe experiments.[8,9] An analogous effect on $\mu\eta$ appears in

values obtained for GaAs at 800-nm and 400-nm excitation (Fig.2). Assuming $\eta = 1$ at both wavelengths, the value for $\mu\eta$ of ~7500 $cm^2/(Vs)$ at 800 nm is consistent with Hall-effect measurements,[87] while that obtained at 400 nm is much lower. This arises from differences in absorption coefficient at these wavelengths[87] leading to a fast charge recombination at the surface at 400 nm. The $\mu\eta$ values obtained at room temperature

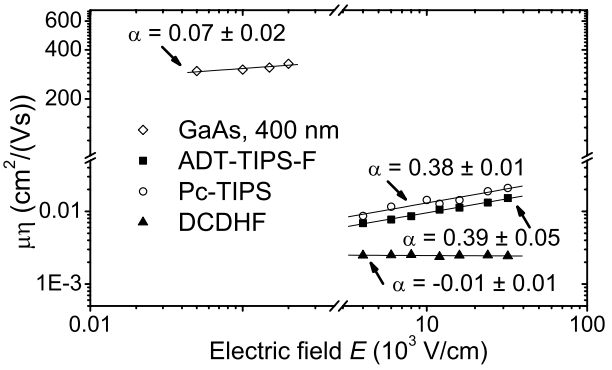

Figure 3.13. Product of mobility and photogeneration efficiency, ($\mu\eta$), obtained from the peak transient photocurrent in ADT-TIPS-F, Pc-TIPS, DCDHF films and GaAs at 400 nm as a function of applied electric field. Data from GaAs transients at 800 nm are also included. Power-law ($\mu\eta \propto E^{\alpha}$)fits are shown.

(RT) of 295 K as a function of applied electric field (E) are shown in Fig. 3.13, fitted with a power-law function $\mu\eta \propto E^{\alpha}$. In GaAs, almost field-independent mobility is observed, as expected at low electric fields. In ADT-TIPS-F and Pc-TIPS films, α varied between 0.4 and 0.8, depending on the sample, in agreement with α~0.6 in tetracene single crystals.[92] In organic semiconductors, at low fields, field-independent charge carrier mobility is predicted.[93] Therefore, the observed sublinear field dependence of $\mu\eta$ is incorporated in η, due to either field-assisted charge photogeneration or slightly field-dependent carrier lifetime (e.g. that in Fig. 3.13(d)) during the first 30 ps after excitation. The latter mechanism seems more plausible, considering the absence of field dependence of $\mu\eta$ in the DCDHF glass, in which significant deep trap density is not likely to be affected by low electric fields enough to contribute to field dependence of

the carrier lifetime at ps time scales. At E=3×10^4 V/cm, the $\mu\eta$ values obtained in ADT-TIPS-F, Pc-TIPS and DCDHF films are ∼0.018-0.025 $cm^2/(Vs)$ and ∼0.01-0.022 $cm^2/(Vs)$ and ∼0.002-0.004 $cm^2/(Vs)$, respectively, depending on the film quality.

Temperature dependence of transient photocurrent. The temperature dependence of the $\mu\eta$ values is shown in Fig. 3.12. In all organic samples, the $\mu\eta$ product decreased as the temperature increased from 285 K to 350 K, a trend qualitatively similar to that observed in GaAs (Fig. 3.12). As discussed in Chapter 2, one possible explanation for such behavior is that charge carrier mobility decreases as the temperature increases. This has been attributed by many to "bandlike" charge carrier transport in crystalline materials.[7–10,66,89,90,92] For example, a power-law dependence of charge carrier mobility (μ) as a function of temperature ($\mu \propto T^{-n}$), with n=0.5–3 is typical of band transport,[66] and has been observed in a variety of organic crystals and thin films.[7–10,61,66,89,90,92] The temperature dependence of the $\mu\eta$ values in ADT–TIPS–F and Pc–TIPS samples could also be fitted with the power-law function ($\mu\eta \propto T^{-n}$), with, for example, n=2.3±0.2 in an ADT–TIPS–F film in Fig. 3.12. Interestingly, DCDHF amorphous glass, in which CW photocurrent is strongly thermally activated (Sec. 3.2.2 and Ref.[26]), also showed a slight decrease in $\mu\eta$ extracted from the transient photocurrent on the picosecond time-scales as a function of temperature. In this case, it could be due to mobility decreasing due to increased disorder caused by a local motion of the DCDHF side groups,[26] an effect similar to that of the torsional disorder affecting sub-picosecond photoconductivity in a photoconductive polymer MEH-PPV.[91] In all samples, no significant change in the transient photocurrent dynamics as a function of temperature was observed.

3.2.2 CW photoconductivity

Wavelength and electric field dependence. In all organic samples studied, at the electric field of ∼10^4 V/cm, even at the lowest light intensity of 0.5 mW/cm^2 the CW photocurrent under dc conditions was at least an order of magnitude higher than

the dark current. Under 365-nm and 532-nm photoexcitation, the photocurrent (normalized by the number of absorbed photons) measured under similar conditions yielded similar values, and exhibited similar electric field, light intensity, and chopper frequency dependencies. This suggests similar charge photogeneration mechanisms operating at these wavelengths. The electric field dependence of the CW photocurrent (I_{CW}) can be characterized by a power-law function ($I_{CW} \propto E^{\alpha_{CW}}$), with $\alpha_{CW} \approx 1$ in GaAs and α_{CW} varying between 1.8 and 3.2 in organic films, depending on the sample. Within the same sample, however, the field dependence of the CW photocurrent is stronger than that of the transient photocurrent (i.e. $\alpha_{CW} > \alpha$), as illustrated in Fig. 3.11(b).

Chopper frequency dependence. The dependence of the CW photocurrent (I_{CW}) on chopper frequency (f) can be described by a power-law function $I_{CW} \propto f^{-\gamma}$ at both 532 nm and 365 nm (Fig. 3.14(a)). The exponent γ decreased as light intensity (I) increased in all samples, except for GaAs, in which frequency-independent response ($\gamma \approx 0$), characteristic of band transport,[94] was observed at all intensities (Fig. 3.14(b)). In organic samples, $\gamma \sim 0.5$ was observed at 1 mW/cm^2 and reached values as low as $\gamma = 0.07 \pm 0.02$ in the ADT–TIPS–F film at 25 mW/cm^2. At light intensities above 20 mW/cm^2, an almost frequency-independent photocurrent is observed in ADT-TIPS-F films, which suggests that most charge carriers contributing to the photocurrent under these conditions move in the extended states, as in GaAs. This is consistent with two channels of charge transport at low light intensities, with some carriers propagating in extended states and others in somewhat localized states, while at higher light intensities, the extended-state channel predominates, due to light-induced trap filling. In Fig. 3.14(b), lower trap density (i.e. more efficient trap filling) is observed in ADT-TIPS-F compared to Pc-TIPS and DCDHF, in agreement with the transient photoconductivity results.

Light intensity dependence. The dependence of the CW photocurrent on light intensity can be described by a power-law function ($I_{CW} \propto I^b$), characterized by the exponent b varying with chopper frequency. Figure 3.15(a) shows the light intensity

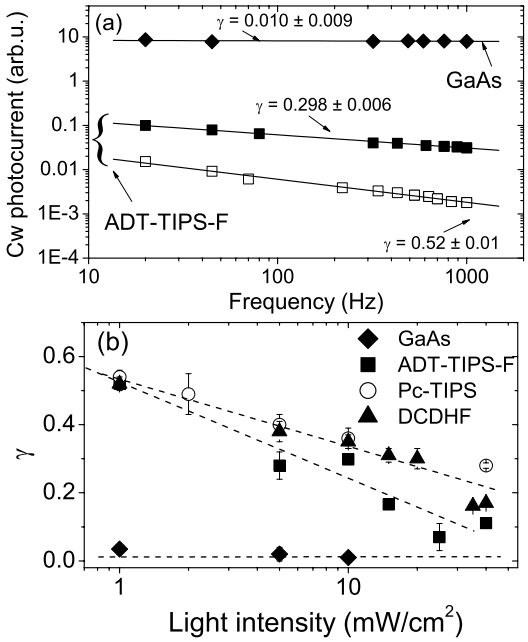

Figure 3.14. (a) CW photocurrent as a function of chopper frequency (f) obtained in the ADT–TIPS–F film at 1 mW/cm^2 (open squares) and 10 mW/cm^2 (solid squares) at 1.2×10^4 V/cm, as well as in GaAs at 1 mW/cm^2 at 150 V/cm, all at 532 nm. Power-law fits ($I_{CW} \propto f^{-\gamma}$), with exponents γ, are also shown. (b) Exponents γ as a function of light intensity obtained in ADT–TIPS–F, Pc–TIPS, and DCDHF films and GaAs. The lines are guides for the eye.

dependence of CW photocurrent obtained in the ADT–TIPS–F film at a chopper frequency of 20 Hz, 390 Hz, and 1 kHz at 532-nm excitation. In this sample at 20 Hz, the exponent b is 0.71±0.04. As the chopper frequency increases, the exponent b increases, reaching 1.02±0.03 at 1 kHz, corresponding to linear dependence of the CW photocurrent on light intensity. A similar trend is observed in Pc–TIPS and DCDHF films, as illustrated in Fig. 3.15(b), although at low frequencies the intensity dependence in these films is closer to linear than that in the ADT–TIPS–F films. In GaAs, linear intensity dependence of the CW photocurrent, characteristic of monomolecular recombination, is observed at all frequencies (Fig. 3.15).

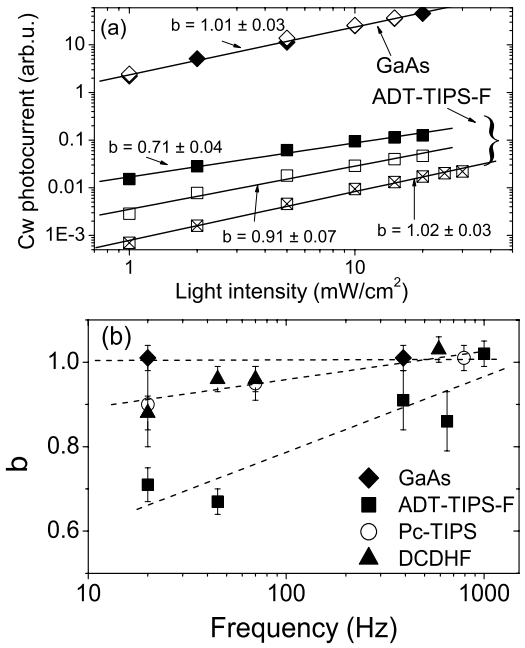

Figure 3.15. (a) CW photocurrent as a function of light intensity (I) obtained in an ADT–TIPS–F film at 20 Hz, 390 Hz and 1 kHz (solid, open, and crossed squares, respectively) at 1.2×10^4 V/cm, as well as in GaAs at 390 Hz and 1 kHz (solid and open diamonds, respectively) at 150 V/cm, all at 532 nm. Power-law fits ($I_{CW} \propto I^b$), with exponents b, are also shown. (b) Exponents b as a function of chopper frequency obtained in ADT–TIPS–F, Pc–TIPS, and DCDHF films and in GaAs. The lines are guides for the eye.

Temperature dependence of CW photoresponse. The temperature dependence of CW photoresponse obtained in ADT–TIPS–F, Pc–TIPS, and DCDHF films, as well as in GaAs sample, at 532-nm excitation with 0.5 mW/cm^2 at a chopper frequency f of 1 kHz and under dc conditions is presented in Fig. 3.16(a) and (b), respectively. In ADT–TIPS–F films, the temperature dependence of the photoresponse measured at f=1 kHz showed a sample-to-sample variation, ranging between slightly negative temperature dependence (i.e. photoresponse decreasing with increasing temperature) and

thermally activated response ($I_{CW} \propto \exp[-\Delta/(k_B T)]$, where k_B is the Boltzmann constant), with the activation energy Δ up to ∼0.09 eV (Fig. 3.16(c), solid squares). Under dc conditions, however, the same samples exhibited a thermally activated CW photocurrent, with the activation energy Δ reaching ∼0.17 eV (Fig. 3.16(c), open squares). Interestingly, at 1 kHz, the photoresponse in all Pc–TIPS samples studied decreased as the temperature increased (Fig. 3.16(a)), a behavior similar to that of the amplitude of transient photocurrent obtained on picosecond time-scales (Fig. 3.12). Under dc conditions, however, either temperature independent or weakly thermally activated response was observed (Fig. 3.16 (b)), with the activation energies Δ up to ∼0.05 eV, depending on the sample. In both experiments (i.e. at 1 kHz and under dc conditions), DCDHF amorphous glass samples exhibited thermally activated behavior, with Δ of ∼0.24–0.26 eV (Fig. 3.16 (c)), a behavior similar to that observed in PR glasses containing previously studied DCDHF derivatives sensitized with C_{60}.[26] CW photoresponse in GaAs decreased as the temperature increased (Fig. 3.16(a) and (b)), reflecting the temperature dependence of charge carrier mobility characteristic of band transport.

From dc photocurrents obtained at 532-nm excitation (Fig. 3.16(b)), a product of mobility (μ), initial photogeneration efficiency (η_0) and average time the carrier travels before trapping and recombination (τ) was calculated using $\mu\eta_0\tau = j_{dc}/(n_{phot}eE)$, where j_{dc} is dc photocurrent density.[74] At room temperature at 0.8×10^4 V/cm, $\mu\eta_0\tau$ values for ADT–TIPS–F were $\sim6\times10^{-9}$ cm^2/V, similar to those observed in C_{60} thin films[97] and inorganic amorphous semiconductors.[94] In Pc–TIPS and DCDHF, the corresponding values were up to one and two orders of magnitude lower, respectively (Fig. 3.16).

3.3 Discussion

There are some significant similarities between charge transport in GaAs and in the organic semiconductors studied here. In all the materials under investigation, charge carriers are photogenerated on ps (most likely sub-ps[8–10]) time scales (Fig. 3.13) and exhibit charge transport in extended states, while slowly relaxing into more localized

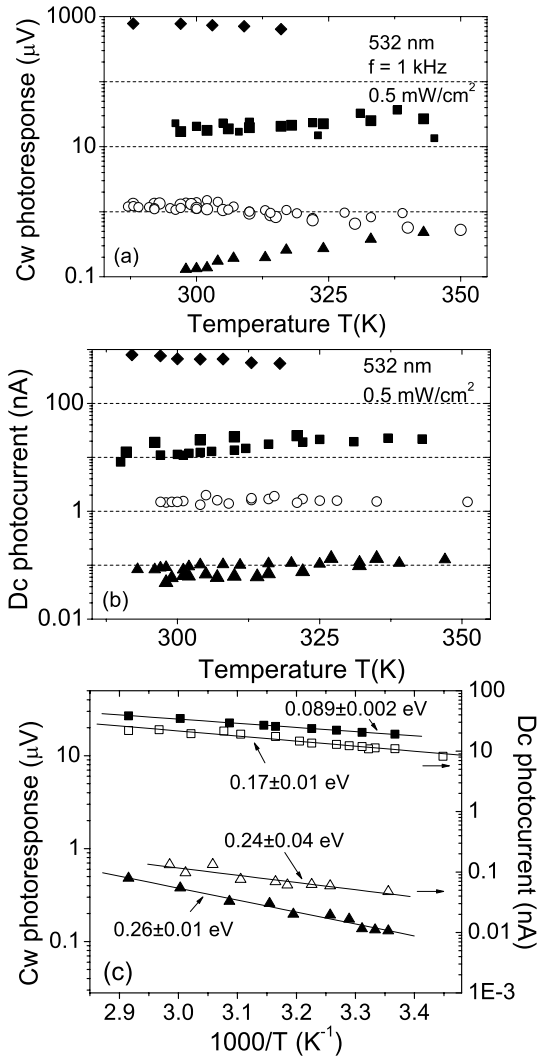

Figure 3.16. CW photocurrent as a function of temperature (T) obtained in ADT–TIPS–F, Pc–TIPS, and DCDHF films (solid squares, open circles, and solid triangles, respectively) at 0.8×10^4 V/cm and in GaAs (solid diamonds) at 100 V/cm at light intensity of 0.5 mW/cm^2 at 532 nm: (a) at a chopper frequency f of 1 kHz, and (b) under dc conditions. Double and triple symbols of different sizes correspond to different samples. (c) CW photocurrent in one of the DCDHF (triangles) and ADT–TIPS–F (squares) samples replotted as a function of 1/T: at f=1 kHz (solid symbols, left axis) and under dc conditions (open symbols, right axis). Arrhenius fits ($I_{CW} \propto \exp[-\Delta/(k_B T)]$), with corresponding activation energies Δ, are also shown.

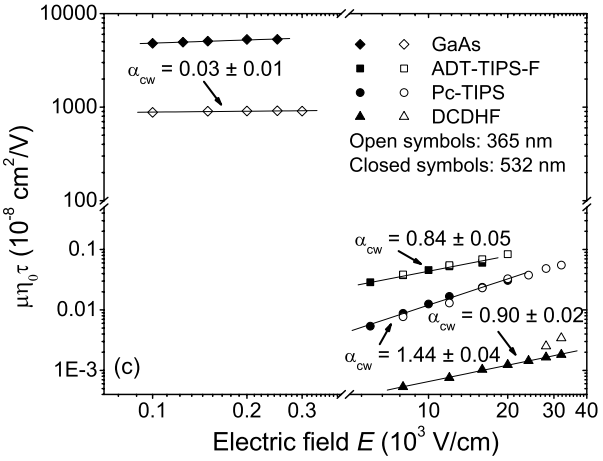

Figure 3.17. Product of mobility, initial photogeneration efficiency, and carrier lifetime, $\mu\eta_0\tau$, obtained from CW photocurrents at 532 and 365 nm as a function of electric field. Power-law fits ($\mu\eta_0\tau \propto \mathrm{E}^{\alpha_{CW}}$) are also shown.

states (inset of Figs. 3.12 and 3.17). An electric field may assist in detrapping carriers into the extended states manifold, prolonging the effective carrier lifetime (Fig. 3.13). Conversely, increased carrier lifetime, and carrier transport predominantly in extended states may also be seen when the majority of traps are filled, as observed in CW photocurrent with increased light intensity (Fig. 3.15). A similar trap-filling effect manifests itself as slower decay of the transient photocurrent at higher light fluences, observed on ps time scales in optical pump-THz probe experiments in pentacene single crystals.[7] Dynamics after photoexcitation, when more carriers become localized and move by thermally-assisted hopping, depends on the structure and morphology of the films: at ms time scales, in DCDHF amorphous glass, the carriers are more localized than those in polycrystalline ADT-TIPS-F or Pc-TIPS films. From $\mu\eta$ values of ∼0.02 cm^2/(Vs) obtained in ADT-TIPS-F and Pc-TIPS films and using TFT mobility values of ∼1 cm^2/(Vs) in similar films,[24] one can estimate a lower limit of photogeneration efficiency η ∼0.02, similar to that obtained in tetracene single crystals in similar experiments.[92]

If one assumes, in CW photoconductivity experiments under trap-filled conditions, that one is observing the same carriers propagating in the extended states as those at ps time scales, then μ in $\mu\eta$ is the same as in $\mu\eta_0\tau$. Then, in the case of Pc-TIPS for example, if one assumes the average carrier lifetime τ to be $\sim$1 ns, then the initial η_0 estimated from $\mu\eta_0\tau$ values would be $(3.3\times10^{-10}\text{cm}^2/\text{V})/(1\ \text{cm}^2/(\text{Vs})\times 10^{-9}\ \text{s}) = 0.33$. This is consistent with the value for η of 0.02 obtained in the transient photoconductivity experiments, if it is coupled with the 90% carrier loss, during the first 30 ps after excitation, observed in previous studies.[8,9]

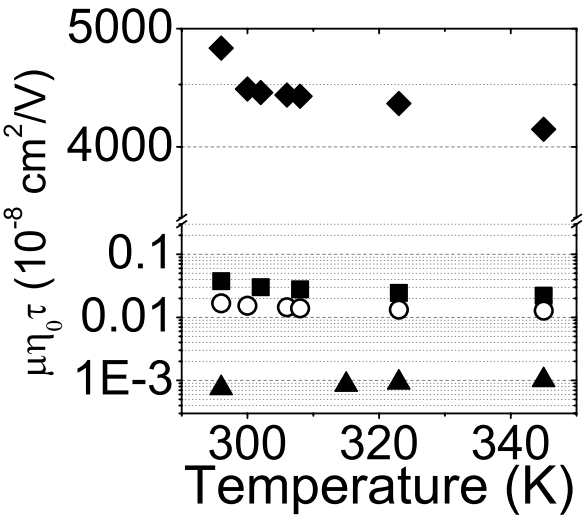

Figure 3.18. Product of mobility, initial photogeneration efficiency, and carrier lifetime $\mu\eta_0\tau$ as a function of temperature at 1.2×10^4 V/cm (organic films) and 1.5×10^2 V/cm (GaAs).

3.3.1 Photogeneration efficiency

In all the materials studied here, including DCDHF amorphous glass, mobile charge carriers are photogenerated on picosecond (most likely sub-picosecond[8–10]) time–scales (Fig. 3.10). From $\mu\eta$ values of $\sim$0.02 cm^2/(Vs), calculated from amplitudes of transient photocurrents obtained in ADT–TIPS–F and Pc–TIPS films at 1.2×10^4 V/cm,

and using TFT mobility values of $\sim$1 cm^2/(Vs) in similar films,[24] one can estimate a lower limit of photogeneration efficiency $\eta \sim 0.02$ at this field, similar to that obtained in tetracene single crystals in experiments utilizing Auston-switch geometry.[92] Furthermore, η is smaller than η_0 (Sec. 3.2.1). As mentioned above, in previous studies of Pc–TIPS films using optical pump–THz probe time–resolved spectroscopy,[8,9] more than 90% carrier loss occurred during the first 30 ps (which is the time resolution of our transient photoconductivity setup) after photoexcitation. If a similar trend persisted under conditions of the experiments presented here, it would make the initial photogeneration efficiency η_0 in, for example, Pc–TIPS films to be at least $\sim$0.2. The $\mu\eta$ value obtained from the amplitude of the transient photocurrent in DCDHF amorphous glass is rather high, reaching 0.004 cm^2/(Vs), which is only a factor of $\sim$6 lower than that in the best polycrystalline ADT–TIPS–F and Pc–TIPS films. A similar difference in $\mu\eta$ was observed on sub-picosecond time-scales in amorphous and polycrystalline Pc–TIPS films,[9] which may suggest that $\mu\eta$ values similar or higher than those observed in Pc–TIPS films could be obtained in the crystalline phase of DCDHF.[25,99]

3.3.2 Transient decay

Before proceeding to a general discussion of the results for transient photocurrents, the issue of the contribution of displacement currents should be addressed. Frankevich has shown[84] that, in a configuration such as described here, displacement current may make a significant contribution to an observed transient photoconductivity signal. He shows, furthermore, that it is possible that two very similar transient photoresponse waveforms may be composed, on the one hand, of displacement current and one type of free charge carriers, or, on the other hand, of two types of free charge carriers of different lifetimes. The magnitude of the RC time constant of the measuring circuit, relative to the life-times and populations of free carriers, is the primary factor governing the relative contribution of the displacement current. One may follow Frankevich's analysis,[43,84] using an RC time-constant of 30 ps, extracted from the above analysis of the fixture time-constant (Section 3.1.4) and from the observed rise-times, and assuming

lifetimes for free carriers of 0.2 ns and for excitons of 1.5 ns. With these assumptions, simulations yielded the result that the photocurrents in Fig. 3.10 are not displacement currents, but are rather due to mobile photogenerated carriers. Data in Fig. 3.10 establishes an upper limit of 30 ps for carrier photogeneration-times in all materials under study, in agreement with similar studies of tetracene single crystals[92] and with optical pump-THz probe data for similar materials.[7–10] A synopsis of Frankevich's analysis is given in Appendix B.

The decay dynamics of the transient photoconductivity reflects charge trapping and recombination processes. ADT–TIPS–F and Pc–TIPS films exhibit two-component decays, with a faster component on the time scale of ∼100 ps, most likely due to deep trapping, and a slower component characterized by a power-law function ($I_{ph} \propto t^{-\beta}$) with β ∼0.5–0.7 (Fig. 3.10). Similar power-law decay dynamics have been previously observed, on time-scales from ∼400 fs to at least ∼500 ps after photoexcitation, in optical pump-THz probe experiments in similar materials.[8,9,11] These dynamics were attributed to tunneling of nearly-small molecular polarons (see Chapter 2, Section 2.4). In the experiments with ADT–TIPS–F and Pc–TIPS films here described, similar transport evolution is observed, over time-scales extending into a microsecond range in the best films. The observation that the product of mobility and photogeneration efficiency ($\mu\eta$), obtained from the amplitude of the transient photoconductivity), decreases as the temperature increases (Fig. 3.12) in ADT–TIPS–F and Pc–TIPS films (Fig. 3.12), would tend to support this hypothesis. If one assumes that photogeneration efficiency η does not decrease with the temperature,[100] then this behavior would be attributed to charge carrier mobility, with a resulting dependence on temperature which is consistent with bandlike charge transport on picosecond time-scales.[7–10,66] Since decay dynamics of transient photoconductivity are temperature-independent in the range studied, this suggests that the contribution of localized carriers, either lattice polarons or carriers thermally excited out of traps, to the photocurrent is not significant up to at least microseconds after photoexcitation. This is consistent with a recent demonstration that light quasiparticles (which could be nearly-small molecular polarons), rather than heavy

lattice polarons, dominate charge transport in rubrene single crystals.[6] It also agrees with the observation in this study of non-thermally-activated behavior of CW photoconductivity, at a chopper frequency f of 1 kHz (corresponding to characteristic times of $\sim 1/(2\pi f) \approx 160$ μs), in Pc–TIPS and in some of the ADT–TIPS–F samples.

The decay dynamics of the transient photoconductivity observed in DCDHF amorphous glass indicates that most charge carriers photogenerated on the picosecond time-scales are trapped in deep traps within ~200 ps, and less than ~3% of the carriers contributing to the peak photocurrent are still mobile after only 3 ns. Interestingly, the amplitude of the transient photocurrent and of the associated $\mu\eta$ values in DCDHF amorphous films do not display the dependence on temperature which would suggest that these parameters are thermally-activated (Fig. 3.12), despite the lack of crystalline order in these samples. A small decrease in $\mu\eta$ as a function of temperature may reflect an increase in disorder, caused by highly temperature-dependent local motion of the DCDHF side groups. This has been previously observed in other DCDHF derivatives, is known to occur on microsecond time-scales at $T<T_g$ and is much faster at $T>T_g$ (T_g = glass transition temperature).[26] This would lower the intrinsic charge-carrier mobility at higher temperatures. Apparently, large-scale molecular motion activated at around T_g in DCDHF glass, which assists in CW photoconductivity (Fig. 3.16 and Ref.[26]), is too slow to contribute to the transient photocurrent.

3.3.3 Electric field dependence: field-assisted detrapping

In all organic samples, the electric field dependence of the amplitude of the transient photoconductivity was between linear ($\alpha \approx 1$) and superlinear with $\alpha \approx 1.8$. This suggests sublinear electric-field-dependence of mobility μ, photogeneration efficiency η or both. Since at the relatively low electric fields used here (up to 4×10^4 V/cm), mobility is not likely to depend on the electric field,[101] most of this dependence would be due to η.

However, the observation of an increase in α as a function of the time after photoexcitation and of α_{CW} being larger than α (e.g. in Fig. 3.11 (b)) suggests that most of

the electric field dependence does not come from the initial photogeneration efficiency η_0. Rather, it may come from the electric field-induced detrapping[50] of charge carriers trapped in very shallow traps within, for example, the first 30 ps after photoexcitation. Alternatively, it may come from the increasing contribution of another, relatively slow, process of carrier photogeneration to the photocurrent at longer time scales – for example, electric field-assisted triplet exciton dissociation. Although the dependance of the shape of the transients on electric field-strength, especially pronounced in ADT–TIPS–F films (Fig. 3.11), is more consistent with the former mechanism, detailed photophysical studies are needed to distinguish between these mechanisms.

3.3.4 Distribution of trapping states

In all organic samples, the amplitudes of CW photocurrents generated with 532-nm and 365-nm light, at the same number of absorbed photons and under the same conditions, were similar, and exhibited similar dependence on various parameters. This indicates that the mechanism of photogeneration of mobile carriers and subsequent charge transport, which generates CW photocurrent, is the same at both these wavelengths.

It was found that the dependence of the CW photocurrent on chopper frequency changes as a function of light intensity and, conversely, that the dependence of the CW photocurrent on light intensity changes as a function of the chopper frequency (Figs. 3.14 and 3.15, respectively). From these relations, one may extract information about the distribution of trapping states, as well as information about the contribution to the CW photoconductivity made by charge carriers which are trapped and then released. In the case of monomolecular recombination, the following chopper frequency dependence of the mobile carrier density and, therefore, photocurrent (I_{CW}), is expected: $I_{CW} \sim 1/(\sqrt{1+(\omega\tau)^2})$, where $\omega = 2\pi f$ and τ is the carrier lifetime.[102] At $\omega\tau \ll 1$, frequency-independent photocurrent, such as that in GaAs (Fig. 3.14), is expected. At $\omega\tau >> 1$, I_{CW} decreases with frequency as $1/\omega$ (i.e. $\gamma = 1$). Inclusion of bimolecular recombination yields the same behavior in these two limits.[102] Power-law frequency

dependence, with $\gamma < 1$, has been observed in photoinduced absorption and photoconductivity experiments in a variety of inorganic materials. This is attributed to long-lived excitations, with stronger frequency dependence reflecting higher density of defects and impurities.[103–105] Sublinear values of γ, such as those measured in the films in this study (Fig. 3.14), have also been observed in semiconducting polymers (e.g. $\gamma = 0.66$ in PPV[50] and $\gamma = 0.3$ in polydicarbazolyldiacetylene[102]), and attributed to a broad distribution of trapping states. At higher light intensities, the frequency dependence of the photocurrent is weaker in all samples. A similar trend was previously observed in inorganic semiconductors such as GaS crystals and explained by carrier lifetime decreasing as the intensity increases due to bimolecular recombination.[103] Qualitatively, a reduction in τ with intensity leads to an approach to the limit $\omega\tau \ll 1$, and results in an almost frequency-independent photocurrent. Among ADT–TIPS–F, Pc–TIPS, and DCDHF films, the ADT–TIPS–F films exhibited the strongest dependence of γ on light intensity, reaching γ of only $\sim$0.07 at 25 mW/cm^2. This is consistent with a much higher CW photocurrent, and therefore, carrier density, in ADT–TIPS–F (Fig. 3.16), which leads to an enhanced bimolecular recombination.

3.3.5 Intensity dependence

While light intensity dependence ($I_{CW} \sim I^b$) was linear in GaAs, it was sublinear (b <1) in all organic samples under dc conditions and at lower chopper frequencies, but increased to 1 at higher frequencies (Fig. 3.15). As sublinear intensity dependence is indicative of the presence of shallow traps ($0.5 < b < 1$) and bimolecular recombination ($b = 0.5$) in a material,[95] these results suggest that the contribution made by these traps to CW photocurrent , as well as that made by bimolecular recombination in the range of light intensities used in this study, is considerably lower at higher frequencies, corresponding to time-scales of several hundreds of microseconds.

3.3.6 Localization processes on longer time-scales

Comparison between temperature dependencies of the CW photocurrent observed in ADT–TIPS–F and Pc–TIPS films at $f = 1$ kHz, and under dc conditions, suggests that carrier localization still proceeds on time-scales from hundreds of microseconds to seconds. Further, it suggests that the contribution to the CW photocurrent, made by localized carriers moving by thermally-activated hopping, increases as the time progresses. In the dc limit (time-scales of tens of seconds), thermally activated CW photoconductivity is observed in most ADT–TIPS–F and Pc–TIPS samples. Larger activation energies Δ obtained in ADT–TIPS–F films, compared to those in Pc–TIPS films (up to 0.17 eV, and 0.05 eV, respectively), suggest broader distribution of trapping sites in the ADT–TIPS–F. A much higher CW photoconductivity observed in ADT–TIPS–F films compared to Pc–TIPS ones, in spite of their comparable transient photoconductivity, may indicate a much larger contribution by carriers detrapped from shallow traps into the CW photocurrent in ADT–TIPS–F. The traps are deeper in the Pc–TIPS, which is consistent with the decay dynamics of the transient photoconductivity (Fig. 3.10). Once carriers are trapped in these deep traps, they do not contribute to the CW photocurrent measured under the conditions of experiments in this study, but participate rather in persistent photoconductivity on the time-scales of hours.[73]

In DCDHF glass, complete carrier localization occurs on sub-millisecond time-scales (most likely sub-nanosecond time-scales, as suggested by the transient photoconductivity experiments described above). CW photoconductivity exhibits similar thermally-activated behavior at all chopper frequencies, and under dc conditions, with Δ of $\sim$ 0.24-0.26 eV. GaAs is on the other end of the spectrum, with delocalized carriers contributing to transient and CW photocurrent at all time-scales investigated.

3.4 Conclusions

In summary, the data presented in this part of this study are consistent with the following overall picture. In ADT–TIPS–F, Pc–TIPS, and DCDHF films, mobile charge

carriers are photogenerated on picosecond time-scales via non-thermally-activated mechanisms, assisted weakly if at all by electric fields. In ADT–TIPS–F and Pc–TIPS polycrystalline films, the charge transport mechanism at time-scales from tens of picoseconds to at least several hundreds of nanoseconds is consistent with tunneling of nearly-small molecular polarons. In DCDHF amorphous glass, non-thermally-activated charge transport on picosecond time-scales is observed, and is negatively affected by disorder caused by local motion of the DCDHF side groups. As soon as ∼200 ps after photoexcitation, in these films, most charge carriers are already trapped or recombined. At room temperature at 1.2×10^4 V/cm, values obtained for the product of mobility and photogeneration efficiency, $\mu\eta$, in ADT–TIPS–F, Pc–TIPS and DCDHF films are $\sim$ 0.018 – 0.025 $cm^2/(Vs)$ and $\sim$ 0.01– 0.022 $cm^2/(Vs)$ and $\sim$ 0.002 – 0.004 $cm^2/(Vs)$, respectively, depending on the film quality.

On time scales from hundreds of microseconds to seconds after photoexcitation, an increasing contribution of localized carriers to photocurrent, together with an increasing role played by traps and, at higher light intensities, by bimolecular recombination, is observed in ADT–TIPS–F and Pc–TIPS films. At these time-scales, only thermally-activated hopping of localized charge carriers is observed in DCDHF glass. Although photoconductivity on picosecond time-scales is similar in ADT–TIPS–F films and Pc–TIPS films, it becomes much higher on longer time-scales in ADT–TIPS–F. It is suggested that this is associated with a larger contribution to photocurrent in ADT–TIPS–F from carriers detrapped from shallow traps. In general, the effects of trap depth, and of trapping and detrapping dynamics are more noticeable on longer time–scales.

On the Photoresponse of Several Novel Functionalized Oligoacene
and Anthradithiophene Derivatives

CHAPTER 4
DOPING: PROBING AND MANIPULATING TRANSPORT DYNAMICS

4.1 Introduction

Prior work, and particularly work in the area of photorefractive polymers, has indicated the potential of using molecular dopants as a means of exploring the molecular energy structure of organic semiconductors, and extracting information about the nature and role of both deep and shallow traps in such materials, as well as enhancing performance.[121–123] Such dopant materials may be introduced as a means of creating sites where the electron affinity and the ionization potential differ from those of the bulk material, thereby introducing into the bulk material a known density of traps, of known depth. It is also possible to choose a dopant such that the introduced dopant molecule constitutes a structural defect, which is a trap of a different sort. The electronic behavior of the material will often be altered by the additions of such dopants, sometimes dramatically. While the role of dopants in inorganic semiconductors is well understood, much work remains to be done with dopants in organics.

In this chapter, results from experiments will be described in which both sorts of dopants were introduced into ADT-TES-F thin films. Two of the dopants were closely related to ADT-TES-F, but with different ionization energies, another was the amorphous glass DCDHF, and the fourth dopant was the buckminsterfullerene C_{60}. It will be seen that the results are in some respects analogous to the known behavior of

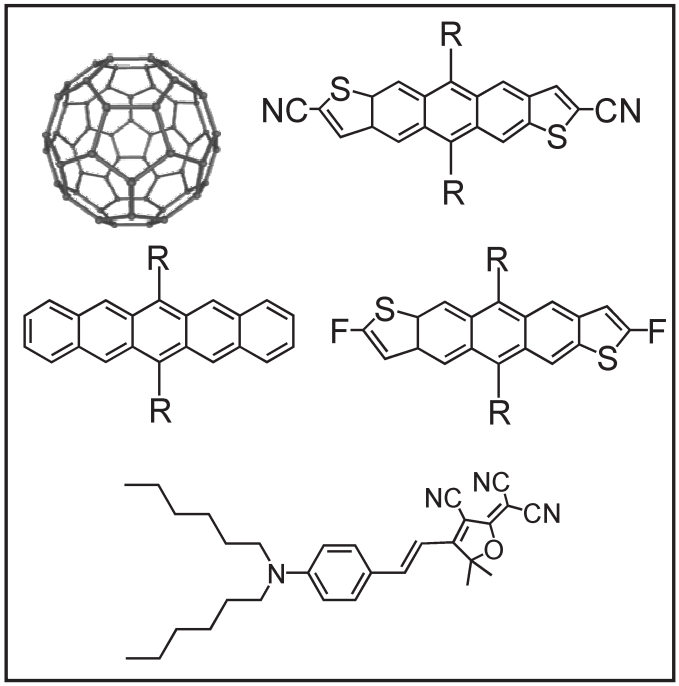

Figure 4.1. Molecular structures, clockwise from top: C_{60}, ADT-TIPS-CN (R = Si(i-Pr)$_3$), ADT-TIPS-F or ADT-TES-F (R = Si(i-Pr)$_3$ (ADT-TIPS-F), R = Si(Et)$_3$ (ADT-TES-F)), DCDHF, and Pc-TIPS (R = Si(i-Pr)$_3$).

p-type semiconductors, in which holes are the majority carrier, into which p-type or n-type dopants are introduced . But some of the results are also akin to observed behavior of disordered materials into which electron acceptors have been introduced.[49]

4.2 Materials

This part of this study used, for the bulk materials of the organic films, the novel high performance fluorinated anthradithiophene derivative functionalized with triethylsilylethynyl (TES) side groups, ADT–TES–F,[2] (Fig. 4.1). As described before, ADT–TES–F exhibits brick-wall-type crystal packing, with significant π-overlap,[2,80]favoring high TFT mobility.[24] It forms polycrystalline films[9] when deposited from solution, with the a-b plane in the plane of the film.

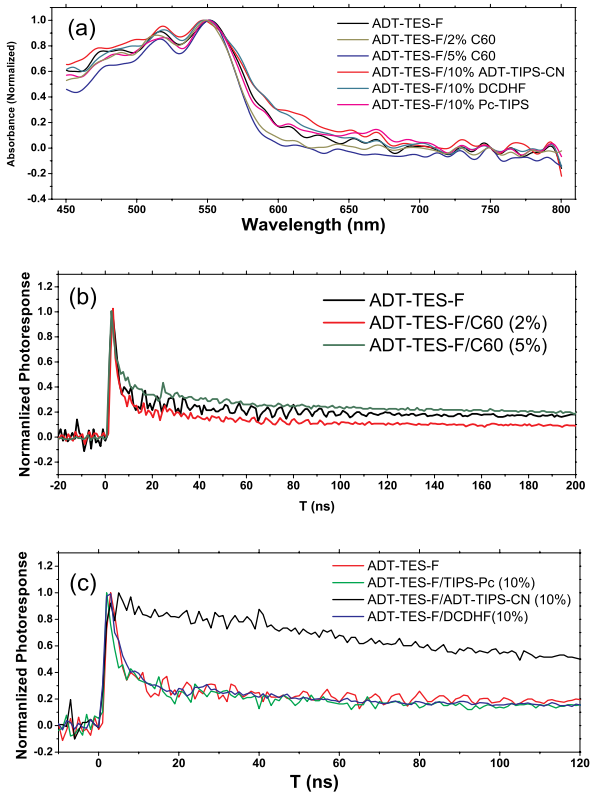

Figure 4.2. (a) Optical absorption spectra of ADT–TES–F films, pristine and with dopants. (b) Transient photocurrents obtained in ADT–TES–F films, pristine and doped with 2% and 5% concentrations by weight of C_{60} at 1.2×10^4 V/cm and 30 μJ/cm^2 at 400 nm. (c) Transient photocurrents in ADT–TES–F films, pristine and doped with 10% DCDHF, Pc-TIPS, and ADT-TIPS-CN

For dopants, two classes of materials were used. One was the buckminsterfullerene C_{60}, an electron acceptor. The material parameter for C_{60} which is most relevant to what follows is the electron affinity, which is 2.65 eV. The other class of dopants consisted of organic molecules: Pc-TIPS and DCDHF, described in Chapters 1 and 3, and the anthradithiophene derivative ADT-TES-CN. Pc-TIPS and ADT-TIPS-CN are materials which are structurally similar to the bulk material, and it is believed therefore that their role is primarily to introduce local discontinuities in the energy structure (electron or hole traps), without major structural deformation. The DCDHF

molecule, on the other hand, is structurally quite different from ADT-TES-F, and hence will introduce structural defects. It also strongly polar.[98] These are all shown in Figure 4.2. The energy levels of the HOMO and LUMO levels of these materials are shown in Figure 4.10.

As a way of comparing our results with the behaviors of more well known materials, data was also taken with N(polyvinylcarbazole) doped with 0.5%, 1% and 2% C_{60}. PVK sample films were spin-coated onto glass substrates prepared with an ITO layer, at 3000 rpm for 10 to 15 seconds. Gold upper electrodes were deposited in vacuum onto the PVK layer, to produce a sandwich electrode/sample geometry.

4.3 Experiment

For this study, doped polycrystalline films of the anthradithiophene derivative ADT-TES-F were prepared in the following fashion. The ADT-TES-F crystalline powder was mixed with a specific percentage concentration by weight of the given dopant, also in powder form. The "dopant concentrations" referred to below are then the percentages by weight of dopant in ADT-TES-F. The powder mixture was then dissolved in toluene, and drop-cast onto a glass substrate pre-patterned with gold interdigitated electrodes, with fingers of 25 μm width as described in Section 3.1.2, in the manner detailed in previous chapters. In order to drop-cast films thick enough to return good signals for measurements, the dopant/ADT-TES-F mixtures were mixed with the minimum amount of toluene, and the solution vial immersed in an ultrasonic bath to achieve complete dissolution.

As mentioned above, the dopants were of two kinds: in one set of experiments the dopant was the buckminsterfullerene C_{60}, in 2% and 5% concentrations by weight. In another set of experiments, the dopants were ADT-TIPS-CN, DCDHF (ZL18), and Pc-TIPS, all in 10 % by weight concentrations. (An ADT-TES-F/10% C_{60} solution was prepared, but it yielded transient responses lower than the un-doped film.) ADT-TES-F mixed with C_{60} needed significantly more time in the ultrasonic bath in order to achieve dissolution, and the C_{60} tended also to precipitate more quickly out of solution, while

in storage. Absorption spectra for the polycrystalline films, prepared as just described, are shown in Figure 4.2(a). Within the error introduced by noise in the measurement apparatus, there is no difference between the spectra.

For measurement of transient photoconductivity data for these films, the procedure was essentially the same as described in Chapters 3 and 4. The principal difference was that the Tektronix CSA8200 DSO was not available for this data set, and transient photoresponse data was taken by an Agilent DSO6032A. Dark current I-V data were taken by the Keithley 237 SMU Source-Measure-Unit (SMU). The Keithley 237 performed linear stair sweeps, in increments of 1 Volt for the 0 to 10 Volt range, and increments of 10 Volts for sweeps from 10 to 100 Volts or higher. Data for CW photocurrent as a function of voltage were taken in precisely the same way, except that the sample was excited by a Nd:YVO_4 laser at the wavelength of 532.

In order to examine carrier generation and relaxation dynamics on long (many-second) time scales, samples were placed in a 532–nm Nd:YVO_4 laser beam path, with a Thorlabs shutter to open and close the beam. The lens, shutter, and sample were so arranged that the shutter was slightly beyond the focal point, and the sample was at a point further on where the beam had expanded to 1 mm diameter. The shutter position near the focal point of the lens ensured the smallest possible transition time between beam blocked and beam open. Single-run oscilloscope traces were then taken, as a means of gathering data for the dynamics of the transition from dark current to CW photocurrent and back again. These waveforms will be referred to as "DC transients" in what follows. Data for the CW photoresponse of the samples of PVK doped with C_{60} was taken in this way.

4.4 Results

4.4.1 Transient photoresponses

Easily the most striking feature of the plots shown in Figure 4.2 is the almost complete absence, in the transient response of ADT-TES-F doped with ADT-TIPS-CN,

of the rapid decay after the initial peak, which is seen in all the other transients. The normalized transient decay profiles for the other doped samples were all quite similar to one another and to the profiles for the pristine material. However, if one examines the inset to Figure 4.3(b), one can see that on longer time scales, all of these dopants appear to be acting to shorten the tail of the decay profile, in comparison with that of the pristine material.

Doping with C_{60} clearly brings about an increase in the peak amplitude of the transients for ADT-TES-F, close to an order of magnitude for the film doped with 5% C_{60} (Figures 4.3(a) and 4.4). But although C_{60} appears to reduce the slope of the transient decay (inset, same figure), it does not produce any dramatic change in decay dynamics such as we observe with ADT-TES-F doped with ADT-TIPS-CN. (Figure 4.4(a)).

The amplitudes of transient photoresponses for ADT-TES-F thin films doped with 10% concentrations of Pc-TIPS, ADT-TIPS-CN and DCDHF are shown in Figure 4.5.

4.4.2 Dark current and photoresponse on longer time-scales

Dark current and CW photocurrents measured against voltage are shown in Figure 4.6. C_{60} enhances dark current, by less than a factor of two; it somewhat more than doubles CW photoresponse, for ADT-TES-F doped with 5% C_{60} compared with the pristine material (Figure 4.8). This is seen more clearly in Figure 4.7.

It may be seen from Figure 4.9(b) that doping with C_{60} shortens the rise time for photoresponse to CW illumination. The results for the analogous experiment with C_{60} in PVK are in reasonably good agreement (Figure 4.9(a)). We were not able to pursue the effects of doping with C_{60} further than 5% since, as mentioned above, the 10% concentration did not allow usable films to be made. Figure 4.6 shows, with respect to the other dopants, that ADT-TIPS-CN acts to enhance the dark current, and the other two dopants act to reduce it, Pc-TIPS the most, DCDHF the least. Figure 4.8 indicates

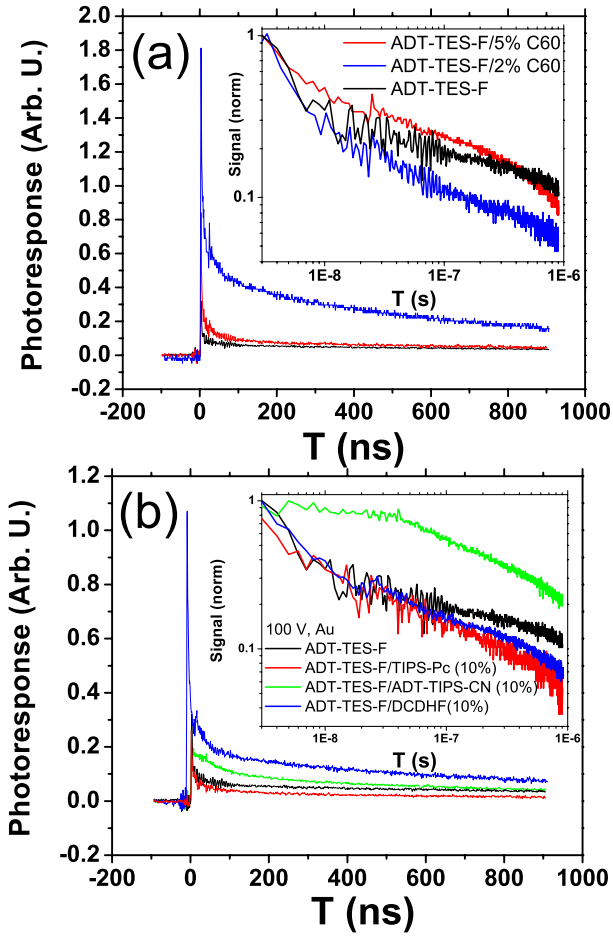

Figure 4.3. (a) Transient photoresponse of ADT–TES–F films, pristine and doped with 2%, 5% C_{60}. Inset: Logarithmic plot of transient photoresponse (b) (a) Transient photoresponse of ADT–TES–F films, pristine and doped with 10% DCDHF, Pc-TIPS, and ADT-TIPS-CN. Inset: Logarithmic plot of transient photoresponse .

that the effects of these dopants on CW photoresponse with dark current subtracted are more ambigious, varying over the voltage range.

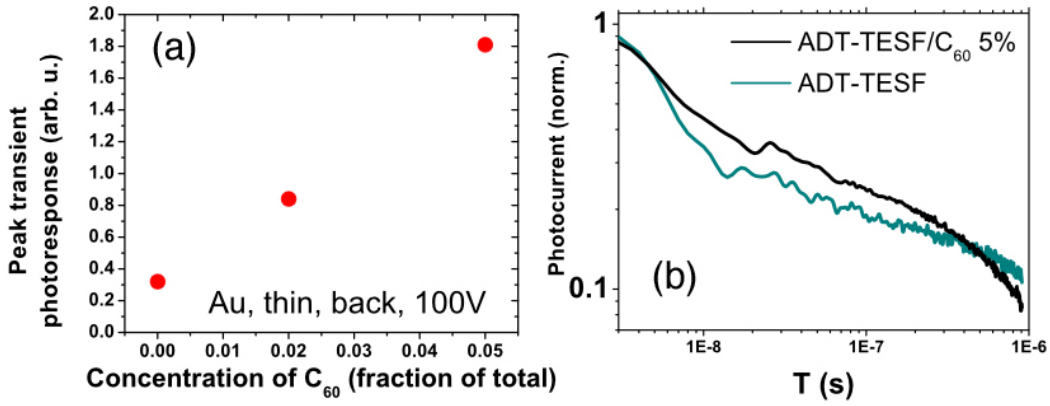

Figure 4.4. (a): Amplitude of peak photoresponse as a function of dopant concentration (percentage by weight of C_{60}). (b): Log-log plot of normalized decay profiles, ADT-TES-F, 5% C_{60} doping vs. pristine ADT-TES-F.

4.5 Discussion

The results confirm that dopants which are electron acceptors in a host material in which holes are the majority carrier act as p-type dopants, increasing conductivity, although not necessarily increasing photoresponse on all time scales. Conversely, dopants which are hole acceptors act as n-type dopants, decreasing conductivity. It is found that not all electron acceptors have the same effect; this will depend not only on the affinity, but upon the degree to which the dopant introduces structural defects into the host material.

4.5.1 Doping with C60

C_{60} acts in polymers and oligoacenes as an electron acceptor, capable of accepting up to six electrons, and forming charge-transfer complexes in the bulk material. When a bulk material such as PPV or ADT-TIPS-F is doped with a small percentage of C_{60}, say 1 – 2%, the photoresponse is generally enhanced. Figure 4.4(a) gives the amplitudes

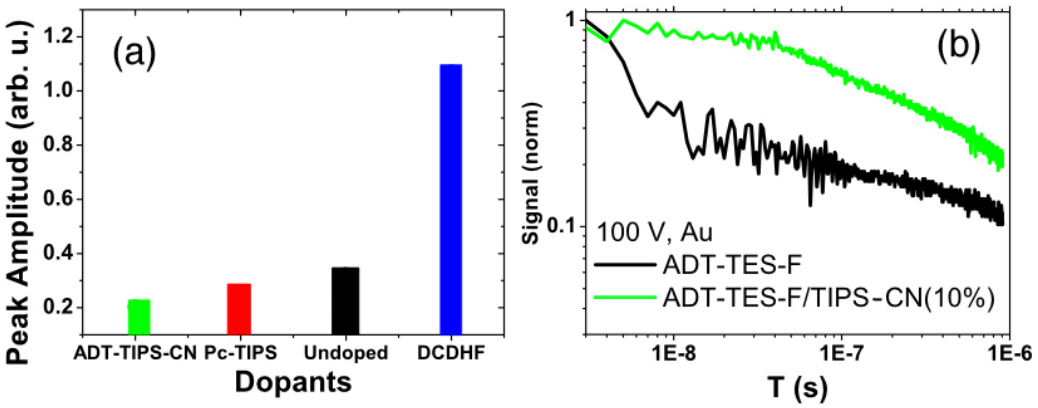

Figure 4.5. (a): Amplitude of peak photoresponse for ADT-TES-F doped with: 10% DCDHF, Pc-TIPS, and ADT-TIPS-CN. (b): Log-log plot of normalized decay profiles, ADT-TES-F with 10% ADT-TIPS-CN doping vs. pristine ADT-TES-F.

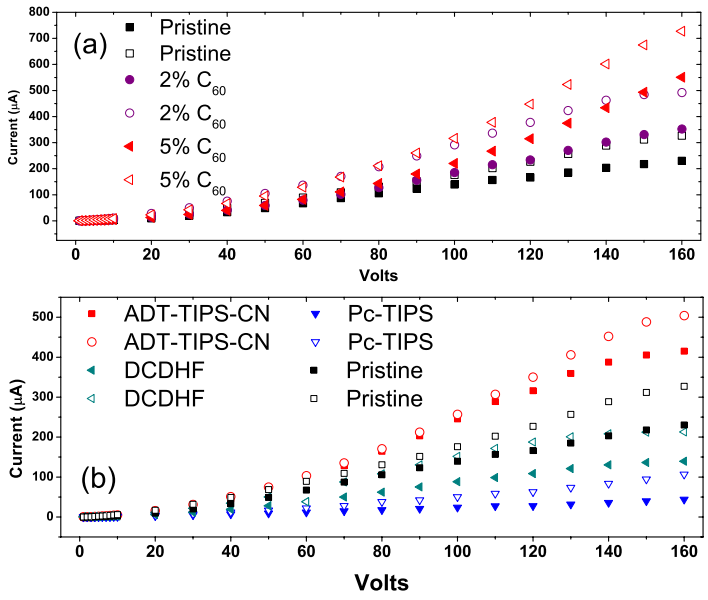

Figure 4.6. (a) Dark current and CW photoresponse for ADT-TES-F, pristine and doped with 2 %, 5 % C_{60} (b) Dark current and CW photoresponse for ADT-TES-F, pristine and doped with ADT-TIPS-CN, Pc-TIPS, and DCDHF. Open symbols: CW, closed symbols: dark current

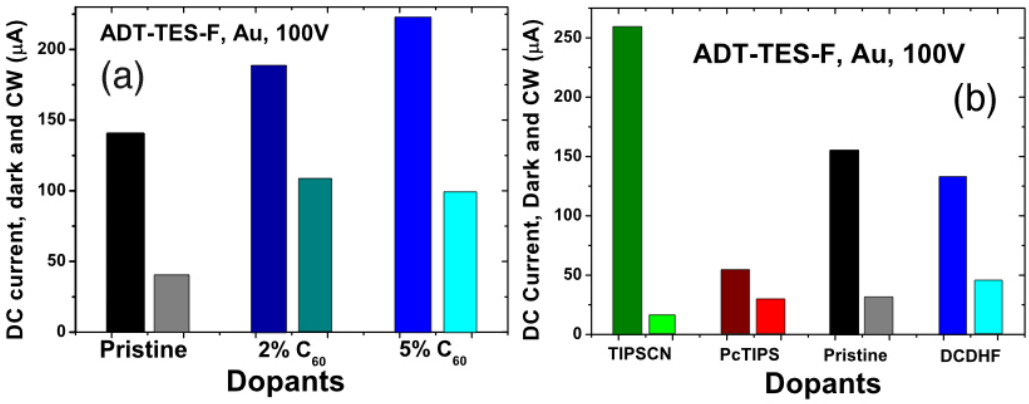

Figure 4.7. (a): Amplitude of dark current and CW photoresponse as a function of dopant concentration, ADT-TES-F doped with C_{60}. (b): Amplitude of dark current and CW photoresponse as a function of dopant concentration, ADT-TES-F doped with Pc-TIPS, ADT-TIPS-CN, DCDHF. For each pair of bars: darker bar represents dark current; lighter bar CW photocurrent.

of the peak photoresponses and of CW photocurrents as a function of the dopant concentration. In view of the variations seen between the films, the exact numerical value of these relations is not significant, but the trend is unmistakeable.

The data in Figures 4.4 taken together with the data in Figure 4.9(b) mean that C_{60} as a dopant in ADT-TES-F acts both to speed photoresponse to CW illumination and to increase its amplitude. But it does not act as an electron acceptor in the same way that ADT-TIPS-CN does. As a dopant in ADT-TES-F, ADT-TIPS-CN seems to be positioned peculiarly well, in terms of the energetics of photoexcitation of this host material at 400 nm, to inhibit the recombination process. ADT-TIPS-CN is structurally similar to ADT-TES-F, which means that if it introduces structural defects, they will be much less severe than those introduced by C_{60}. In terms of Daniel Moses' argument (Section 2.3.3),[49] in which the fast component of the decay is quenched by C_{60} accepting electrons from initially de-localized excited states, and in terms of our view that such delocalization of these states diminishes progressively after the intial excitation, one may

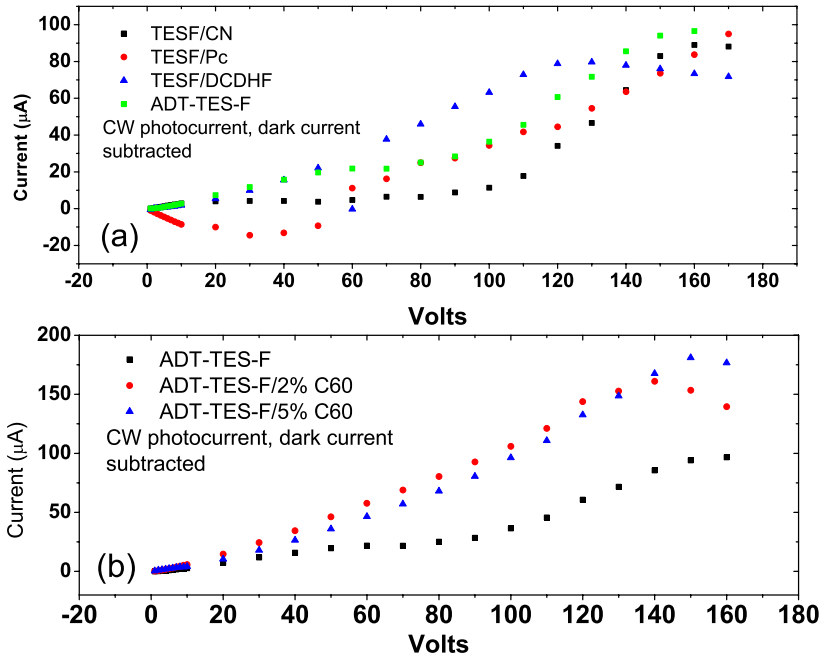

Figure 4.8. (a)ADT-TES-Films doped with Pc-TIPS, ADT-TIPS-CN, and DCDHF, concentrations 10% by weight: CW photocurrent, dark current subtracted. (b)ADT-TES-Films, pristine and doped with C_{60}, 2% and 5% by weight: CW photocurrent, dark current subtracted.

propose the following: In order for C_{60} to accept an excited electron, that electron must first not scatter off the structural defect which that C_{60} has introduced. The transfer of a photoexcited electron to C_{60} is likely to be a much less energetically favorable event than the acceptance of that same electron by an ADT-TIPS-CN dopant molecule. Hence, only the initial, most energetic, excited states will result in a charge transfer to a C_{60} acceptor, together with the resulting increase in carrier density as holes are freed. The C_{60} will enhance the peak amplitude of the photoresponse, but it will diminish the longer-time-scale photocurrents, as carriers relax to less energetic states, and its role as a scatterer begins to predominate over its role as an electron acceptor. As a consequence, the transient photo-response current returns more quickly to dark current levels (although those dark current levels may still be higher than in the undoped material – see below).

The ADT-TIPS-CN dopant molecule, on the other hand, introduces no such structural defect, and less energetic, more localized states will be able to transfer charge to it. Hence its effect on the decay profile will be seen to be that of enhancement, both on short and on long time-scales.

CW and dark current. As is evident from Figures 4.6(a), 4.7(a), and 4.8(b), C_{60} appears to enhance both steady state dark currents and CW photoresponse. This may be understood in terms analogous to those of elementary semiconcuctor physics, in which the introduction of electron-accepting doping (p-type) material acts to increase the density of (mobile) holes. It has been found, in recent work with the star-burst small molecule 1, 3, 5-tris (N, N-bis-(4, 5-methoxyphenyl)-aminophenyl) benzol (TDAPB) that C_{60} acts as a p-type dopant in the hole transport layer in that material, resulting in an almost order-of-magnitude increase in hole mobility.[124] This is similar to with what we observe for transients with the 5% doping concentration, albeit in a very different material.

The effect of C_{60} on CW photocurrent may be understood in the same way. Photoexcitation generates mobile carriers and an increase in hole-density. But hole conductivity is greater in p-doped material, hence one naturally observes higher photocurrents in the p-doped material, which is, in this case, ADT-TES-F with C_{60} acting a a p-type dopants. In contrast, ADT-TIPS-CN seems to behave as a p-type dopant for dark current (Figure 4.6) but not for CW photocurrent (Figure 4.8). In general, the role of the molecular dopants, other than C_{60}, either in enhancing or in diminishing CW photocurrent in this experiment is not clear.

DC transients. As noted above, the DC transients indicate a somewhat faster response to CW photoexcitation for ADT-TES-F films doped with C_{60} (Figure 4.9(b)). This is to be expected, if C_{60} is playing on longer time scales the same role of an electron acceptor which it plays in transient photocurrents. The effect of C_{60} in this context is similar to its effect when it is used to dope PVK (Figure 4.9(a)).

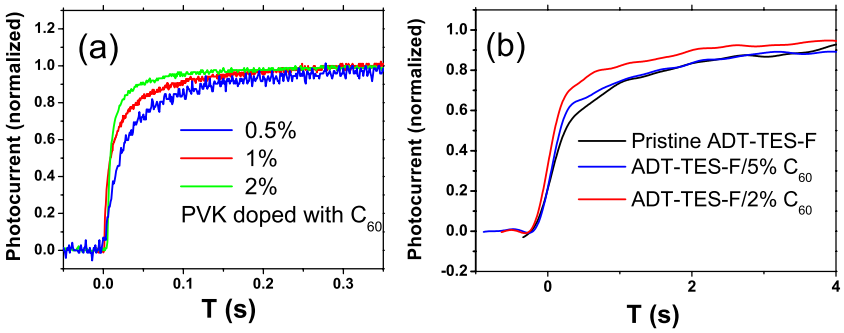

Figure 4.9. (a) DC transients, PVK, doped with C_{60}, 0.5%, 1%, and 2% by weight. (b) DC transients, ADT-TES-F, doped with C_{60}, pristine, 2%, 5% by weight.

4.5.2 Doping with related molecules and with DCDHF

The purpose, in the context of these experiments, of doping the organic matrix with molecules of similar structure but different ionization potentials and electron affinities is the controlled introduction of a specific density of sites with known differences in electron affinity or ionization potential from the bulk material. The relative energies of the HOMO levels of ADT-TES-F and the molecular dopants used are shown in Figure 4.10.

The bandgaps for all these materials (except DCDHF) are close to the same value, approximately 2 eV. This means, for example, that the LUMO level for ADT-TIPS-CN will be approximately 0.2 eV below that of ADT-TES-F, i.e., its electron affinity is 0.2 eV greater. A site where an ADT-TIPS-CN molecule is present will tend therefore to act as an electron acceptor.

Transients. As mentioned above, the effect of doping ADT-TES-F with ADT-TIPS-CN (10% by weight) is dramatic. The difference between the photoresponse of the thin film doped with ADT-TIPS-CN and the films doped with the other molecular dopants, or the pristine film, is seen most clearly in Figure 4.5(b). During the first $\sim$ 50 nanoseconds after the peak, the decay is very gradual, compared with all the other

films. There is an actual knee in the decay curve at around 40 - 50 ns after the peak, at which point the decay rate steepens, and begins to resemble that of the other films.

The overall effect is in some ways very similar to that described by Moses[42] and discussed in Chapter 2, Section 2.3.2 (see figure 2.4). In that case, MEH-PPV was doped with C_{60} and data was taken for photo-induced absorption as a function of time, using pump-probe methods (Chapter 1, Sec. 1.4.3). In this method, the pump-beam induces photoexcitation; if an acceptor such as C_{60} is present, the excited electron is taken up by the acceptor, and the hole is left behind at the donor site, resulting in a charge-separated state. Such a state improves the quantum efficiency for photogeneration of charge carriers, but decreases the associated absorption, since the charge-separated state is transparent to the probe beam. In the case of a material such as ADT-TES-F, in which the majority carrier is holes, the hole left behind can become a free carrier. Since the rapid component of the transient decay is almost completely quenched by the presence of the ADT-TIPS-CN, this suggests that this dopant is playing a very similar role to that played by C_{60} in MEH-PPV. That is, when excitations are induced by the ultrafast laser pulse, rather than e-h pairs quickly recombining, the electrons are taken up by the electron traps or acceptors formed by the ADT-TES-CN molecules, and the holes become free carriers, whose lifetime, before trapping or recombination, is greatly increased. (Recall that this model for decay quenching implies a certain degree of delocalization of the initial excitation.) Since it is difficult to see how doping with ADT-TIPS-N could greatly reduce the density of deep traps, this suggests, if the above analysis is correct, that recombination may in fact play a role in fast decay equal to that played by deep trapping.

The $\sim$50 ns delay after the peak, before the decay rate of the film doped with ADT-TIPS-CN begins to resemble that of the other films, is suggestive. If the above view is correct, then this gives us a good estimate of how long the electrons accepted by the ADT-TIPS-CN molecules remain‘trapped. Prior to the knee in the decay profile mentioned above, the initial decay in the transient response is quenched by the inhibition of recombination due to the presence of the electron acceptors. But at some point near

40 ns after the peak, perhaps as a result of thermal de-trapping, the number of electrons bound by ADT-TIPS-CN acceptor molecules has diminished, and the carrier density and the degree of carrier delocalization have also diminished, to the point where trapping and recombination processes begin to re-assert themselves, and the decay begins to become steeper, or rather to return to a normal rate.

In this context it is very interesting that C_{60}, as a dopant in ADT-TES-F, appears to play a very different role from that played by ADT-TIPS-CN, or from the role which it plays, itself, in MEH-PPV. This may be seen by comparing Figure 4.2(b) and (c). Figures 4.3 and 4.4 shows that it does act to enhance the amplitude of the transient, but its effects on the actual shape of the curve are ambiguous. Doping with a 5% concentration appears to result in a slower decay; doping with 2% results in a faster decay, but a longer tail (see Figure 4.2(b) and especially Figure 4.3(a), inset). These features of the data are not yet understood.

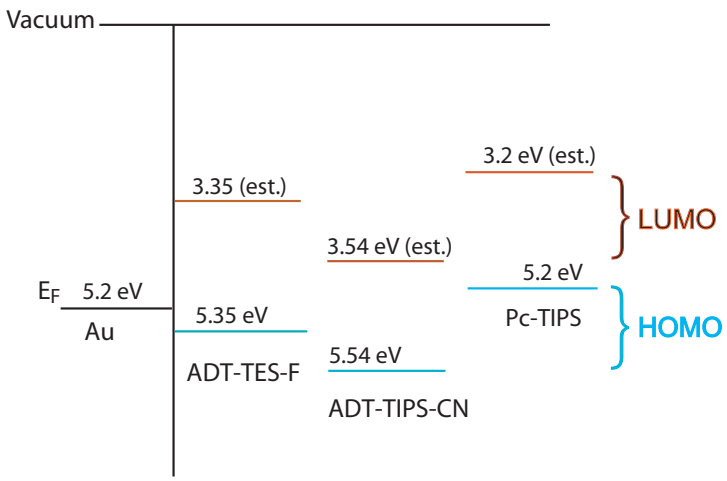

Figure 4.10. Ionization energies for the materials studied in this Chapter. E_F, Fermi energy.

In contrast, if we look at the results of doping ADT-TES-F with one of the other dopants, the principal difference between the decay dynamics of pristine ADT-TES-F, and the same material doped with Pc-TIPS, or DCDHF, is that either of those shorten the tail of the decay profile (Figure 4.3(b), inset), compared with the pristine material. This might suggest that Pc-TIPS and DCDHF are similar with respect to their role in the energy structure of the doped materal. However, in terms of the energy levels shown in Figure 4.10, Pc-TIPS is a hole acceptor, and DCDHF is, like ADT-TIPS-CN, an electron acceptor. This suggests that the first will diminish, the second enhance DC conductivity. But the data shown in Figure 4.6 does not agree with this. Both diminish DC dark current, Pc-TIPS more, DCDHF somewhat less. This is a continuation into long time scales of the comparable roles the two play in shortening the tail of the decay profile (Figure 4.3(b), inset). This action of Pc-TIPS is not surprising, if it is indeed acting as an n-type dopant. The question is, why does not DCDHF, with ionization energy so close to that of ADT-TIPS-CN, play a similar role, enhancing the DC conductivity? The answer may lie in the fact that, unlike ADT-TIPS-CN, DCDHF is strongly polar, in the first place, and introduces structural defects, i.e., scattering sites, in the second place, We are using a fairly large concentration of DCDHF here, 10% by weight. It would not be surprising if, on the one hand, the polarity of this molecule rendered it approximately neutral with respect to the actions of accepting holes or electrons and, on the other hand, its addition of scattering sites made its net effect that of the reduction of DC conductivity, at least on longer time-scales.

However, looking at shorter time-scales, easily the largest of the peak amplitudes is that of the film doped with DCDHF, although the shape of the normalized transient decay curve is very similar to that of the film with Pc-TIPS dopant (Figure 4.3). The effect of doping with DCDHF is somewhat similar to the effect of doping with 5% C_{60}. This suggests that, on very short time scales, the role of DCDHF as a scatterer is less important, similar to the case of C_{60}, and that the molecule in that case functions chiefly as an electron acceptor.

CW and dark current. On the one hand, Figure 4.6(b) indicates that ADT-TIPS-CN enhances, while Pc-TIPS and DCDHF inhibit dark current. On the other hand, CW photocurrent, when dark current is subtracted, is found to be comparable for all three (Figure 4.8(a)), at least at certain voltages. The result for the dark current agrees well with the position of the ionization energy of ADT-TES-F roughly midway between the energies of the others. In general, these results are compatible with the view that ADT-TIPS-CN acts as a p-type dopant, and Pc-TIPS and DCDHF act as n-type dopants. That is to say, if we accept the view that the HOMO and LUMO levels are in some way analogous to the conduction and valence bands of an inorganic semiconductor, then the configuration of energy levels between the bulk material here and the dopant is also analogous. The ADT-TIPS-CN is an electon acceptor, Pc-TIPS and DCDHF are "hole acceptors." In a material in which holes are the majority carrier, electron acceptors will act to increase the mobility, electron donors or "hole acceptors" will decrease it. The results for CW photocurrent with the dark current subtracted are less conclusive. It is not clear why, for example, the CW photocurrent minus the dark current for ADT-TES-F doped with ADT-TIPS-CN should have been nearly zero, up to 100 V, and then climbed steeply.

4.6 Conclusions

The dopants here chosen will serve as either hole acceptors or electron acceptors in ADT-TES-F. C_{60} forms charge-transfer complexes in ADT-TES-F and, in similarity to its behavior in polymers and other materials, enhances conductivity. The results present some suggestive similarities to the known consequences of doping inorganic semiconductors with p-type or n-type dopants.

The results also shed further light on the dynamics of carrier recombination and trapping, and the way in which the nature of the carrier develops over time after its initial photogeneration. For example, if ionization energy were the sole, governing parameter, it would be expected that the effects of doping ADT-TES-F with ADT-TIPS-CN and DCDHF would be very similar. However, on short time scales ADT-TIPS-CN

acts as an electron acceptor and a strong inhibitor of recombination. DCDHF, on the other hand, appears to act as an even stronger electron acceptor but has no marked effect in slowing recombination. This may be tied to the difference in the degree to which these two may introduce structural defects, so that whereas DCDHF, like C_{60}, will introduce scattering sites, ADT-TIPS-CN will do so to a much smaller degree. Hence the role of DCDHF and C_{60} in transient photoresponses will tend to be more restricted to the times immediately after the initial photoexcitation, when carriers are more delocalized and less likely to scatter from defects. In contrast, ADT-TIPS-CN will tend to act more like a p-type donor in a p-type semiconductor, enhancing photoconductivity on both short and long time-scales, whether carriers are less or more localized. Similarly, Pc-TIPS, which in ADT-TES-F is equivalent to an n-type dopant, serves to diminish conductivity on time scales greater than $\sim$500 nanoseconds.

On the Photoresponse of Several Novel Functionalized Oligoacene
and Anthradithiophene Derivatives

CHAPTER 5
CONTACT EFFECTS

5.1 Introduction

The organic materials discussed in this study, if they are to be of practical use, must be integrated into systems in which they will almost certainly interface with inorganic materials, often metals. Hence questions pertaining to the physics of such interfaces are of great interest, for reasons germane to both theory and practice. We must be able to distinguish the part played by carrier dynamics in bulk material from that played by interface dynamics, so that the separate contribution of each to the behavior of the overall system may be understood. Such questions are by no means fully answered at the present time.

Described in this chapter are experiments performed with two very similar materials, ADT-TES-F and ADT-TIPS-F, primarily with the latter. Films of these materials were prepared on substrates pre-patterned with gold and on substrates pre-patterned with aluminum electrode pairs, both interdigitated and simple coplanar. The details for sample preparation are the same as given in Chapter 3. Data for dark currents, CW photoresponse and transient photoresponse were taken, allowing us to compare the different behaviors of films of the same material prepared with the different metal contacts. From this some important characteristics of the interfaces of the organic materials with the two metals may be deduced, and some conclusions drawn regarding the overall effect of these characteristics on device performance.

5.2 Materials

One of the materials used in this portion of this study was among the group discussed in the previous chapter, that is, the novel high performance fluorinated anthradithiophene derivative ADT–TIPS–F, functionalized with triisoproplysilylethynyl (TIPS) side-groups,[2] (Fig. 5.1 (a)). As described before, ADT–TIPS–F exhibits brick-wall-type crystal packing, with significant π-overlap,[2,80] favoring high TFT mobility.[24] It forms polycrystalline films[9] when deposited from solution, with the a-b plane in the plane of the film. The other material was a very similar molecule, ADT-TES-F, the same in every respect as ADT-TIPS-F, except functionalized with triethylsilylethynyl (TES) side groups.

Glass substrates were prepared by photolithographic deposition of 100-nm-thick aluminum (Al) and 50-nm-thick gold (Au) electrode pairs (Figure 3.3), by Charles Ellis of Auburn University. Pairs were fabricated in two different configurations, the first consisting of 10 interdigitated finger-pairs, with 1 mm finger length, 25 μm finger width and 25 μm gaps between the fingers of opposite electrodes, the second consisting of 6 finger-pairs, with the same length and spacing, but with 50 μm finger width. Both configurations resulted in the same total active (interdigitated) area, 1 mm^2. ADT–TIPS–F polycrystalline films with thicknesses of 0.5 – 2 μm were drop-cast from toluene solution onto these substrates at $\sim 60^\circ$C. At least five samples on each metal type and configuration of electrodes were prepared. A typical optical absorption spectrum is shown in Fig. 5.1(a).

5.3 Experiments and Results

Observations of the photoresponses of thin films of ADT-TIPS-F and ADT-TES-F with aluminum and with gold contacts, on time-scales from nanoseconds to seconds (as well as dark currents) show that the role of the contact metal is crucial in shaping the photoresponse and dark current. But that role takes very different forms at the two ends of the time-scale used in this experiment. On short time scales, those of measurements

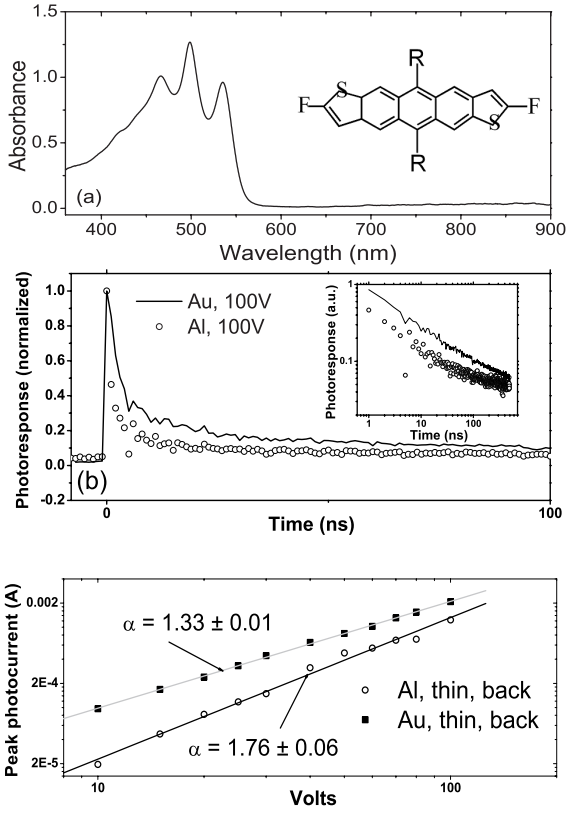

Figure 5.1. (a) Molecular structure (R = Si(i-Pr)$_3$ (ADT-TIPS-F), R = Si(Et)$_3$ (ADT-TES-F)), and optical absorption spectra of ADT–TIPS–F films. (b) Transient photocurrent obtained in ADT–TIPS–F films, on Au and Al electrodes, at 1.2×10^4 V/cm and 30 μJ/cm^2 at 400 nm. Inset: Transient photocurrents (I_{ph}) in ADT–TIPS–F films on loglog scales. (c) Transient photoresponse peak amplitudes vs. voltage, for Au and Al electrodes, thin fingers, back illumination.

of transient photoresponse, films with the two different contacts do not exhibit great differences in behavior, either with respect to the amplitude of the signal or the shape of the response curve (Figure 5.1(b) and (c)). On longer time-scales the differences become much more pronounced. Data for dark current and CW photoresponse (Figures 5.4 and 5.5), show marked differences in both the amplitudes of the currents and in the functional relations between currents and applied voltage. These differences are clear indications of the importance, for overall device performance, of the physics at the organic/metal interface. This is discussed in detail in what follows.

5.3.1 Transient and CW photoresponse measurements

For transient photoconductivity measurements, an amplified Ti:Sapphire laser (800 nm, 100 fs, 1 kHz) was used in conjunction with a frequency-doubling BBO crystal to excite the samples at 400 nm wavelength. Fluences in the 10-100 μJ/cm^2 range were used. Voltage was supplied by a Keithley 237 source-measure unit, and laser-pulse-induced transient photocurrent was measured with a 50 Ω load by a 50-GHz CSA8200 digital sampling oscilloscope (DSO). The configuration of instrumentation was the same as that described in Chapter 3, Section 3.1.3, Figure 3.4. Samples were placed in the same fixture described in that chapter. Photoresponse magnitudes were read out from the sample fixture as voltages across the input impedance of the DSO.

In the CW photoconductivity measurements, the sample was excited by a Nd:YVO_4 laser at the wavelength of 532 nm. The Keithley 237 source-measure unit was used to measure dark and CW photocurrent by performing linear stair voltage sweeps, from 0 to a maximum of 300 Volts. The overall setup was the same as shown in Figure 3.5. Dwell times at each voltage in the linear voltage sweeps were varied between 0.2 seconds and 10 seconds. Both dark and cw photocurrent sweeps were done in the same way. The light intensities for the CW photocurrent experiments were relatively low, approximately 1 to 5 mW/cm^2.

Transient photoresponse was measured primarily with samples illuminated from the glass substrate side. This serves to put the organic film in the shade cast by the electrodes, as a means of minimizing photoinjection and photoemission effects at the organic/electrode interface. Data was also taken with illumination from the electrode side and compared with data taken from the glass side, to determine the result of maximizing such effects.

5.3.2 Transient photoresponse data

The peak transient amplitudes for films on Au and films on Al electrodes were typically of the same or nearly the same order of magnitude (Figs. 5.1 and 5.3). The

relative differences in these amplitudes were of the same order as differences observed in all of our experiments due simply to film-to-film variations. The relation between peak amplitude and voltage is linear to superlinear (Fig. 5.1(c)) for Au, sub-quadratic to quadratic for Al.

Both these experiments and those described in the previous chapter indicated that the initial decay of the transient is faster for films on aluminum electrodes than it is for those on gold. In general, however, it must be said that the transient responses for films on the two different contact metals are similar, with respect both to amplitude and to the general profile of the transient decay.

5.3.3 Geometry differences. Back illumination versus front.

As mentioned above, substrates were pre-patterned, for both contact metals, with two different interdigitated geometries, one with fingers 25 μm wide, the other with fingers 50 μm wide. These will be referred to as "thin" and "wide" fingers. The amplitudes of the peak photoresponses with thin fingers were greater with gold contacts, for both front and back illumination (Figure 5.3(a)). In general, one would expect greater photoresponse for thin fingers, for either contact metal, inasmuch as the gap between the electrodes is longer, with a greater volume of illuminated sample. The corresponding difference, for thin fingers and wide, was indeterminate with aluminum contacts (Figure 5.3(b)). This is probably due to differences in film morphology between the different samples. (In general, the films on gold contacts seemed to be less subject to variations in behavior due to varying morphologies. It is not known why this should be the case.) Transient amplitudes for back illumination tended to be somewhat greater, with both gold and aluminum contacts. This will be discussed in Section 5.4.6.

For the most part, the relation between peak transient amplitude and voltage is consistent across the sample set, for both contact metals. One finds a power-law relation, $I \propto V^{\alpha}$, with α between 1 and 1.5. The exception is one aluminum sample in the lower voltage range, where $\alpha \sim 2$ (Figure 5.3(b)). Several causes may contribute to this case. It may be due either to a peculiarity in the morphology of that particular

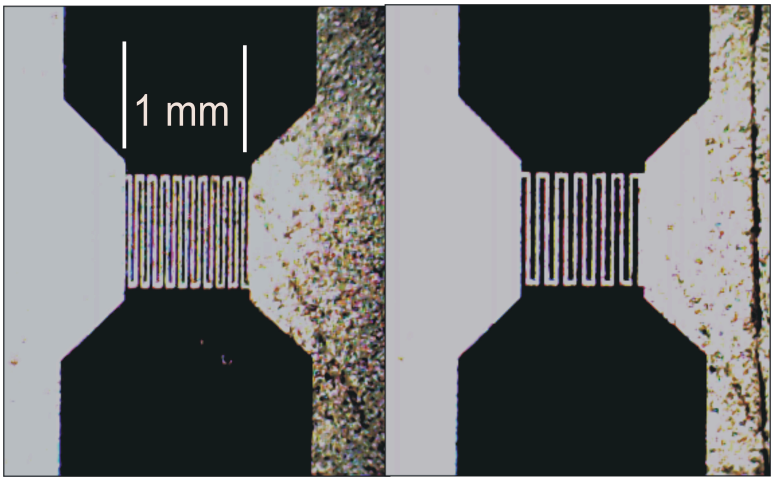

Figure 5.2. Interdigitated electrode pair geometry, showing geometry using "thin" fingers and geometry using "wide" fingers.

film, or perhaps to a peculiarity in the molecular interface between the bulk material and the aluminum contact. The results of Chapter 4 suggest that it is the latter.

5.3.4 Dark current and cw photocurrent

Unlike the transient amplitudes, the amplitudes of CW photocurrents for films on Au and on Al are not similar, but differ rather by at least an order of magnitude. Figure 5.4 shows one form of this difference, at voltages an order of magnitude either way from 10 V. Figure 5.5 shows another aspect of this difference, manifest at the higher voltages (130 -300 V).

The dark current data for films on aluminum electrodes given in Figure 5.4(a) is rather noisy at low voltages, but if one performs linear fits to the data on a log-log plot, one obtains a relation in the form of $I \sim V^{\alpha}$ between current and voltage, with an apparent transition at around 7 volts from value of α to another, particularly in the plot for CW photoresponse. The relation may change from linear to more than cubic (again, depending on film quality and morphology). The plots for a similar sample with gold electrodes (Figure 5.4(b)) show no such transition, but are rather gently concave upward.

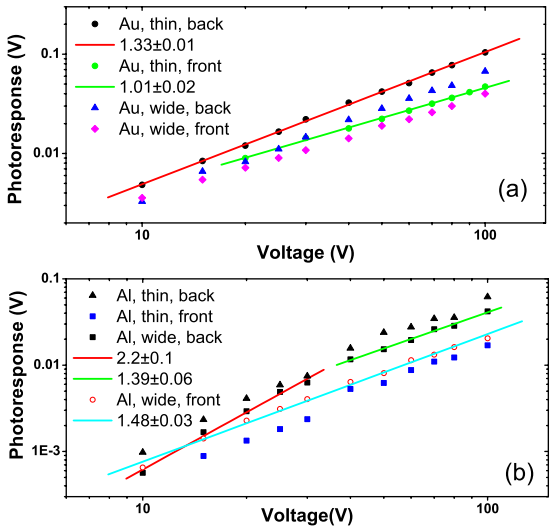

Figure 5.3. ADT-TIPS-F thin films, amplitude of peak transient photoresponse as a function of applied voltage. (a) Au contacts, both thin and wide fingers. (b) Al contacts, both thin and wide fingers.

Below the transition (with aluminum contacts), the voltage dependence of both dark current and cw photocurrent are sublinear to linear. Above the transition, for the case shown, the two dependencies diverge: the dark current varies quadratically with voltage; the cw photocurrent varies cubically. It should be mentioned here that substantial variation in these exponents has been observed. The divergence is not always so great. But for a given film, in general the power-law exponents for dark-current versus voltage will be steeper than that for CW versus voltage, in the case of films on aluminum contacts.

In contrast, no such divergence is seen in the comparable plots for samples with gold electrodes (Figure 5.4(b)). If one fits the data for gold electrodes to a power law, one finds that above approximately 10 Volts, the typical relation between cw photocurrent and voltage for gold electrodes is $I_{CW} \sim V^{1.7}$. The power-law exponents for dark currents tend to be very slightly smaller. It will be seen below, however (Sec. 5.4.3),

that the power-law fit is in any case not the best for dark currents and CW photoresponse in films on gold electrodes.

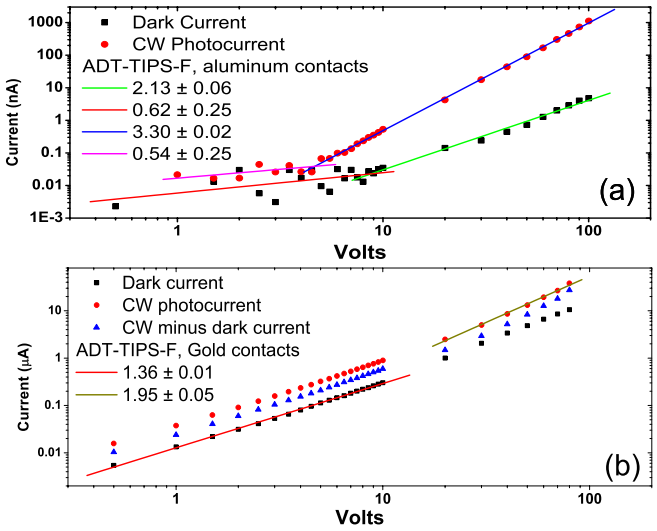

Figure 5.4. (a) ADT-TIPS-F films with aluminum contacts. Dark current and CW photocurrent. CW photocurrent minus dark current not shown; coincides on this scale with CW photocurrent. Voltage 0 – 100V. (b)ADT-TIPS-F films with gold contacts. Dark current, CW photocurrent and CW photcurrent minus dark current, voltage 0 – 100V.

In Figure 5.5, dark currents, CW currents, and CW currents with dark current subtracted, for ADT-TES-F films on aluminum and gold electrodes, are plotted against voltage (10 – 300 V). This plot exhibits some features not seen in Figure 5.4. Most strikingly, the plot for films with aluminum contacts shows a transition, between 150 and 200 V, to a much steeper dependence of amplitude on voltage. The transition occurs at a lower voltage for CW than for dark current. At the highest voltages in the range, the current appears to be leveling off, in this case at around 100 μA for CW. The divergence in the power law exponents for the lower–voltage range is present, although not as great as in the previous figure, for ADT-TIPS-F films. In contrast, the plot for the same currents in films on gold contacts shows no transition and no divergence. However it does show a similar, but more pronounced leveling off at the higher end

of the voltage range, in fact a drop in CW photocurrent if dark current is subtracted. Also, while the power-law fit for the films on gold is reasonably good (Fig. 5.5), if one looks closely one can see that these plots are, again, gently concave upward for voltages below the point where the currents begin to level off. These features will be discussed in detail in Sections 5.4.2 and 5.4.3.

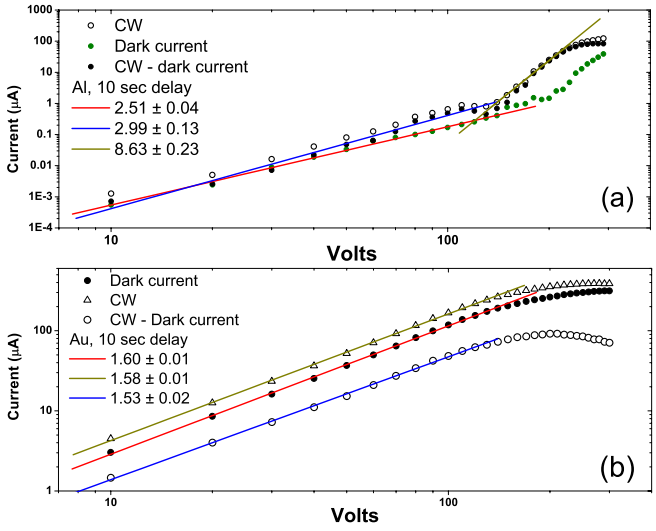

Figure 5.5. (a) ADT-TES-F films with aluminum contacts. Dark current, CW photocurrent and CW photcurrent minus dark current, voltage 10 – 300V. (b)ADT-TESS-F films with gold contacts. Dark current, CW photocurrent and CW photcurrent minus dark current, voltage 10 – 300V.

5.3.5 Gap Scan: Photoresponse

In order to begin to map the variations in potential, electric-field strength, space-charge density, and other parameters across the gap between electrodes, an experiment was designed to measure the intensity of the photoresponse as a small beam spot was moved across the gap from one electrode to another. Glass substrates were prepared by photolithographic deposition of simple (not interdigitated) coplanar aluminum and gold electrode layers (Figure 5.6). The gap between the electrodes was 50 μm. A laser beam

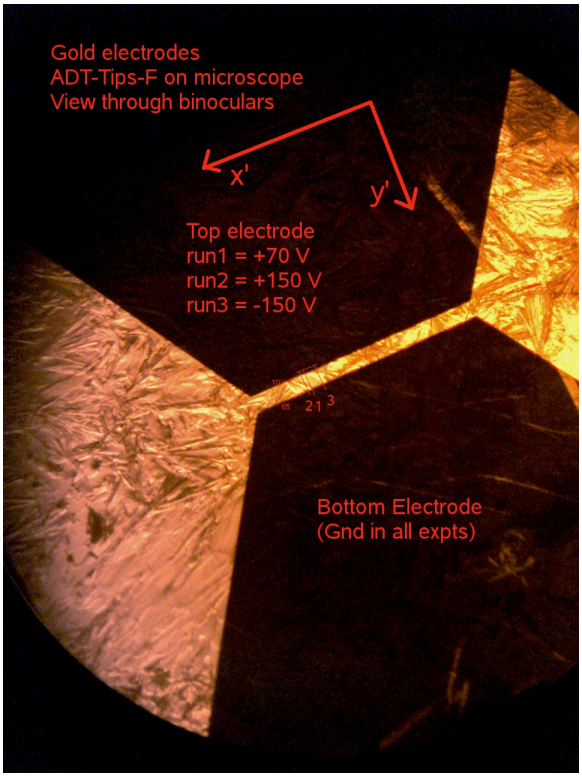

Figure 5.6. Microsope view of coplanar electrode pair used for measurement of phoresponse as function of beam spot position in gap.

with a wavelength of 532 nm was focussed into a spot in this gap approximately 1 μm in diameter. The spot traversed the gap, moving from the negative electrode towards the positive, under control of LabView software (Figure 5.7), while being chopped at 565 Hz. The modulated photocurrent signal was detected by an SRS 830 lock-in amplifier. The resulting photoresponse as a function of position in the gap is shown in Figure 5.7(b), for gold and for aluminum electrodes. It may be seen that both gold and aluminum electrode pairs show a marked peak in photoresponse, for excitation near the negative electrode. For aluminum electrodes, the amplitude of this peak response, near the positive electrode edge, is three and one-half orders of magnitude greater than the response in mid-gap, while for gold electrodes, the difference is perhaps only an order of magnitude, largely due to a much greater response to illumination in the mid-gap region. This will be discussed further below.

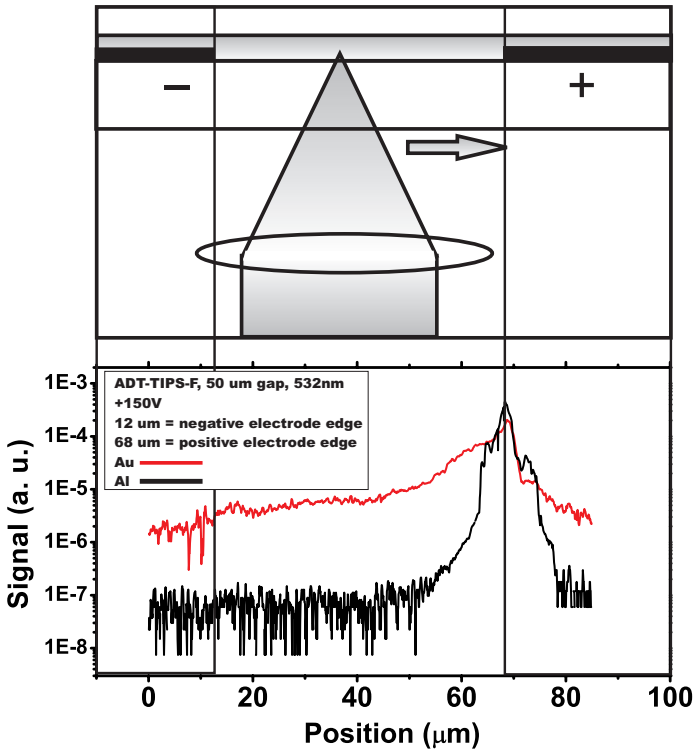

Figure 5.7. Top: Schematic of scan of coplanar gap. Bottom: photoresponse as function of position of beam spot in gap, for gold and for aluminum contacts.

In Figure 5.8 are shown, for gold contacts, the results of three similar scans with different voltages across the gap. The photocurrent response for mid-gap illumination is linear with voltage, but is quadratic with voltage for illumination near the positive electrode. Currents with aluminum electrodes were too small to allow similar data to be taken for films with those electrodes, but the profiles given in the bottom of Figure 5.7 suggest that the variation with applied voltage of response to illumination near the positive electrode would have been even steeper, perhaps cubic or higher. Data not here presented indicates that while these contours for photoresponse as a function of spot position do vary with applied voltage, they do not vary significantly with beam intensity. This indicates that photo-injected carriers do not contribute to any significant change in the space-charge profile within the greater part of the gap, and therefore the

profiles given in these figures may be taken to map fairly closely the contours of E-field strength.

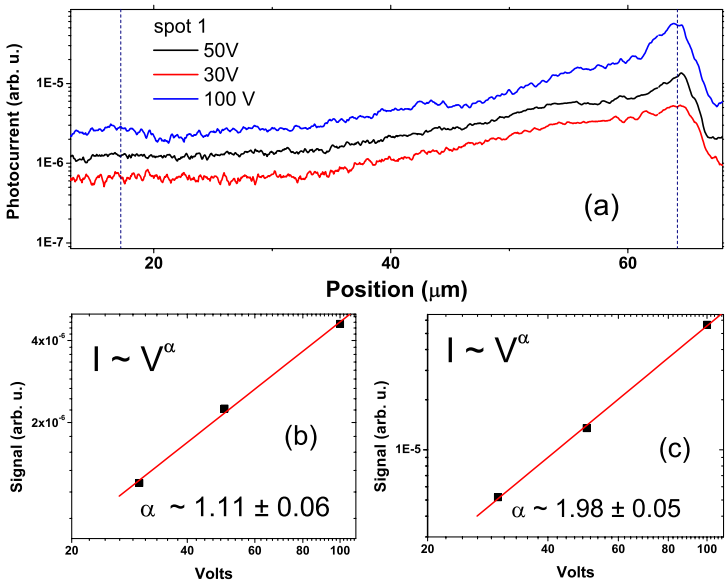

Figure 5.8. (a) Gap: photoresponse to localized beam spot, as a function of spot position in gap, for 30, 50, and 100 V. Vertical dashed lines show positions of electrode edges, positive at 70 μm. (b) Power-law relation $I \propto V^{\alpha}$, showing linear relation with beam spot at mid-gap. (c) Quadratic relation for beam-spot near positive electrode edge.

5.3.6 Gap scan: Transients

Data was also taken for transient photoresponse with the beam localized to a small spot within the coplanar gap, approximately 4 microns in diameter. The beam was focused to a small waist by a 25 mm lens which was mounted on a micrometer translation stage, and the spot was then made to traverse the gap manually by making small adjustments of the micrometer. However, the signal-to-noise ratio for this measurement is not good, since the signals from the simple coplanar electrode pair (Figure 5.6) tend to be weak. For each type of contact metal, the results were inconclusive with respect

to any differences in the shape of the transient which might result from changing the position of the beam spot within the gap. The results did confirm, however, that the transients in general decay more quickly in films with aluminum electrodes than with gold.

5.4 Discussion

The evidence presented here confirms that differences in contact metals lead to differences in the physics at the organic/metal interface, which in turn play an important role in the different transport behaviors of films on gold and on aluminum electrodes, especially in the CW and dark current regimes, where the difference in current magnitude for films on the two metals can be several orders of magnitude, and where the relation between current and voltage is qualitatively quite different. The discussion here will focus on three main areas. First, there is the question of the relative roles played by injection-limited versus bulk-limited currents in the cases of the two different contact metals. Second, there is the question of the particular effect an injection-limited current has on the space-charge distribution in the gap between the electrodes, and on the physics of current-injection and current-extraction at the interfaces between the electrodes and the bulk material in the gap. Third, a model is proposed, in the case of the injection-limited currents in the film with the aluminum contacts, for a transition between one charge-injection mode and another, as applied voltage is increased past a certain point.

5.4.1 Space charge in electrode gap

To account for what is seen in figure 5.7 (b), we suggest the following, similar to a model proposed by Agostinelli *et al*,[111] and supported by simulations done by Hurd and McKinnon in 1993.[114] If the bulk material between the electrodes should have a higher density of electron traps, particularly deep traps, than of hole traps, then electrons injected from the negative electrode will tend to be trapped in the bulk material, building

up a negative space charge density in the region between the electrodes, and screening the negative electrode. The potential gradient at the interface between the negative electrode and the bulk material will become flatter, while the gradient at the interface with the negative electrode will be made steeper. The potential gradient near the positive electrode will be in effect that of the applied potential over, not the gap width L, but over a much narrower L*. Consequently, field-induced photocurrent is more likely to be generated near the positive electrode edge. We see this in Figure 5.7 for both aluminum and gold electrodes. The plot of photoresponse versus position may thus be taken as an approximate map of the E-field profile across the gap. It is noteworthy that the peak photoresponses for both are of the same order of magnitude.

In the case of aluminum electrodes, there is the additional factor of the very high resistance to current flow through the oxide layers. At room temperature, aluminum self-anodizes to form an oxide layer 2 to 3 nm thick.[108] Charge may tunnel through this layer, since the tunneling range for aluminum oxide films is < 10 nm.[109] Or it may move through the layer by hopping.[110] In either case, the effective resistance to current flow is very high. That the peak for photoresponse in Figure 5.7 for aluminum is comparable to that for gold suggests that the E-field gradient at the edge of the aluminum negative electrode is much steeper than it is for gold electrodes, as it must be to transport a comparable current against the resistance of the oxide layer. This in turn suggests that the space-charge accumulation in the gap is much greater for the aluminum electrode pair. This may be explained by supposing that de-trapping from both deep and shallow traps in the gap area is inhibited, in comparison with gold, by the high resistance of the oxide layer, allowing a greater accumulation of trapped charge, i.e., space charge, in the gap.

The power-law dependence of both dark and CW currents on voltage tends to be steeper with aluminum electrodes than with gold ($I \propto V^{\alpha}$, $\alpha > 2$ for dark current, $\alpha > 3$ for CW current, versus $\alpha = 1$ to 2 for gold). The work functions from standard references, for aluminum with native oxide, and for gold, are 3.9 and 5.2 - 5.4 eV respectively.[112] The injection barrier for holes between gold and ADT-TIPS-F, with

an ionization energy of 5.35 eV, is then much lower than that between aluminum and ADT-TIPS-F. Theoretical work by Arkhipov *et al*[113] indicates that an increase in the size of the injection barrier should result in a steeper dependence of current on electric field, which is what we observe.

5.4.2 Aluminum Contacts

Schottky barrier, injection-limited dark current. The exact nature of the physics at the interface has been an ongoing topic of investigation in recent years. Work with MEH-PPV, Alq_3, and other organic materials has suggested modifications to the Schottky band-bending model.[116,117] Other models have been proposed with no band-bending, particularly in disordered materials.[118] The notion of band-bending, after all, presupposes a material in which carriers are relatively free to move and to seek thermodynamic equilibrium under the influence of various internal and external potentials. Materials bound by Van der Waals forces, with carriers in localized states, may not behave in that fashion, and in many cases almost certainly do not.[116,117]

As a starting point, nevertheless, we may model an ADT-TES-F film between two metal contacts as an anode-to-anode, Schottky diode structure (Figure 5.9(a)), with band-bending. To the extent, then, that the Schottky barriers limit current, the I-V relation of the whole device will be essentially that of that junction which is reverse-biased. A closer view of this junction is given in Figure 5.9(b). An important feature of this model is the Schottky effect, in which the injection barrier height for injection of holes from the positive electrode, for example, is lowered due to an image-charge potential seen by any hole which has been ejected from the electrode.

If this general characterization is valid, there remains the question, how is the charge transported across the Schottky barrier? Is it primarily thermionic, or tunneling? On the one hand, work with MEH-PPV and a variety of anode metals supports the position that bands are not bent in such systems, and carrier injection is via tunneling.[116] The Fowler-Nordheim equation gives the current I through a tunneling barrier as

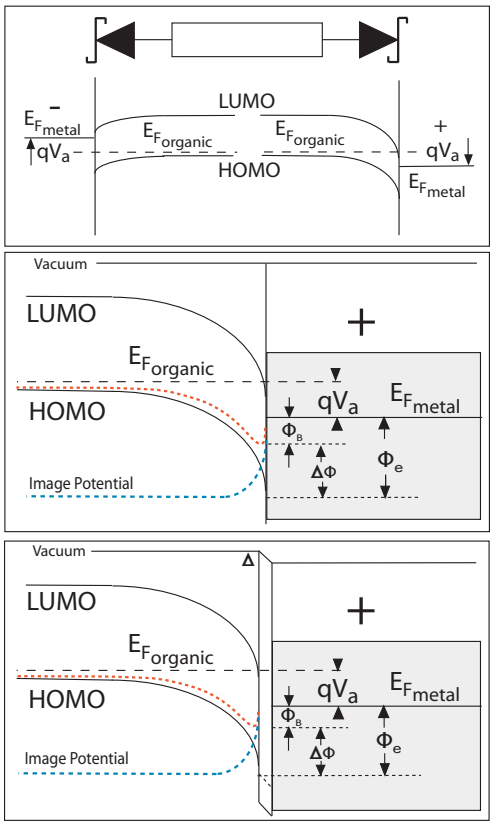

Figure 5.9. (a) Schottky anode-to-anode structure. (b) Detail at reverse-biased junction, showing reduction of barrier size from Φ_e to $\Phi_B = \Phi_e - \Delta\Phi$ due to Schottky effect. The effective barrier potential, due to the superposition of the image potential on the HOMO level, is shown as a red dashed line. (c) Detail, showing further reduction in magnitude of the injection barrier Φ_B due to interface dipole and resulting vacuum level shift Δ.

$$I \propto F^2 exp(\frac{\kappa}{F}), \tag{5.1}$$

where the constant κ is

$$\kappa = \frac{8\pi\sqrt{2m^*}\Phi_B^{3/2}}{3qh}. \tag{5.2}$$

Here F is the field strength, m* is the effective carrier mass, and Φ_B is the barrier height. Dividing Equation 5.1 through by F^2 and taking the natural logarithm of both sides yields

$$ln(\frac{I}{F^2}) = -\kappa(\frac{1}{F}). \tag{5.3}$$

If $\ln(I/F^2)$ is plotted against $1/F$, the result is termed a Fowler-Nordheim plot. When such a plot reveals a linear relation of I/F^2 to $1/F$, this is an indication of injection via tunneling.[115] Obtaining the slope κ of that relation, one may deduce from Equation 5.2 a value for the barrier height Φ_B.

On the other hand, the dark current data may be also fitted to the Richardson equation for injection via thermionic emission:

$$j = (4\pi m_e^* e\frac{k^2}{h^3})T^2 e^{-\frac{\Phi_B}{kT}}, \tag{5.4}$$

where Φ_B is the injection barrier height incorporating the Schottky effect, h is Planck's constant, k the Boltzmann constant, T the device temperature, and m_e^* is the effective carrier mass. Here the Schottky barrier height Φ_B is

$$\Phi_B = \Phi_e - \Delta\Phi, \tag{5.5}$$

where Φ_e is the barrier height for hole injection (the difference between the metal work function and the organic ionization energy), L* is the effective gap width due to the negative space charge build-up described above, and

$$\Delta\Phi = \sqrt{\frac{e^3 V}{4\pi\epsilon\epsilon_0 L^*}} \tag{5.6}$$

is the reduction in the injection barrier height due to the Schottky effect,

Dark current data was fitted to the Richardson equation with the following variable parameters: the effective gap width L*, the effective mass m*, and the activation energy Φ_e. Φ_e was allowed to be a variable parameter as a means of testing the general validity of the fit. The actual values expected for Φ_e are 1.4 eV for ADT-TIPS-F on self-anodized aluminum contacts, 5.35 - 5.4 = -0.05 $\sim$ 0 eV for gold contacts. This value for the gold contacts would seem to be no barrier at all, and hence we would not expect the Richardson equation to fit the data for gold contacts well. We will see below that it does not. (The data for the photoresponse as a function of beam spot position in the electrode gap (Section 5.3.5) suggests that the injection barrier at the gold electrodes may be low, but it is not in fact zero.) The effective gap width L*, while allowed to vary from fit to fit, was assumed to be a constant in any given fit. This is probably not quite true in reality, but over a relatively small voltage range such as ours, it may be taken to be a good approximation.[114]

When the data for dark current for films on aluminum contacts, for voltages from 0 V to approximately 100V, was fitted to the Richardson equation, the following typical values for the parameters were extracted (Figure 5.10). The value for the injection barrier height Φ_e, neglecting the Schottky effect, was typically between 0.7 – 1.3 eV, usually close to 0.7, where the expected value was 1.4 eV. The typical value for L* was 1.2 - 2 microns, usually close to 1.2. A narrow range of values for the effective mass could not be obtained from fits of data to the Richardson equation; the value could be allowed to range within one to two orders of magnitude of unity m_e with

little effect on the other parameters. The value extracted for Φ_e was 0.7 eV for gold contacts, an order of magnitude too large. In general, fits of the data for films on gold electrodes to the Richardson equation were poor (Figure 5.10(b)). The poorer fit of curve to data for gold contacts, and the resulting error in the Φ_e parameter, is probably due to the real injection barrier height between gold contacts and ADT-TIPS-F films being too low to yield a truly injection-limited current, and to the Richardson equation therefore being no longer applicable to the overall I-V relation. These values for these parameters nevertheless suggest that the primary mode of charge injection for voltages up to approximately 100V, for aluminum and possibly also with gold contacts, is a form of thermionic emission. This suggests further that the current through the oxide layer on the aluminum contacts is an energetically neutral tunneling transport which serves to limit the current, without having a marked affect on the energy profiles at the barrier shown in Figure 5.9. Injection via thermionic emission in an injection-limited system is consistent with the positive temperature dependence we have seen in experiments with CW photocurrents over temperature.

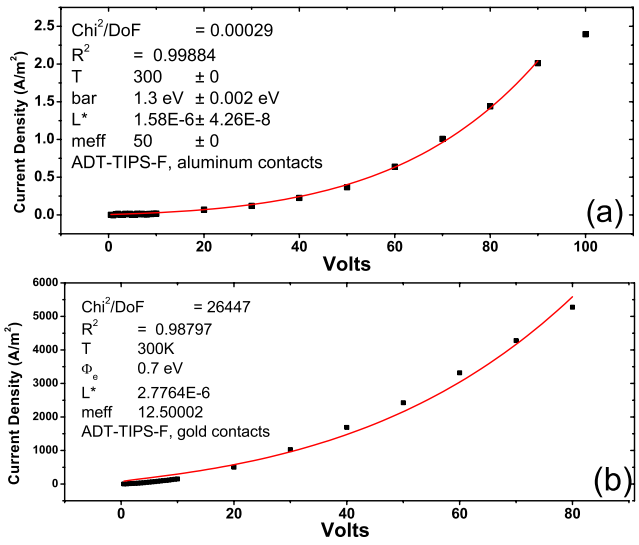

Figure 5.10. Fit of dark current data to Richardson equation, for ADT-TIPS-F thin films. (a) aluminum contacts, (b) gold contacts.

For most of the films on aluminum contacts, the data for voltages from 150 to 300 V showed a tendency to level off at the higher voltages, probably due to an approach to saturation. Hence, if one attempts to fit such data for higher voltage ranges to the Richardson equation, the fit in such cases becomes progressively poorer as the voltage range increases. If one produces a Fowler-Nordheim plot, however, for the data for voltages from 0 to 300 Volts, even in the cases where the current trends towards saturation, it is apparent that there is a transition, at a voltage in the neighborhood of 130 volts, to a linear relation between $\ln(I/F^2)$ and $1/F$, in agreement with the Fowler-Nordheim equation (Figure 5.11). Such a linear relation is an indication of tunneling injection. In our case, in other words, one observes a transition from injection via thermionic emission to injection via tunneling. Here "tunneling" means, not tunneling through the oxide layer on the aluminum, but through the Schottky barrier at the reverse-biased positive electrode.

In the case of one film, however, which reached 300 V without ever approaching the current levels where saturation was observed, an excellent fit to the Richardson equation was obtained. This suggests that if the dark currents for the other films over the full 0 - 300 V range had not trended towards saturation at the higher voltages, they would also have fitted well to the Richardson equation. The Fowler-Nordheim plot for that film, however, also yielded a typical value for the coefficient κ, from which a typical value for Φ_B was deduced. More generally, data which did not fit the Richardson equation well at higher voltages nevertheless was found to yield good Fowler-Nordheim plots, suggesting that currents at higher voltages are governed primarily by tunneling through the Schottky barrier.

In view of the fact, as may be inferred from Figure 5.7, that the electric field across the gap is not uniform, the electric field strength parameter F in the Fowler-Nordheim equation is difficult to quantify. We are interested in the field strength specifically at the injection interface. We know the voltage across the gap as a whole, and therefore the average field strength across the gap, but one of the two electrodes may be screened across a significant portion of the gap by space charge.[111,114] If this is the case, the

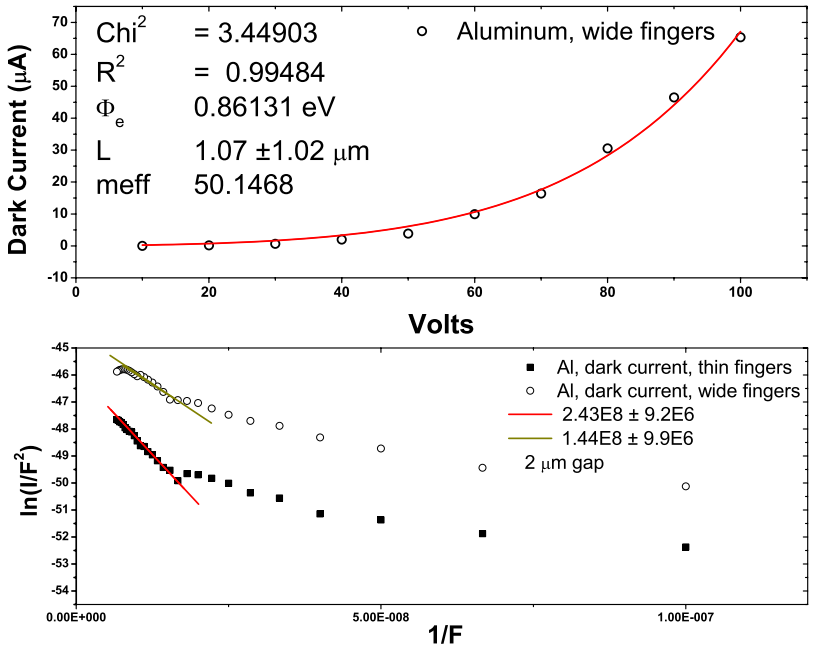

Figure 5.11. Top: ADT-TES-F, dark current, applied voltage 0 to 200V, fit to Richardson equation for thermionic emission. Bottom: Fowler-Nordheim plot of dark current for two different samples, for applied voltage 10 to 300 V. Data for voltages 150 to 300 fitted to Fowler-Nordheim tunneling theory. Fit yields value for κ (Equation 5.2). Assumption: 2μm effective gap size.

effective gap width, as described above, may be much narrower, and the field strength at the gap, therefore, much greater than the average. As a means of estimating both the effective gap width and the field strength across the interface, the data was fitted to the Richardson equation in a manner which allowed the extraction of the effective gap width L* (defined above) as one of the parameters. The values extracted for L* in this way were fairly consistent, in the neighborhood of 1 to 2 microns. The field strength F needed to generate the Fowler-Nordheim plots was then the applied voltage divided by L*. The resulting values for the barrier height Φ in the tunneling regime ranged from 0.1 to 0.3 eV.

The value for Φ_e (the injecton barrier height without consideration of the Schottky effect), which is obtained from fits of the data to the Richardson equation, as mentioned above, is 0.7 eV. This does not agree with the expected value, 1.4 eV. One may introduce here a modification of the Schottky interface model, which takes into account the possibility of an interface dipole layer between the metal contact and the bulk material (Figure 5.9(c)). Such an interface dipole typically produces a vacuum level shift, so that the vacuum energy levels of the organic material and the metal no longer align.[116,117]

Hence one may postulate, in the case of the interface under discussion, that the vacuum level shift at the interface is +0.7 eV, effectively reducing Φ_e from 1.4 eV to 0.7 eV. If one calculates further $\Phi_e - \Delta\Phi$ at 150 V (Equations 5.5, 5.6), one obtains a value of 0.3 eV, in close agreement with values obtained from the Fowler-Nordheim plots. The magnitude and sign of the dipole layer at the interface between ADT-TES-F or ADT-TIPS-F and self-anodized aluminum has, to our knowledge, not been determined. But work with pentacene and various metal contacts (Au, Ag, and Pt) has found a linear relation between the work function and the magnitude of the interface dipole.[12] This linear relation suggests the existence of an interface dipole between pentacene and aluminum which would produce a vacuum level shift of +0.3 eV. A dipole layer of the same sign, but approximately twice the magnitude (+0.6 to +0.7 eV), at the interface between ADT-TES-F and aluminum, would yield a good agreement between the values obtained for the height of the injection barrier in the two voltage regimes we have described. The barrier height will drop to a value of approximately 0.3 eV when the voltage across the electrodes reaches 150 V, at which point the transition from thermionic emission to tunneling injection takes place. Once in the tunneling regime, the barrier height remains at 0.3 eV up to 300 V.

Aluminum contacts, CW photocurrent. We have already noted the difference between CW versus dark current in films with aluminum, compared with films with gold contacts. Specifically, if CW and dark currents in films on gold contacts are fitted to power-laws, the exponents are very close. But if the same fit is done with

data for films on aluminum contacts, the CW currents typically fit to power-laws with exponents sometimes significantly greater than the exponents for dark currents.

We assumed, in the analysis which allowed us to fit dark current data to to the Richardson equation, for the 1 to 100 V portion of the voltage range, that the effective gap width was a constant over the range. This allowed us to extract the parameter L*, which then allowed us to produce Fowler-Nordheim plots from which we could extract a consistent barrier height for the higher-voltage, tunneling regime. But simulations by Hurd and McKinnon suggest that, for certain materials, there may be a significant enlargement in the screening of one or the other of the electrodes, and a concomitant reduction in the effective gap width, for increases in the applied voltage smaller than an order of magnitude.[114] This is due to the accumulation of space charge, particularly steady-state mobile space charge. If it should happen that the space charge accumulation very near the positive electrode is augmented by the greater carrier density due to light-and-field assisted carrier generation in the already narrow effective gap, and by the energy gradient faced by carriers crossing the interface to a semi-blocking contact, then the screening of the negative electrode will be greater, and the effective gap-width correspondingly smaller. In that case, the E-field gradient near that contact will tend to rise more steeply as a function of voltage than it would in the case of dark current. If CW photocurrent, then, varies with E-fields near the positive electrode (which is the reverse-biased Schottky junction), we would expect it to rise more quickly as a function of voltage than in the case of dark current.

The transition. In the case of aluminum electrodes, when one has become familiar with the plots of dark current, whether linear, log-log, or Fowler-Nordheim, one sees that in all cases the transition from what we have called the lower-voltage regime (0 – 130 V) to the higher-voltage regime (130 – 300 V) is not smooth. This is particularly plain in a log-log plot of current versus voltage across the entire 0 – 300 V range (Figure 5.12). At the transition voltage, around 130 V, there is a drastic increase in the exponent, if one chooses to fit the data to a power-law. This transition voltage

corresponds to the lower field-strength F for the range of data points which are linear in the corresponding Fowler-Nordheim plot.

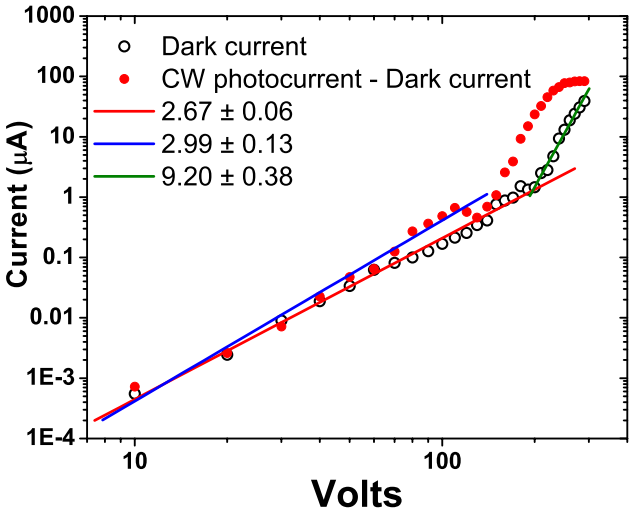

Figure 5.12. Dark current and CW - dark current, ADT-TES-F film on aluminum electrodes

In other words, if we are correct in supposing that there is a transition from thermionic injection to injection via tunneling at the transition voltage, it appears to be quite sudden, in comparison to data reported elsewhere.[116] There is often, as seen in the data for CW current with dark current subtracted (Figure 5.12), an actual small dip in the current with increasing voltage, just before the I-V relation assumes a quantitatively much different character in the 130 – 300 V range. In work by Forrest *et al*,[1] this general form of the I-V plot is associated with injection into disordered materials, although there is no suggestion in that work that the currents with the steeper I-V relation are due to injection via tunneling. Rather, the model there proposed views such injection as a stepwise hopping through a series of densities-of-state characteristic of disordered materials near an interface. The question of what makes the transition we have observed so sudden remains open.

5.4.3 Gold contacts

The primary difference between dark currents and CW photoresponses, in ADT-TES-F thin films with gold electrodes, from those in films with aluminum electrodes, is that the behavior of the electrode-film-electrode system is no longer governed almost exclusively by what happens at the interfaces, or at one of the two interfaces. The current is no longer injection-limited. Interface effects play a role, but it is no longer the dominant role.

Mobility. If the currents in ADT-TES-F thin films on gold electrodes are primarily bulk-limited, then it should be possible to estimate the hole mobility, using the Mott-Gurney relations for space-charge limited currents. In a sandwich electrode configuration, current density in the (SCLC) regime has a quadratic dependence on the strength of the E-field, and an inverse cubic dependence on the electrode spacing. For dark current, the relation is given by the Mott-Gurney Law:

$$J \approx \frac{9\mu\epsilon\epsilon_0}{8}\frac{U^2}{L^3} \tag{5.7}$$

where U is the potential difference and L is the spacing between the electrodes.[21] This equation describes what is sometimes referred to as 2-D SCLC. However, in a coplanar electrode configuration, assuming that the current flows as an infinitely thin sheet, the relation derived by Geurst applies:[119]

$$J \approx \frac{2\mu\epsilon\epsilon_0}{\pi}\frac{U^2}{L^2}, \tag{5.8}$$

for what is called 1-D SCLC.

Using the first equation to relate current density to U^2 allows a value for mobility to be extracted, for a ADT-TIPS-F film on gold electrodes, of 0.63 $cm^2/(Vs)$. Using the second yields a comparable mobility of 0.047 $cm^2/(Vs)$ ((Figure 5.13, (a) and (b),

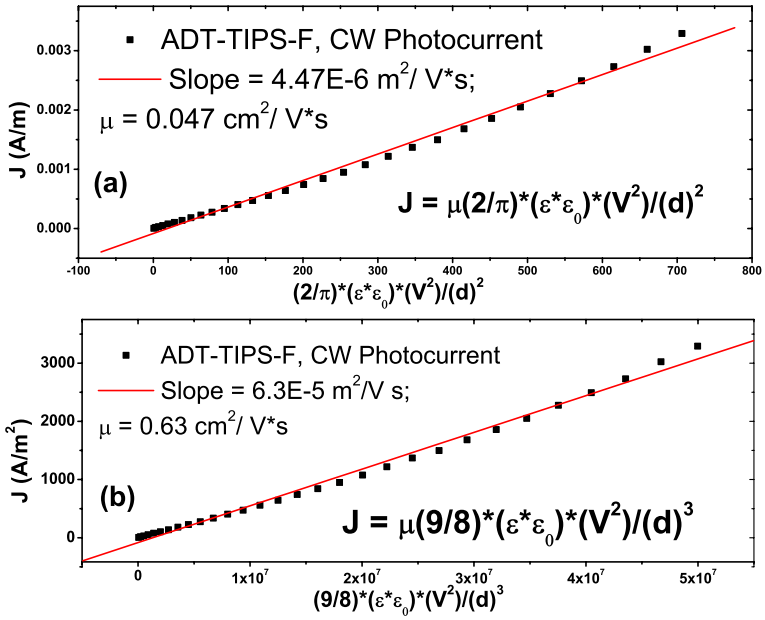

Figure 5.13. CW photocurrent, in ADT-TIPS-F with gold electrodes, plotted to fit (a) the 2-D Mott-Gurney relation and (b) the 1-D (Geurst) version of the Mott-Gurney relation.

respectively). Since the two equations govern the two extremes of the ratio between electrode thickness and gap width, these two values set upper and lower limits on the mobility in our films. The values thus obtained are within an order of magnitude of values for mobility reported recently by Subramanian *et al* for ADT–TES–F, using FET methods.[120] This may be taken as further support for the position that the photocurrents we observed in samples with gold electrodes are indeed bulk-limited and SCL currents. However, the photo-excitation profile in Figure 5.7 suggests that, while the barrier heights at the two interfaces with gold contacts are much lower than those for aluminum, the space charge density across the gap is still far from uniform, which implies that the energy cost of transport across at least one of the interfaces is significant even with gold contacts. The positive electrode appears, that is, to be at least partly a blocking contact.

Low injection barriers. The principal difference between dark current and CW photocurrent plots for films on gold versus those on aluminum is that on gold, the dark and CW currents stand in an almost constant ratio to one another over our voltage range, but are otherwise essentially the same. The ratio of CW to dark is relatively small, meaning that the dark currents in films on gold are relatively quite large. This may be taken as an indication that the role played in these currents by contact effects, for films on gold contacts, is smaller than in films on aluminum contacts. If the CW photocurrent with dark current subtracted is plotted against voltage for both aluminum and gold, it is apparent that, even if an equal quantity of carriers are photo-injected into films on each metal, under conditions of the same intensity of CW illumination, far fewer of them are able to traverse the interface between the film and the aluminum electrodes. This is, in other words, a further indication that the currents in the films on aluminum electrodes are injection-limited, while those in films on gold are not.

Even though both dark and photocurrents in films on gold are therefore likely to be bulk-limited rather than injection-limited, and there is good reason to think they are space-charge-limited, they do not show the quadratic relation between current and voltage which agrees with the Mott-Gurney relation. Rather, as seen in Figures 5.4 and 5.5, a log-log plot of current against voltage does not give a power-law relation over a large voltage range. However, data for dark current can be fitted with some degree of success to the Richardson equation (Figure 5.14(b), with data for aluminum shown for comparison in (a)). This suggests that the measured CW photocurrent in films with gold electrodes is shaped both by bulk, space-charge effects and by contact effects, i.e., that it is, in some sense, both contact- and bulk-limited.

5.4.4 Peak transient photoresponse versus CW

While the amplitudes of transient photoresponses for ADT-TIPS-F films with gold and with aluminum electrodes are comparable, it will be noted in Figure 5.1(b) that the response decays more quickly for the films on aluminum electrodes. This is consistent with the view that the transient response is governed by the characteristics

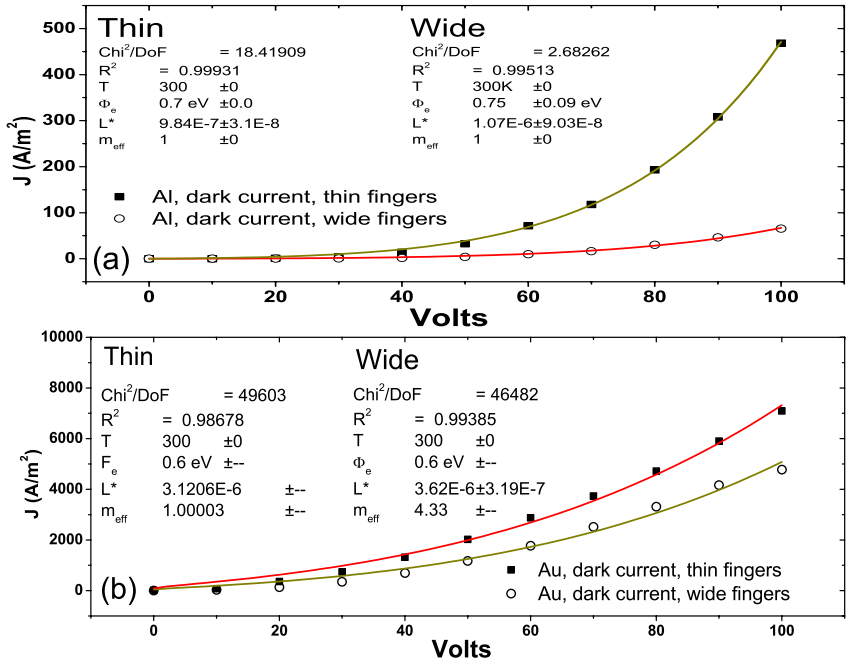

Figure 5.14. (a) ADT-TES-F Film on Al electrodes, thin fingers and wide, dark current data fitted to Richardson equation. (b) ADT-TES-F Film on Au electrodes, thin fingers and wide, dark current fitted to Richardson equation.

of the bulk material on the shortest time scales, on the order of the rise-time of the transient, but that the effects of injection-limitation become noticeable on time-scales of the order of the time-of-flight from the point of excitation to the nearest electrode. It is to be expected that the locus of most intense photogeneration of carriers would be similar to the zone of the peak photoresponse seen in the gap scan (Figure 5.7). In the case of aluminum, a significant portion of the total volume of carriers are generated at distances from the positive electrode which are a few percent of the total gap width. If the carrier fails of ejection at the contact, due to the higher Schottky barrier or to the resistance of the oxide layer, the decay of the transient response will be faster. Assuming an electron mobility of 0.1 $cm^2/(Vs)$, and an E-field strength of 4 x 10^6 V/m, a free electron generated at a point 2.50 μm from the positive electrode will take 62.5

ns to reach it. However, it was argued above that, due to space-charge screening of the negative electrode, the effective gap width L* is much narrower than the 25 μm distance between the electrodes. If we take L* to be 2 μm, then the E-field strength within the effective gap is $\sim$5 x 10^7 V/m, and the transit time across the effective gap is $\sim$4 ns. A time of this order is consistent with the observed difference between the decays in (Figure 5.1)

In terms of time-of-flight (TOF) phenomena, this may be understood as follows. Consider a carrier in transit from its point of photogeneration towards the electrode. This movement will constitute a measurable current while it is in transit, the same regardless of the nature of the contact metal. The movement of the carrier is a shift in the electrostatic equilibrium within the gap, which by continuity must be balanced by a corresponding shift in the equilibrium of the external circuit. This appears as a measurable current. But if, when the carrier reaches the electrode, its extraction (or ejection) is blocked, by a Schottky barrier or by an oxide layer, the current then ceases, or is slowed. This corresponds to the tail end of a typical time-of-flight wave-form. Or, in our case, it corresponds to a contribution by the carrier, delayed at the interface, to the decay of the transient photoresponse, which is observed to be faster for films with aluminum contacts than for those on gold. Now, in the experiment under discussion, the aluminum contacts are not completely blocking contacts, as they are in a real TOF experiment. Nevertheless, if the movement of the carrier across the interface is hindered, there will be, if not the fast falling-off we see at the tail end of a TOF pulse, then a hastening of the gradual decay already in progress as a result of trapping and recombination processes.

This accounts for the similarity in the amplitudes of transient photoresponses in films on gold and on aluminum electrodes, compared with the great difference in CW photoresponse. The peak photocurrent corresponds to movement of charge on time scales much too short for the effects of blocking at the interfaces to be evident. Transient peak amplitudes, in other words, are governed by the bulk characteristics of

the material between the contacts. CW photoresponse, on the other hand, is a steady-state process in which the nature of the contacts is very much evident, playing the dominant role in the case of aluminum contacts.

Although the E-field gradient near the positive electrode is much greater, in the model proposed here, for films with aluminum contacts than for films with gold, the volume of organic material in which there is field strength great enough to separate geminate electron-hole pairs, or to move photo-generated free carriers, is much smaller. This is due to the screening of the negative aluminum electrode by space charge and to the resulting narrowing of the effective gap.[114] Most e-h pairs will be formed at distances from the positive electrode where they will almost certainly recombine, since the voltage potential is relatively flat except for the region very near the positive electrode. In films with gold electrodes, on the other hand, the total volume in which e-h pairs are generated and the E-field is strong enough to separate them is much greater. To put it differently, if a transient photoresponses were integrated with respect to time to yield the total charge Q collected by the positive electrode, it would be much smaller for aluminum contacts than for gold.

5.4.5 Transient response to localized excitation

Data was also taken for transient photoresponse with the beam focused to a diffraction-limited beam spot within the electrode gap. The sample used was a simple coplanar electrode pair (Fig. 5.6), with a 50 μm gap width. The lens by which the beam was focused was mounted in a micrometer-controlled translation-stage, and the beam spot traversed the gap under manual control of the micrometer. The spot position could be read off the micrometer, since the spot displacement was found to be 97% of the lens displacement. Transient photoresponses were measured at 10 micron intervals as the spot traversed the gap, and then the traversal was repeated with the polarity reversed. Data was taken for ADT-TES-F films on both gold and aluminum electrodes.

It was found that the signal-to-noise ratio of the transients was such that no unambiguous conclusion could be drawn regarding the possible difference made in the

shape of the photocurrent transient by positioning the beam spot near the positive or near the negative electrode. The data did, however, agree with other results for which the photoresponse decay was much faster for films on aluminum electrodes than on gold.

5.4.6 Back illumination versus front

Under illumination from the glass substrate side, transient photoresponse was typically greater, by a factor of two or three, than response under illumination from the film/electrode side. This suggests that when the sample is illuminated from the film side, and incident light must travel through the film to reach the electrode, the resulting absorption is only partially compensated for by the addition of carriers via photoemission or photoinjection. This suggests in turn that, since our films are thin, these processes do not make a significant contribution to the total current. This relation held both for films on aluminum electrodes and on gold electrodes, which indicates that a low contribution from photoinjection is not due simply to injection blockage by the aluminum oxide film.

CW photocurrent shows a similar relationship between different photoresponses measured with illumination on the two different sides of the glass slide.

5.5 Conclusions

In this chapter is presented data confirming the important role played by contacts, in the overall performance of those devices in which organic semiconductors must interface with inorganic materials, particularly metals. Two metals were chosen with very different work functions and with very different surfaces, both from a chemical and from a structural point of view, i.e., one (aluminum) presents a self-anodized oxide surface to the interface, the other (gold) does not. It was found that the overall performance of the contact-film-contact structure could be modeled, particularly in the case of aluminum contacts, as an anode-to-anode Schottky diode structure, incorporating a postulated

interface dipole layer between bulk metal and bulk organic semiconductor. The particular features of this model for the aluminum/organic interface were used to account for the behavior of the dark and CW photocurrents over a range of applied voltages from zero to 300 V, for an electrode gap width of 25 μm. It was found that the overall features of the I-V relation for aluminum contacts could be understood as involving two regimes, a lower-voltage (0 - 130 V) regime in which charge is injected via thermionic emission, over the Schottky barrier, and a higher-voltage regime in which injection is via tunneling through the barrier. The contrasting features of the dark and photocurrents in films with gold electrodes are understood as due to the reduced role played by interface effects in those dynamics, and the dominant role played by bulk, particularly space-charge-limited effects. The overall similarity of the transient photoresponses of films with gold electrodes compared with films with aluminum electrodes is explained in terms of the fast component of the transient being governed by charge dynamics within the bulk material, which take place on time-scales too short for interface effects to be manifest.

On the Photoresponse of Several Novel Functionalized Oligoacene
and Anthradithiophene Derivatives

CHAPTER 6
SUMMARY AND CONCUSIONS

In this work a study of the electronic properties of some novel pentacene and anthradithiophene derivatives, members of that broad class of materials referred to as "organic semiconductors," has been undertaken. We have employed real-time contact methods to measure the transient photo-response of these materials, under conditions of varied electric field, light intensity, and temperature, as a means of characterizing the different charge-transport modes which may be operating, singly or in combination, at successive times after the initial photo-excitation. We have also examined their behavior on longer-times scales, up to tens of seconds, while varying the same environmental parameters. We have extended this inquiry, into the question of how the interface between the organic semiconductor and the external circuit may shape its measurable behaviors, with particular reference to the build-up and the distribution of space-charge in the thin film between the metal contacts. Samples of thin films were prepared with electrical contacts of two very different metals, gold and self-anodized aluminum, and consequently very different physics at the interfaces, and measurements were made of transient photo-response, of currents under steady-state or continuous-wave (CW) illumination, and of dark currents. We have probed the electronic structure of these materials on a molecular level, by doping them with both related molecular substances, and with very different molecules, a refractive glass and the buckminsterfullerene C_{60}. Here again, data was taken on short to long time scales, both transient and CW photocurrents, and steady-state dark current.

As a result of these experiments, we are not able to fully answer the question, to what extent are the charge carriers generated by fast pulses de-localized, or in extended

or even coherent states, in the first pico-seconds to tens of nano-seconds after excitation. But we are able to assert that in these materials, the charge carriers on the shortest time-scales we are able to measure do give rise to characteristics shared with materials for which the semiconductor band model is applicable: among others, a peak photo-response which does not arise from thermally-activated or field-assisted carrier generation, and an inverse dependence of mobility on temperature. On longer time-scales, we observe behavior which suggests that excited states take longer to relax to a steady-state mode than might be expected, if the carriers were restricted to transport via hopping, or even via hopping-via-tunneling.

Further, data for electronic characteristics produced or altered by doping indicate that the results of doping, on long time-scales, may be understood in a fashion closely analogous to the theory of doping of inorganic semiconductors, in which a material whose majority carrier is holes will see its DC conductivity increased by doping with p-type, electron-accepting, dopants and decreased by n-type dopants. On short time-scales, the results of this doping support the conclusions drawn from earlier analysis of data from measurements of transient photo-response, that photo-excited charge carriers in these materials are initially in de-localized states, and relax to progressively more localizes states as time passes.

Finally, we find that samples prepared with the simplest of methods, drop-casting from solution onto glass substrates pre-patterned with metal contacts, will yield thin films which interface with the contacts in a fashion which is functonal, and which may be understood in terms of a modified Schottky barrier model, incorporating an interface-dipole vacuum shift which is postulated to have a magnitude of +0.6 to +0.7 eV. In the case of films on aluminum contacts, a shift in injection-mode from thermionic emission to injection-via-tunneling is observed, at overall electric-field strength of $\sim$6 x 10^6 V/m.

REFERENCES

[1] S.R. Forrest, Nature 428 (2004) 911.

[2] J.E. Anthony, Chem. Rev. 106 (2006) 5028.

[3] O. Ostroverkhova and W.E. Moerner, Chem. Rev. 104 (2004) 3267.

[4] N.S. Sariciftci, Primary Photoexcitations in Conjugated Polymers: Molecular Exciton versus Semiconductor Band Model (World Scientific, Singapore, 1997).

[5] F.A. Hegmann, Physics in Canada 59 (2003) 127.

[6] Z. Li et al., Phys. Rev. Lett. 99 (2007) 016403.

[7] V.K. Thorsmølle et al., Appl. Phys. Lett. 84 (2004) 891.

[8] O. Ostroverkhova et al., Phys. Rev. B 71 (2005) 035204.

[9] O. Ostroverkhova et al., J. Appl. Phys. 98 (2005) 033701.

[10] O. Ostroverkhova et al., Appl. Phys. Lett. 88 (2006) 162101.

[11] E.A. Silinsh and V. Capek, Organic Molecular Crystals: Interaction, Localization, and Transport Phenomena (AIP Press, New York, 1994).

[12] L. Diao et al., J. Appl. Phys. 101 (2007) 014510.

[13] D. J. Gundlach et al., Nature Materials 7 (2008) 214.

[14] R.M. Glaeser and R.S. Berry, J. Chem. Phys. 44 (1966) 3797.

[15] D. Herte et al., J. Chem. Phys. 110 (1999) 9214.

[16] J.I.P. (Ed), Semiconductors and Semimetals, Vol. 21, Part C (Academic Press, Orlando, 1984).

[17] C.K. Chiang et al., Phys. Rev. Lett. 39 (1977) 1098.

[18] A.J. Heeger, Rev. Mod. Phys. 73 (2000) 681.

[19] A.B. Kaiser, Rep. Prog. Phys. 64 (2001) 1.

[20] H. Scher and E.W. Montroll, Phys. Rev. B 12 (1975) 2455.

[21] M. Pope and C.E. Swenberg, Electronic Processes in Organic Crystals (Oxford University Press, New York, 1982).

[22] J.E. Anthony, D.L. Eaton and S.R. Perkin, Org. Lett. 4 (2001) 15.

[23] J.S. Brooks et al., Contrib. Atmos. Phys. 1 (2001) 301.

[24] S.K. Park et al., Appl. Phys. Lett. 91 (2007) 063514.

[25] O. Ostroverkhova et al., Adv. Funct. Mat. 12 (2002) 621.

[26] O. Ostroverkhova et al., Chemphyschem 4 (2003) 732.

[27] J. Chen, J. Athony and D.C. Martin, J. Phys. Chem. B 110 (2006) 16397.

[28] C. Lee et al., Phys. Rev. B 48 (1993) 15425.

[29] O. Ostroverkhova et al., Phys. Rev. B 71 (2005) 035204.

[30] K.P.H. Lui and F.A. Hegmann, Appl. Phys. Lett. 78 (2001) 3478.

[31] A. Othonos, App. Phys. Rev. 83 (1997) 1789.

[32] F.A. Hegmann et al., Proc. SPIE 5352 (2004) 196.

[33] Z. Rang et al., Appl. Phys. Lett. 79 (2001) 2731.

[34] W. Graupner et al., Phys. Rev. Lett. 81 (1998) 3259.

[35] M. Gailberger and H. Bassler, Phys. Rev. B 44 (1991) 8643,

[36] R. Kersting et al., Phys. Rev. B 73 (1994) 1440.

[37] V. Arkhipov et al., Phys. Rev. B 61 (2000) 8207.

[38] S. Barth et al., Phys. Rev. B 56 (1997) 3844.

[39] S. Barth et al., Chem. Phys. Lett 274 (1997) 165.

[40] O. Ostroverkhova et al., Proc. SPIE 5517 (2004) 163.

[41] L. Onsager, Phys. Rev. 54 (1938) 554.

[42] D. Moses, A. Dogariu and A.J. Heeger, Phys. Rev. B 61 (2000) 9373.

[43] C.H. Lee et al., Phys. Rev. B 49 (1994) 2396.

[44] E.A. Silinsh et al., Chem. Phys. 198 (1995) 311.

[45] D. Moses, M. Sinclair and A.J. Heeger, Phys. Rev. B 58 (1987) 2710.

[46] J. Oliver H. LeBlanc, J. Chem. Phys. 35 (1961) 1275.

[47] G. Weiser, Phys. Rev. B 45 (1991) 14076.

[48] H. Eckhardt, K.Y. Shacklette and R.L. Eisenbaumer, J. Chem. Phys. 91 (1989) 1303.

[49] B. Kraabel et al., J. Chem. Phys. 104 (1996) 4267.

[50] D. Moses et al., Phys. Rev. B 54 (1996) 4748.

[51] R. W. I. de Boer et al., J. Appl. Phys. 95 (2004) 1196.

[52] D.M. Pai and R.C. Enck, Phys. Rev. B 11 (1975) 5163.

[53] P.B. Miranda, D. Moses and A.J. Heeger, Phys. Rev. B 58 (1987) 2710.

[54] F.A. Hegmann et al., Phys. Rev. Lett. 89 (2002) 227403.

[55] A.R. Murphy and J.M.J. Frechet, Chem.Rev. 107 (2007) 1066.

[56] J. Zaumseil and H. Sirringhaus, Chem. Rev. 107 (2007) 1296.

[57] I.D.W. Samuel and G.A. Turnbull, Chem. Rev. 107 (2007) 1272.

[58] Y. Shirota and H. Kageyama, Chem. Rev. 107 (2007) 953.

[59] V. Podzorov et al., Phys. Rev. Lett. 93 (2004) 086602.

[60] V. Podzorov et al., Phys. Rev. Lett. 99 (2007) 016403.

[61] O.D. Jurchescu, J. Baas and T.T.M. Palstra, App. Phys. Lett. 84 (2004) 3061.

[62] J.Y. Kim et al., Science 317 (2007) 222.

[63] F.A. Hegmann, Physics in Canada 59 (2003) 127.

[64] R. Schuster, M. Knupfer and H. Berger, Phys. Rev. Lett. 98 (2007) 037402.

[65] H. Marciniak et al., Phys. Rev. Lett. 99 (2007) 176402.

[66] V. Coropceanu et al., Chem. Rev. 107 (2007) 926.

[67] P. Parisse et al., J. Phys 19 (2007) 106209.

[68] F.A. Hegmann, O. Ostroverkhova and D.G. Cooke, Probing organic semiconductors with terahertz pulses, Photophysics of molecular materials, edited by G. Lanzani, pp. 367–428, Wiley-VCH, Weinheim, 2006.

[69] D. Moses, A. Dogariu and A.J. Heeger, Physical Review B 61 (2000) 9373.

[70] C. Soci et al., Phys. Rev. B 72 (2005) 245204.

[71] H.Y. Liang et al., Chemical Physics Letters 419 (2006) 292.

[72] T. Tokumoto et al., Journal of Applied Physics 92 (2002) 5208, Times Cited: 3 Article English Cited References Count: 6 607aa.

[73] J.S. Brooks et al., J. Appl. Phys. 96 (2004) 3312.

[74] D. Moses et al., Physical Review Letters 80 (1998) 2685, Times Cited: 44 Article English Cited References Count: 22 Zd178.

[75] G. Horowitz et al., Phys. Rev. B 59 (1999) 10651.

[76] C.H. Lee et al., Physical Review B 48 (1993) 8506, Times Cited: 42 Note English Cited References Count: 34 Ly665.

[77] A.P. Platt et al., CLEO-QELS, Baltimore, Md, 2007.

[78] K.A. Willets et al., Journal of the American Chemical Society 125 (2003) 1174.

[79] K.A. Willets et al., Accounts of Chemical Research 38 (2005) 549.

[80] O. Ostroverkhova et al., Applied Physics Letters 89 (2006) 192113.

[81] D. Moses et al., Chem. Phys. Lett 350 (2001) 531, Times Cited: 7 Article English Cited References Count: 25 507yh.

[82] C. Im et al., J. Chem. Phys. 117 (2002) 2961.

[83] W. Laureyn et al., Electroanalysis 13 (2001) 204.

[84] E.L. Frankevich, Chem. Phys. Reports 17 (1999) 2069.

[85] M.C. Beard, G.M. Turner and C.A. Schmuttenmaer, Phys. Rev. B 62 (2000) 15764.

[86] P. Parkinson et al., Nano Lett. 7 (2007) 2162.

[87] J.S. Blakemore, J. Appl. Phys. 53 (1982) 123.

[88] O.E. Madelung, Semiconductors - Basic Data (Springer-Verlag, Berlin, 1996).

[89] N. Karl, Synthetic Metals 133 (2003) 649, Times Cited: 2 Article English Cited References Count: 45 660kb Sp. Iss. SI.

[90] N. Karl, Charge-carrier mobility in organic crystals, Organic Electronic Materials, edited by R. Farchioni and G. Grosso, Springer Series in Materials Science, p. 449, Springer, New York, 2001.

[91] E. Hendry et al., Physical Review Letters 92 (2004) 196601.

[92] D. Moses et al., Phys. Rev. Lett. 97 (2006) 067401.

[93] Y.C. Cheng et al., J. Chem. Phys. 118 (2003) 3764.

[94] M. Abkowitz, A. Lakatos and H. Scher, Phys. Rev. B 9 (1974) 1813.

[95] A. Rose, Concepts in photoconductivity and allied problems (Interscience Publishers, New York, 1963).

[96] P.M. Borsenberger and D.S. Weiss, Organic Photoreceptors for xerography, Optical Engineering Vol. 59 (Marcel Dekker, Inc., New York, 1998).

[97] G. Priebe, B. Pietzak and R. Konenkamp, Appl.Phys.Lett. 71 (1997) 2160.

[98] K. A. Willets et al., J. Am. Chem. Soc 125 (2003) 1174.

[99] O. Ostroverkhova et al., Appl. Phys. Lett. 82 (2003) 3602.

[100] M. Pope and C.E. Swenberg, Electronic processes in organic crystals and polymers, 2nd ed. (Oxford University Press, New York, 1999).

[101] J.C. Sancho-Garcia et al., Journal of Chemical Physics 119 (2003) 12563, Times Cited: 0 Article English Cited References Count: 30 750aw.

[102] G. Dellepiane et al., Phys. Rev. B 48 (1993) 7850.

[103] G.A. Gamal and M.I. Azad, Eur. Phys. J. Appl. Phys. 32 (2005) 1.

[104] A. Eray, G. Nobile and F. Palma, Mat. Sci. Eng. B 102 (2003) 398.

[105] R. Schwarz et al., Diamond and Related Materials 16 (2007) 1437.

[106] P. M. Borsenberger and D. S. Weiss, Organic Photoreceptors For Imaging Systems, (Marcel Decker, Inc, New York, New York, 1993).

[107] X. Zhang et al., Chem. Phys. Lett. 422 (2006) 386.

[108] P.G. Sheasby and R. Pinner, The Surface Treatment and Finishing of Aluminum and its Alloys, vol. 1 (sixth ed.) (ASM International and Finishing Publications, Materials Park, Ohio and Stevenage, UK, 2001).

[109] R. Handy, Phys. Rev. 126 (1962) 1968.

[110] Y. Julliard et al., 2000 Conference on Electrical Insulation and Dielectric Phenomena, Anaheim, CA, 2000.

[111] T. Agostinelli et al., J. Appl. Phys. 101 (2007) 114504.

[112] T.A. Skotheim and J.R. Reynolds, Conjugated Polymers: Theory, Synthesis, Properties and Characterization (CRC, Cleveland, Ohio, 2006).

[113] V.I. Arkhipov, U. Wolf and H. Bassler, Phys. Rev. B 59 (1999) 7514.

[114] C. M. Hurd and W. R. McKinnon, J. Appl. Phys. 75 (1994) 596.

[115] M. Schwoerer and H. C. Wolf, Organic Molecular Solids, Wiley-VCH Verlag GmbH and Co., KGaA, Weinheim.

[116] I.D. Parker, J. Appl. Phys. 73 (1993) 1656.

[117] H. Ishii et al., Kelvin probe study of band bending at organic semiconductor/metal interfaces: Examination of fermi level alignment. Physics of Organic Semiconductors, edited by W. Brutting, pp. 69–94, Wiley-VCH, 2005.

[118] J. Reynaert et al., Adv. Funct. Mat. 16 (2006) 784.

[119] J.A. Geurst, Phys. Status Solidi 15 (1966) 107.

[120] S. Subramanian et al., J. Am. Chem. Soc. 130 (2008) 2706.

[121] O. Ostroverkhkova and K. D. Singer, Phys. Rev. B 69 (2002) 125216.

[122] J. S. Schildrkraut and A. V. Buettner, J. Appl. Phys. 72 (5) (1992) 1888.

[123] J. S. Schildkraut and Y. P. Cui, J. Appl. Phys. 72 (11) (1992) 5055.

[124] J. Y. Lee and J. H. Kwon, Appl. Phys. Lett. 88 183502 (2006).

APPENDIX A: CALCULATION OF THE $\mu\eta$ PRODUCT FROM TRANSIENT PHOTOCURRENT DATA

Consider a current $\mathbf{I}$ flowing through a channel of cross-sectional area A. The area A is the product of the width W and the depth T of the channel, the current density $\mathbf{J}$ is $\mathbf{I}/A$, the total charge Q which has transited the channel in time t is

$$Q = \int_0^t \mathbf{I} dt \tag{1}$$

$$= A \int_0^t \mathbf{J} dt = WT \int \mathbf{J} dt \tag{2}$$

But the current density $\mathbf{J} = \sigma \mathbf{E}$, the product of the electrical field strength and the conductivity of the material. The conductivity σ is equal in turn to $ne\mu$, the product of the carrier density n, the charge of the electron e, and the carrier mobility μ. This gives

$$Q = WT \int_0^t \sigma \mathbf{E} dt = WT \int ne\mu \mathbf{E} dt \tag{3}$$

$$= WT \int_0^t \frac{N_{carriers}}{V} e\mu \mathbf{E} dt \tag{4}$$

If we take the number of carriers $N_{carriers}$ to be the product of the number of incident photons and the photogeneration efficiency η of the material, or $N_{carriers} = N_{photons}\eta$, and if we further assume that the number of carriers falls off exponentially, due to trapping/recombination, with some time constant τ_2, we get

$$Q = WT \int_0^t \frac{N_{photons}\eta}{V})(e^{-\frac{t}{\tau_2}}) e\mu \mathbf{E} dt. \tag{5}$$

Assuming further that the current will correspondingly fall off exponentially, so that $\mathbf{I} = \mathbf{I}_0 e^{\frac{t}{\tau_1}}$ for some time constant τ_1, we have

$$Q = I_0 \int_0^t e^{-\frac{t}{\tau_1}} dt, \tag{6}$$

and we get, taking everything as constant except the exponential decay factors,

$$Q = I_0 \int_0^t e^{-\frac{t}{\tau_1}} dt = \frac{WTN_{phot}}{V} \eta e \mu \mathbf{E} \int e^{\frac{t}{\tau_2}} dt \tag{7}$$

$$= \frac{WTN_{phot}}{Vol} \eta e \mu E \int e^{-\frac{t}{\tau_2}} dt. \tag{8}$$

Making the reasonable assumption that the exponential decay constants τ_1 and τ_2 can be taken to be equal, the integral is then the same on both sides of the equation, and we get

$$I_0 = \frac{WTN_{phot} \eta e \mu E}{V} \tag{9}$$

or

$$\mu\eta = \frac{I_0 V e E}{WTN_{phot}}, \tag{10}$$

where I_0 is peak photocurrent, E is electric-field-strength, e is electron charge, V is the volume of sample irradiated, W and T are the width and thickness, respectively, of the photocurrent channel, and N_{phot} is the number of absorbed photons per pulse. This may be written more simply as

$$\mu\eta = \frac{j_0}{n_{phot} e E} \tag{11}$$

where j_0 is the peak photocurrent density, and n_{phot} is the density of absorbed photons per pulse.

APPENDIX B: DISPLACEMENT CURRENTS AND FRANKEVICH'S ANALYSIS

Frankevich has analysed the respective contributions of displacement current and free carriers to the transient photoresponse in a polarizable material.[84] For two cases pertinent to our experiments, for relatively low mobility μ and for relatively high μ, simulations based on his analysis show that for only the first case does a displacement current contribute significantly to the overall transient waveform. This is indicated in Figure 1.

A brief digest of Frankevich's analysis follows.

First:

"Suppose that the lifetime of charge carriers τ_{free} is controlled by their capture by defects and $\tau free \ll T$, where T is the time it takes for charge carriers to cover the distance l between the electrodes, $T = l^2/\mu V$ (μ is the mobility of charge carriers). If so, the kinetics of photoelectric current is governed by equation

$$i_{free}(t) = N_{free}\mu\frac{Ve}{l}exp\left(\frac{t}{\tau_{free}}\right)" \tag{12}$$

Here, $N_{free} = I\beta_{free}\tau_{free}$ is the number of free charge carriers generated by a light pulse; I is the rate of light absorption by the sample (quantum/s); β_{free} is the quantum yield of free charge carriers; e is the electron charge; l is the separation between the electrodes."

For a circuit such as ours, the signal is not measured as current, but as voltage across a load resistor. Then

$$i(t) = \frac{u(t)}{R} + C\frac{du}{dt} \tag{13}$$

Equation 12 then becomes

$$u_{free}(t) = N_{free}\mu\frac{V\cdot\tau_{free}\cdot 1.6\cdot 10^{-19}}{l^2}\left[exp\left(-\frac{t}{RC}\right) - exp\left(-\frac{t}{\tau_{free}}\right)\right](RC-\tau_{free})^{-1} \tag{14}$$

Second:

"If a light pulse impinging on a sample generates species prone to polarization, there arises displacement current i_{pol} in the circuit

$$i_{pol} = \frac{1}{l}\frac{d(N_{pol}p)}{dt}, \tag{15}$$

Here N_{pol} is the number of polarized particles formed in the sample, p is the dipole moment of a particle induced by the electric field $E = V/l$, where V is the applied voltage, and l is the separation between the electrodes."

The dipole moment as a function of time is

$$p = \alpha \frac{V}{l} \left[1 - exp\left(-\frac{t}{\tau_{pol}} \right) \right] \tag{16}$$

where $\alpha V/l = \alpha E = p_{max}$, and τ_{pol} is the time required for formation of the polarizable state. As p goes to p_{max}, the displacement current in the external circuit as a function of time is

$$i_{pol}(t) = \frac{N_{pol}}{l} \frac{dp}{dt} = N_{pol} \alpha \frac{V}{l^2 \tau_{pol}} exp\left(-\frac{t}{\tau_{pol}} \right) \tag{17}$$

"As soon as excited states are generated, there begins the process of their quenching at a rate

$$\frac{dN_{pol}(t)}{dt} = -\frac{N_{pol}(0)}{\tau_{exc}} exp\left(-\frac{t}{\tau_{exc}} \right) \tag{18}$$

which removes polarization induced by excitation and shows itself as an oppositely directed displacement current i_{depol}."

"Since the total charge transferred through the external circuit in a lifetime of polarized particles equals zero,

$$\int_0^\infty (i_{pol} - i_{depol}) dt = 0." \tag{19}$$

Then from equations 17 - 18 we get "the complete equation for the displacement current kinetics":

$$i_{pol}(t) = N_{pol} \alpha \frac{V}{l^2 \tau_{pol}} \left[exp\left(-\frac{t}{\tau_{pol}} \right) - \frac{\tau_{pol}}{\tau_{exc}} exp\left(-\frac{t}{\tau_{exc}} \right) \right] \tag{20}$$

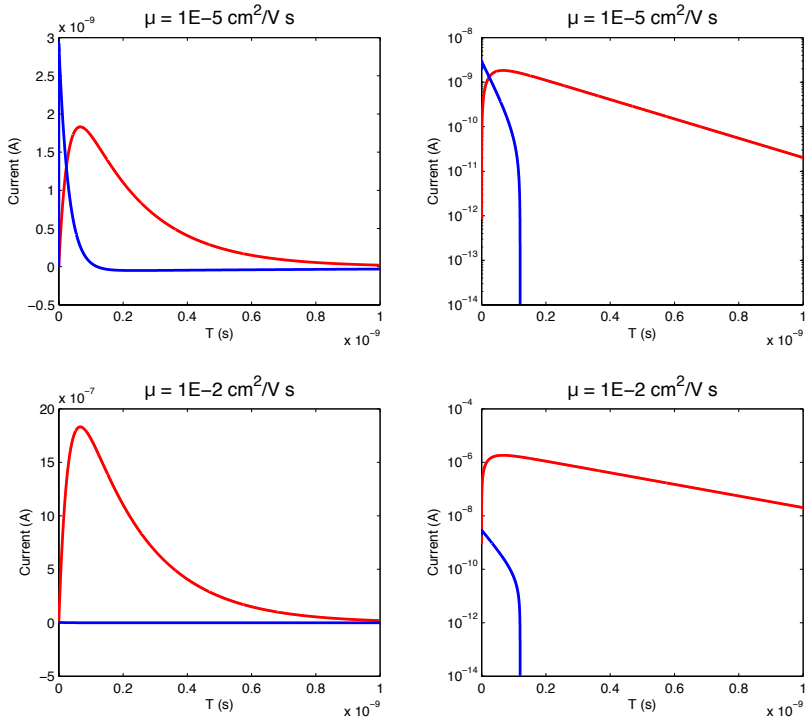

Figure 1. Plots of simulated currents due to free carriers (red) and polarization (blue). Left: linear. Right: logarithmic with respect to current (vertical axis). Top: Low μ (1 x 10^{-5}) for typical disordered organic material (e.g., DCDHF). Bottom: Higher μ (1 x 10^{-2}) for more ordered material (e.g., pentacene)

Again, using Equation 13, Equation 20 becomes

$$u_{pol}(t) = N_{pol}\alpha\frac{V \cdot R \cdot 1.1 \cdot 10^{-12}}{l^2} * \left[\frac{exp\,(-t/RC) - exp\,(-t/\tau_{pol})}{RC - \tau_{pol}} - \frac{exp\,(-t/RC) - exp\,(-t/\tau_{exc})}{RC - \tau_{exc}}\right] \quad (21)$$

"Numerical coefficients ... in Equations 14 and 21 imply that *u(t)* is expressed in V, provided that α comes in cm^3, μ in $cm^2/(Vs)$, R in Ω, C in F, t in s, and l in cm; N_{pol} and N_{free} are dimensionless quantities."

Code was written both in Mathematica and Matlab to apply these derivations to our case. The codes simply calculate and plot, from Equations 14 and 21, the respective contributions of current due to free carriers, and of displacement current of polarized excited states, to the measured voltage signal. The Matlab code will be given at the end of this Appendix. The code tested two different cases, that of a material with a low

mobility, $\mu = 10^{-5}$ cm^2/(Vs), assumed to be like DCDHF, and that of a material with higher mobility, $\mu = 10^{-2}$ cm^2/(Vs), assumed to be like pentacene, The mobility was the only parameter allowed to vary, primarily in order to keep the problem manageable. The relevant lifetimes, for both materials, were assumed to be: $\tau_{free} = 2 \cdot 10^{-10}$s, $\tau_{exc} = 1.5 \cdot 10^{-9}$s, $\tau_{pol} = 1 \cdot 10^{-14}$s. This value for τ_{free} is shorter than that typically assumed by Frankevich; this was done primarily in order to produce decay profiles similar to what we observed for Pc-TIPS. The other lifetime values are closer to his. The values for the RC time constant and for N_{pol} and N_{free} were adjusted similarly, for similar reasons.

The plots generated by this code are shown in Figure 1. It is evident that, while the contributions of the displacement current and the current due to free carriers are comparable on short time scales, for the material with the low mobility, the contribution of displacement current is negligible in the case of the material with the high mobility. The principal characteristic of the displacement current in both cases is that it is ended quickly. It may be seen from the plots that this current has essentially gone to zero, in either case, in just over 100 picoseconds.

The Matlab code is as follows:

```
taufree=2E-10;
tauexc=1.5E-9;
taupol=1E-14;
V=10;
l=25E-4;
Cap=7.5E-14;
alpha=1E-24;

mu=1E-5;

Nfree=1E9;Npol=1E9;R=50;

Nfreemu=Nfree*mu;
Npolalpha=Npol*alpha;
RC=8*R*Cap;

t=[0:1E-14:1E-9];

Ufree=Nfreemu*(V*taufree*1.6E-19/l^2)
*(exp(-t/RC)-exp(-t/taufree))*(RC-taufree)^(-1);


figure;
subplot(2,2,1);
plot(t,Ufree,'r','linewidth',2);
```

```
xlabel('T (s)');
ylabel('Current (A)');
hold;

Upol=Npolalpha*(V*R*1.1E-12/l^2)
*((exp(-t/RC)-exp(-t/taupol))/(RC-taupol)-
(exp(-t/RC)-exp(-t/tauexc))/(RC-tauexc));


plot(t,Upol,'b','linewidth',2)
xlabel('T (s)');
ylabel('Current (A)');
title('{\mu} = 1E-5 cm^2/V s');

subplot(2,2,2);
semilogy(t,Ufree,'r','linewidth',2);
xlabel('T (s)');
ylabel('Current (A)');
hold
semilogy(t,Upol,'b','linewidth',2);
xlabel('T (s)');
ylabel('Current (A)');
title('{\mu} = 1E-5 cm^2/V s')

mu=1E-2;

Nfree=1E9;Npol=1E9;R=50;

Nfreemu=Nfree*mu;
Npolalpha=Npol*alpha;
RC=8*R*Cap;

t=[0:1E-14:1E-9];

Ufree=Nfreemu*(V*taufree*1.6E-19/l^2)
*(exp(-t/RC)-exp(-t/taufree))*(RC-taufree)^(-1);

subplot(2,2,3);
plot(t,Ufree,'r','linewidth',2);
xlabel('T (s)');
ylabel('Current (A)');
hold;

Upol=Npolalpha*(V*R*1.1E-12/l^2)
*((exp(-t/RC)-exp(-t/taupol))/(RC-taupol)-
```

```
(exp(-t/RC)-exp(-t/tauexc))/(RC-tauexc));

plot(t,Upol,'b','linewidth',2);
xlabel('T (s)');
ylabel('Current (A)');
title('{\mu} = 1E-2 cm^2/V s')

subplot(2,2,4);
semilogy(t,Ufree,'r','linewidth',2);
xlabel('T (s)');
ylabel('Current (A)');
hold;
semilogy(t,Upol,'b','linewidth',2);
xlabel('T (s)');
ylabel('Current (A)');
title('{\mu} = 1E-2 cm^2/V s')
```

VITA

Jonathan Day was born November 21, 1954, in Salzburg, Austria. He grew up in Juneau, Alaska, moving to Portland, Oregon in 1972. He moved from Portland to Corvallis in 1979, and received his first Bachelor's Degree from Oregon State University, in Art, in 1983. He has continued to work in a variety of media since then, primarily oil painting and etching, and has exhibited regularly in the Willamette Valley. His work is in many private collections in Oregon and on the West Coast. He returned to the university in 1992, earning his Bachelor's Degree in Electrical Engineering from Oregon State in 1995. He worked in the telecommunication industry as a microwave design engineer, from 1995 to 2002, with design responsibility for several state-of-the-art cellular telephone base-station amplifier projects, principally featuring very low noise figures, for large-scale customers such as Nortel and Nextel. He returned, again, to the university in 2002, to pursue graduate work in physics. This led to the research described in this dissertation, which has also appeared in the following:

J. Day, S. Subramanian, J. E. Anthony, Z. Lu, R. J. Twieg, and O. Ostroverkhova, "Photoconductivity in organic thin films; From picoseconds to seconds after excitation", Journal of Applied Physics, Volume 103, Page 123715, 2008.

J. Day, O. Ostroverkhova, and J. Anthony, "Fast Photoresponse of Functionalized Pentacene and Anthradithiophene Thin Films", Proceedings of the Materials Research Society, Volume 1003, 2007.

Platt, Day, S. Subramanian, J. E. Anthony, and O. Ostroverkhova, "Floures-cent and Photoconductive Properties of Anthradithiophene and Pentacene Derivatives", CLEO/QELS, Baltimore, MD, USA, 2007.

A. D. Platt, W. Buchanan, J. Day, J. E. Anthony, and O. Ostroverkhova, Fluores-cent and photoconductive properties of functionalized pentacene and anthradithiophene derivatives, *Organic Thin Films for Photonic Applications*, *ACS National Meeting*, Philadelphia, PA, USA, August 2008.

O. Ostroverkhova, J. Day, A. D. Platt, J. E. Anthony, R. J. Twieg, Photoexcited charge carrier and exciton dynamics in organic semiconductors, **invited**, ICONO 10, Santa Fe, NM, USA, May 2008.

A. D. Platt, J. Day, J. E. Anthony, R. J. Twieg, and **O. Ostroverkhova**, Temperature dependent properties of novel functionalized anthradithiophene and DCDHF derivatives, CLEO/QELS, San Jose, CA, USA, May 2008.